UNIVERSIDADE DE SÃO PAULO

CENTRO DE ENERGIA NUCLEAR NA AGRICULTURA

SUSILAINE MAIRA SAVASSA

Analysis of the interaction of Ag and ZnO nanoparticles in *Phaseolus vulgaris*

Piracicaba

2019

SUSILAINE MAIRA SAVASSA

Analysis of the interaction of Ag and ZnO nanoparticles in *Phaseolus vulgaris*

Tese apresentada ao Centro de energia Nuclear na Agricultura da Universidade de São Paulo para a obtenção do título de Doutora em Ciências

Área de Concentração: Química na Agricultura e no Ambiente

Orientador: Prof. Dr. Hudson Wallace Pereira de Carvalho

Co-orientador: Dr. Hiram Armando Castillo Michel

Piracicaba
2019

Dados Internacionais de Catalogação na Publicação (CIP)

Seção Técnica de Biblioteca - CENA/USP

Savassa, Susilaine Maira
Análise da interação de nanoparticulas de Ag e ZnO em *Phaseolus vulgaris.* / Analysis of the interaction of Ag and ZnO nanoparticles in *Phaseolus vulgaris.* / Susilaine Maira Savassa; orientador Hudson Walace Pereira de Carvalho, co-orientador Hiram Armando Castillo Michel. - - Piracicaba, 2019.
115 p. : il.

Tese (Doutorado – Programa de Pós-Graduação em Ciências. Área de Concentração: Química na Agricultura e no Ambiente) – Centro de Energia Nuclear na Agricultura da Universidade de São Paulo.

1. Espectroscopia 2. Espectroscopoia infravermelha 3. Feijão 4. Fluorescência 5. Nanopartículas 6. Radiação sincrotron 7. Raios X I. Título

CDU (620.3 + 633.35) : 543.427.4

Elaborada por:
Marilia Ribeiro Garcia Henyei
CRB-8/3631
Resolução CFB Nº 184 de 29 de setembro de 2017

To my parents Margarida C. Gouveia Savassa and José
Antonio Savassa, to my sister Lucilaine M. Savassa,
and my husband Marcos Canto Machado
for love, support and always believe in me.

AKNOWLEDGMENTS

To God for everything in my life.

To the University of São Paulo (USP), the Center for Nuclear Energy in Agriculture (CENA) and the Postgraduate Science Program for the opportunity and infrastructure to develop this work. To European Synchrotron Radiation Facility (ESRF) for the opportunity of internship and working conditions available in France.

To the National Council for Scientific and Technological Development (CNPq) for the PhD scholarship in Brazil (grant 165479/2015-9) and to the Coordination for the Improvement of Higher Level Personnel (CAPES) for the Doctoral Program Sandwich Abroad (PDSE) for the scholarship abroad (grant 88881.131511/2016-01).

To Professor Hudson Wallace Pereira de Carvalho (CENA) for the confidence, patience and teachings. To Dr. Hiram Castillo-Michel (ESRF) for opportunity, co-orientation, patience and teachings during the PhD internship in France and after in the data analysis.

To beamline scientists from ID21 from ESRF, in special, Dr. Ana Pradas Del Real (ESRF) and Dr. Marine Cotte (ESRF), to beamline scientists from XRF, XAFS2 from Brazilian Synchrotron Light Laboratory (LNLS), Brazilian Nanotechnology National Laboratory (LNNano) and the Brazilian Biosciences National Laboratory (LNBio). To the Laboratory of Electron Microscopy “Prof. Elliot Watanabe Kitajima” (Luiz de Queiroz College of Agriculture - ESALQ), Laboratory of Histology and Structural Plant Biology (CENA) and the Laboratory of Cellular and Molecular Biology (CENA) for support and contributions in the development of this study.

To Prof. Cornelis A. M. van Gestel (Vrije Universiteit, Holand) for comments and suggestions that improved the chapter one of this thesis.

To technicians Cleusa Pereira Cabral (CENA), Mônica Lanzoni Rossi (CENA), Sheila Roberta Wenzel Perdigão (CENA) to their contribution to the analyzis and especially to Dr. Eduardo de Almeida (CENA), for sharing his knowledge and all support in the XRF analysis.

To PhD and Master's students from the Laboratory of Nuclear Instrumentation (LIN) Geovani, Joyce, Marcos, Nádia, Tatiana, Eduardo, Bianca and Rafael; to post-doc Dr. João Paulo Marques and, to students of Scientific Initiation, Gabriel, João and Sara for their friendship and cooperation to the development of this work.

To my friends from and outside CENA, Débora Grandino, Maristela Calvente Moraes, Carina Nascimento, Ana Carolina Boni de Bello, Thays Cristina B. Bonifácio and Mariana Tombolato for all support and trust, and to my four-legged friend Bruce by constant company.

“Where there is humility, there is wisdom”

Saint Thomas (Aquinas)

ABSTRACT

SAVASSA, S. M. **Analysis of the interaction of Ag and ZnO nanoparticles in *Phaseolus vulgaris.*** 2019. 115 p. Tese (Doutorado) – Centro de Energia Nuclear na Agricultura, Universidade de São Paulo, Piracicaba, 2019.

Nanoecotoxicology is a growing field of science driven by the extensive use of nanomaterials in commercial products and agriculture. Their use in agriculture is to become a reality through fertilizers and pesticides. On the other hand, little is known about possible collateral effects that of nanomaterials and therefore they may pose a threat to human health and the environment. To shed light on these topics, one must better understand the mechanisms of interaction between nanoparticles (NP) and living beings. Seed treatment is a common practice that provides micronutrients and protection. This study investigated the effects of ZnO and Ag NP on the germination of *Phaseolus vulgaris* seeds and the interaction (uptake and biotransformation) with the seed coat. Zinc-based nanoparticles were chosen because it is a plant micronutrient, whilst Ag ones present antimicrobial activity. The common bean seed treatments and synchrotron analysis were performed at the ID21 beamline in ESRF, CENA-USP and XRF beamline in LNLS. The bean seed coat presents three different layers, which are one of the objects of this study. The seeds were exposed to Ag_2S NP, Ag metallic NP, ZnO NP, $AgNO_3$ and $ZnSO_4$ in different concentrations (Ag 100 and 1000 mg L^{-1} while Zn 100, 1000 and 5000 mg L^{-1}). After 5 days of post-treatment and germination, seed coats were recovered, sectioned and investigated by FTIR, µ-XRF and µ-XANES. µ-XRF analysis showed that most of the NP treatments remained trapped in the seed coat, while µ-XANES unraveled that depending on the composition of pristine materials they can be biotransformed. Finally, FTIR pointed out that the proportion of organic functional groups present in the seed tissue were modified due to the presence of NP.

Keywords: *Phaseolus vulgaris*. ZnO nanoparticle. Ag nanoparticle. Germination. X-ray spectroscopy. X-ray fluorescence. X-ray absorption. Fourier transform infrared spectroscopy. Synchrotron-based techniques.

RESUMO

SAVASSA, S. M. **Análise da interação de nanoparticulas de Ag e ZnO em *Phaseolus vulgaris.*** 2019. 115 p. Tese (Doutorado) – Centro de Energia Nuclear na Agricultura, Universidade de São Paulo, Piracicaba, 2019.

A nanoecotoxicologia é um crescente campo da ciência impulsionado pelo uso extensivo de nanomateriais em produtos comerciais e na agricultura. Seu uso na agricultura está se tornando uma realidade através de fertilizantes e pesticidas. Por outro lado, pouco se sabe sobre possíveis efeitos colaterais dos nanomateriais e, portanto, podem representar uma ameaça à saúde humana e ao meio ambiente. Para esclarecer esses tópicos, é preciso entender melhor os mecanismos de interação entre nanopartículas (NP) e seres vivos. O tratamento de sementes é uma prática comum que fornece micronutrientes e proteção. Este estudo investigou os efeitos de ZnO e Ag NP na germinação de sementes de *Phaseolus vulgaris* e a interação (absorção e biotransformação) com o tegumento da semente. As nanopartículas à base de zinco foram escolhidas pelo Zn ser um micronutriente da planta, enquanto as da Ag apresentam atividade antimicrobiana. Os tratamentos de sementes de feijoeiro comum e análise síncrotron foram realizados na linha de luz ID21 da linha de luz ESRF, CENA-USP e XRF no LNLS. A casca do feijão apresenta três diferentes camadas, que são um dos objetos deste estudo. As sementes foram expostas a Ag_2S NP, Ag NP metálico, ZnO NP, $AgNO_3$ e $ZnSO_4$ em diferentes concentrações (Ag 100 e 1000 mg L^{-1}, enquanto Zn 100, 1000 e 5000 mg L^{-1}). Após 5 dias de pós-tratamento e germinação, as cascas das sementes foram separadas e seccionadas para serem investigadas por FTIR, µ-XRF e µ-XANES. A análise de µ-XRF mostrou que na maioria dos tratamentos com NP, elas permaneceram aprisionadas no tegumento da semente, enquanto µ-XANES revelou que, dependendo da composição dos materiais, eles podem ser biotransformados. Finalmente, FTIR apontou que uma parte de grupos funcionais orgânicos presentes no tecido das sementes foi modificada devido à presença de NP.

Palavras-chave*: Phaseolus vulgaris*. Nanopartícula de ZnO. Nanopartícula Ag. Germinação. Espectroscopia de raios X. Fluorescência de raios X. Absorção de raios X. Espectroscopia de infravermelho por transformada de Fourier. Técnicas baseadas em síncrotron.

SUMMARY

1 INTRODUCTION 17
1.1 Hypothesis 20
1.2 Objectives 20
1.3 Structure of the thesis 21
References 21
2 EFFECTS OF ZnO NANOPARTICLES ON *Phaseolus vulgaris* GERMINATION AND SEEDLING DEVELOPMENT DETERMINED BY X-RAY SPECTROSCOPY 24
Abstract 24
2.1 Introduction 25
2.2 Materials and Methods 27
2.2.1 Nanoparticles and Dispersions Characterization. 27
2.2.2 Germination Assay 29
2.2.3 Statistical Analysis of Germination and Weight Gain 30
2.2.4 Quantification of Zn Uptake and Root SEM Images 30
2.2.5 μ-XRF and μ-XANES 31
2.3 Results and Discussion 33
2.3.1 Nanoparticles and Dispersions Characterization 33
2.3.2 Germination Assay 34
2.3.3 Uptake of Zn by Seeds: Quantification and Spatial Distribution 38
2.3.4 Zinc Speciation 44
2.4 Conclusion 53
References 54
3 SYNCHRONTRON-BASED TECHNIQUE ASSOCIATED TO PLANT SCIENCE: A CASE OF Ag NANOPARTICLES IN COMMON BEAN GERMINATION 61
Abstract 61

3.1 Introduction 61

3.2 Materials and Methods 63

3.2.1 Characterization of Ag NPs 63

3.2.2 Germination assay 64

3.2.3 Scanning electron microscopy (SEM) 64

3.2.4 μ-XRF and μ-XANES 65

3.2.5 Fourier Transform Infrared Analysis 65

3.3. Results and Discussion 66

3.3.1 Germination assay 66

3.3.2 Spatial distribution of Ag in the hilum of *Phaseolus vulgaris* seeds 68

3.3.3 Ag localization and speciation in the seed coat 72

3.3.4 Fourier Transform Infrared Analysis 74

3.4 Conclusion 80

References 80

4 APPLICATION OF MICROPROBE SYNCHROTRON TECHNIQUES TO UNDERSTAND THE INTERACTION OF ZnO NANOPARTICLES IN *Phaseolus vulgaris* SEED COAT 87

Abstract 87

4.1 Introduction 87

4.2 Materials and Methods 89

4.2.1 Nanoparticles dispersion and common bean seeds 89

4.2.2 Scanning electron microscopy (SEM) 89

4.2.3 Microprobe X-ray fluorescence spectroscopy (μ-XRF) and micro-X-ray absorption near-edge structure (μ-XANES) 89

4.2.4 Fourier transform infrared analysis 90

4.3 Results and Discussion 91

4.3.1 Scanning electron microscopy 91

4.3.2 Zn localization and speciation within the seed coat 92

4.3.3 Fourier transform infrared analysis 95

4.4 Conclusion 105

References 105

5 GENERAL CONCLUSIONS.. 111

ANNEX 113

1 INTRODUCTION

The world population continues to grow. There are 7.7 billion people worldwide in 2019 and, the medium-variant projection indicates growing to 8.5 billion in 2030, 9.7 billion in 2050, and 10.9 billion in 2100 (PARANT, 1990). Currently, Brazil is the fifth most populated country in the world. The increase in the world population over the last two centuries has increased humanity's impact on the natural resources. The adequate provision of resources, space and food for the present and future large world population is a most important challenge of this century (ROSER, 2019).

Agriculture is one of the key sectors of production that need to innovate to win these challenges. Current agricultural practices heavily rely on the use of agrochemicals (fertilizers and pesticides) that quite often are applied inefficiently with a large fraction of these inputs finally lost or are unavailable to crops.

For optimal plant development, a balanced proportion of essential nutrients such as Zn, Cu, Fe, Mn, B, Mo, Cl and Ni is required. Zinc (Zn) is a micronutrient to plants since it plays a crucial role in the biological process such as enzymatic reactions, nitrogen metabolism, protein synthesis, among others (HAFEEZ, 2014). Therefore, fertilizers are used to supply deficiencies of this micronutrient in crops.

Pesticides are employed to prevent and control insects and plant diseases. In this context, silver (Ag) is known for its high antimicrobial and its different uses in medicine, food protection, clothing, and water disinfection (JO et al., 2009). The use of Ag in agricultural has recently became a subject of studies. From toxicological standing view, Ag may be safer to humans and fauna than common synthetic fungicides (JO et al., 2009).

Within this framework, Nanotechnology can contribute effectively to improve the crop production. The number of research articles in the literature in this topic has increased over the last decade. Figure 1 presents the number of publications and citations on Web of Science [v.5.32] (accessed date: June 21, 2019) using the keywords “nanotechnology” and “agriculture” along the last ten years. In 2009, about only 14 documents with these thematic where listed and had 68 citations, in 2018 these numbers significantly increased to 92 documents and 2299 citations thus demonstrating the importance and urgency of this matter.

Figure 1 - Number of publications and citations on Web of Science with the search term “Nanotechnology” and “Agriculture” grouped annually. Accessed date: June 21, 2019.

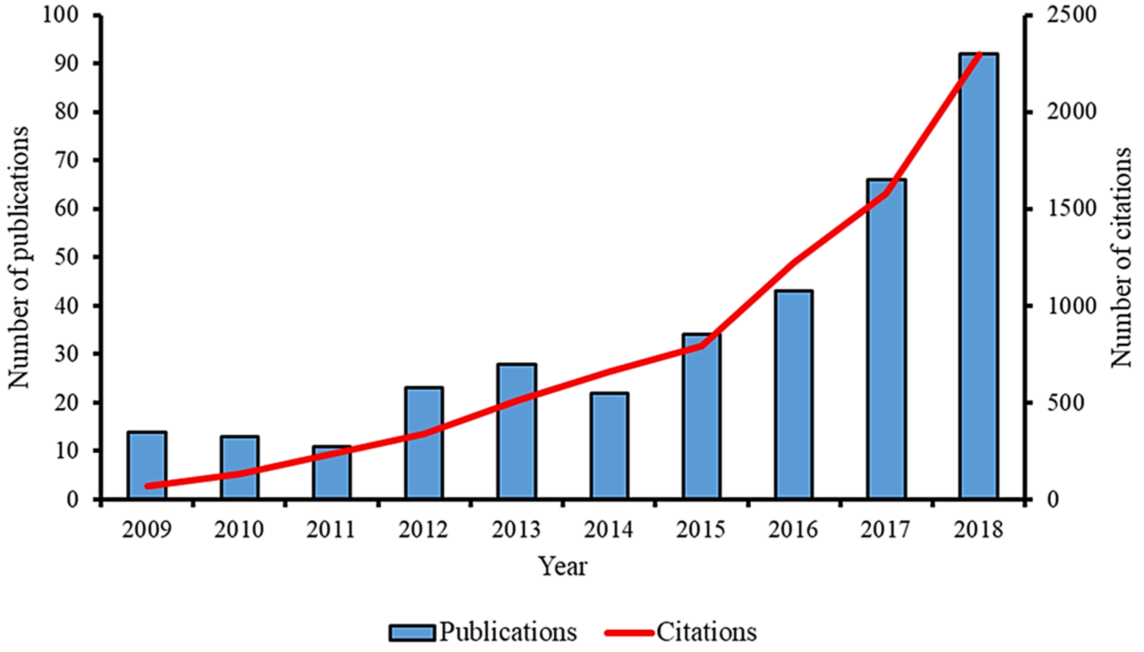

There are several definitions for nanoparticles, but almost all of them are in concordance that is a particulate substance with one dimension less than 100 nm (BOVERHOF et al., 2015). However, this definition should be reconsidered since particles larger than 100 nm may present size-dependent properties that differ from bulk analogs. Due to their small size interesting novel proprieties of nanoparticles such as chemical reactivity due to the higher fraction of atoms on the surface (high surface area), crystallinity, surface charge, solubility, dissolution, among others (BUZEA et al., 2007; LUYTS et al., 2013), compared with bulk materials make them interesting to develop new products.

Making use of all the potential of nanomaterials, literature presents a large number of studies that seek to perfect and create nanofertilizers and nanopesticides. Nanofertilizes can have the benefit to be more effective, minimizing losses comparing with the conventional ones (DIMKPA; BINDRABAN, 2018). Several studies showed that the effects of nanoparticles as nutritional complement can be positive or negative, depending on the properties of the particle, plant species, and phase of plant development.

Currently, a critical gap regards the concentration range of nanomaterials investigated in most studies. Several published studies involving plant micronutrients were carried out employing nanomaterials dispersions whose concentrations were far beyond those environmental relevant. For instance, in soil solution micronutrient availability is in the order of sub or few mg L^{-1}. This factor must be considered before attributing toxic or harmful effects to properties that arise at the nanoscale. This thesis presents results with experiments delineated with a range of concentrations from very low concentrations, i.e.1 mg L^{-1} to as many as 5000 mg L^{-1}.

To follow these advances and reliably evaluate the interactions between nanoparticles and plants, precise analytical techniques and powerful equipment are needed. For routine elemental content analyzes in plant tissues, techniques such as electrothermal atomic absorption spectroscopy (ET-AAS), inductively coupled plasma mass spectrometry (ICP-MS) and inductively coupled plasma optical emission spectrometry (ICP-OES) are commonly used. However, these techniques present some limitations, particularly the complex sample preparation and there is no possibility of analysis *in vivo*.

Multielement and non-destructive techniques like X-ray fluorescence spectroscopy (XRF), unlike the others mentioned, has a very simple or no sample preparation. This feature affords the analysis of in situ samples, fresh and in vivo plant tissues (CRUZ et al., 2017; GUERRA et al., 2018; RODRIGUES et al., 2018). In thesis, three variants of the XRF technique were employed, namely energy dispersive X-ray fluorescence (EDXRF), scanning electron microscope with energy dispersive X-ray spectroscopy (SEM-EDS) and energy dispersive microprobe X-ray fluorescence (μ-XRF). They granted quantitative and qualitative results as well as distribution maps of the elements of interest (Zn and Ag).

The limits of detection of benchtop EDXRF and μ-XRF are surpassed by synchrotron-based XRF. These techniques are essential for analysis at small samples and low concentrations as in environmental and biological samples (CASTILLO-MICHEL et al., 2017). This thesis used synchrotron-based micro/nanoprobes X-ray fluorescence (μ-XRF), synchrotron-based X-ray absorption spectroscopy (XAS), synchrotron Fourier transform infrared microscopy (μ-FTIR) and attenuated total reflection Fourier transform infrared spectroscopy (ATR-FTIR).

μ-XRF is an excellent tool to investigate the mineral distribution in biological tissues. For example, it can reveal the elemental distribution in primed seeds (DURAN et al., 2017; SAVASSA et al., 2018), uptake in root and stem (CRUZ et al., 2017; VAN DER ENT et al., 2018) and in leaves as well (UZU et al., 2010; VIGANI et al., 2018). On the one hand, XAS makes possible to determine the local structural and chemical environment of an absorbing atom. This technique takes into account the absorption energies of each atom, an X-ray beam (micro or nano lateral resolution) scans the sample over a range of energies below and above the absorption edge of the element of interest creating a spectrum. This thesis presents results using the X-ray absorption near-edge structure (XANES) by analyzing the specific region around the absorption possibility to determine the oxidation state, geometry and nature of ligands around the element of interest (PARSONS et al., 2002; YANO; YACHANDRA, 2009).

μ-FTIR and ATR-FTIR were used to determine biomolecular changes of the different tissue layers from the common bean seed coat. μ-FTIR allows to visualize the sample and to choose a specific region to analyze, being thus possible to examine tissue regions between the two surfaces (internal and external) of the seed coat. It requires samples in the order of a few micrometers thick. On the other hand, the sample preparation for ATR-FTIR is simpler and it allows to analyze the two surfaces from the seed coat, i.e. the cuticle and the parenchyma regions.

This research used as a model plant the common bean (*Phaseolus vulgaris*) that is one of the most consumed food legumes in the world mainly in Latin America and Africa (BEEBE et al., 2013). The seed is composed by a semipermeable seed coat (tegument) and an embryo (cotyledon). The seed coat has a protective function besides regulating the entrance of water for a successful process of germination (SOUZA; MARCOS-FILHO, 2001; SMÝKAL et al., 2014). As the seed coat of the bean serves as a kind of barrier, most of the applied treatments end up being retained, but another part penetrates. The latter one interact with the tissues making them a very attractive topic to be studied. Ultimately, it opened a possibility to better unravel the mechanisms of action of nanoparticles on vegetal.

1.1 Hypothesis

This study tested the following hypotheses:

- Nanoparticles (ZnO, Ag2S and Ag 0) can overcome the barriers of the common bean seed coat and penetrate within the seeds;
- Nanoparticles can enhance seed germination and seedling growth and to present a protective action.;
- Nanoparticles can be biotransformed after seed soaking;
- Nanoparticles can be translocated to different parts of plants.

1.2 Objectives

The aim of this thesis was to evaluate the effects of ZnO and Ag_2S, Ag^0 nanoparticles on the germination and seedling development of *Phaseolus vulgaris*. For this purpose, several experiments were carried out:

i. Nanoparticle characterization using dynamic light scattering (DLS), X-ray diffraction (XRD), EDXRF, scanning electron microscopy (SEM) and transmission electron microscopy;

ii. Seed soaking using a range of concentrations and different sizes of the nanoparticles, followed by evaluation of biometric parameters such as germination rate and seedling weight gain.

iii. Benchtop and synchrotron-based techniques like μ-XRF, μ-XANES, ATR-FTIR, and μ-FTIR to monitor the uptake, chemical environment and biomolecular changes in treated seeds and seedlings.

1.3 Structure of the thesis

In addition to the introductory text, this thesis is organized in three chapters:

Chapter 2: Effects of ZnO Nanoparticles on Phaseolus vulgaris Germination and Seedling Development Determined by X-ray Spectroscopy. This chapter corresponds to a manuscript published at ACS Appl. Nano Mater. 2018, 1, 6414−6426.

Chapter 3: Movement and chemical transformation of Ag nanoparticles in common bean seed coat during germination investigated by synchrotron-based techniques. [This chapter will be sent to publication].

Chapter 4: Application of microprobe synchrotron techniques to understand the interaction of ZnO nanoparticles in Phaseolus vulgaris seed coat. [This chapter will be sent to publication].

References

BEEBE, S. E.; RAO, I. M.; BLAIR, M. W.; ACOSTA-GALLEGOS, J. A. Phenotyping common beans for adaptation to drought. **Frontiers in Physiology**, Lausanne, v. 4, p. 35, 2013.

BOVERHOF, D. R.; BRAMANTE, C. M.; BUTALA, J. H.; CLANCY, S. F.; LAFRANCONI, M.; WEST, J.; GORDON, S. C. Comparative assessment of nanomaterial definitions and safety evaluation considerations. **Regulatory Toxicology and Pharmacology**, New York ,v. 73, n. 1, p. 137–150, 2015.

BUZEA, C.; PACHECO, I. I.; ROBBIE, K. Nanomaterials and nanoparticles: sources and toxicity. **Biointerphases**, Melville , v. 2, n. 4, p. 17-71, 2007.

CASTILLO-MICHEL, H. A.; LARUE, C.; PRADAS DEL REAL, A. E.; COTTE, M.; SARRET, G. Practical review on the use of synchrotron based micro and nano X-ray fluorescence mapping and X-ray absorption spectroscopy to investigate the interactions between plants and engineered nanomaterials. **Plant Physiology and Biochemistry**, Amsterdam, v. 110, p. 13–32, 2017.

CRUZ, T. N. M. DA; SAVASSA, S. M.; GOMES, M. H. F.; RODRIGUES, E. S.; DURAN, N. M.; ALMEIDA, E. de; MARTINELLI, A. P.; CARVALHO, H. W. P. Shedding light on the mechanisms of absorption and transport of ZnO nanoparticles by plants via in vivo X-ray spectroscopy. **Environmental Science: Nano**, London, v. 4, p. 2367-2376, 2017.

DIMKPA, C. O.; BINDRABAN, P. S. Nanofertilizers: New Products for the Industry? **Journal of Agricultural and Food Chemistry**, Washington, DC, v. 66, n. 26, p. 6462–6473, 2018.

DURAN, N. M.; SAVASSA, S. M.; LIMA, R. G. D.; ALMEIDA, E. de; LINHARES, F. S.; VAN GESTEL, C. A. M.; CARVALHO, H. W. P. de. X-ray spectroscopy uncovering the effects of Cu based nanoparticle concentration and structure on *Phaseolus vulgaris* germination and seedling development. **Journal of Agricultural and Food Chemistry**, Washington, DC, v. 65, n. 36, p. 7874-7884, 2017.

VAN DER ENT, A.; PRZYBYŁOWICZ, W. J.; JONGE, M. D.; HARRIS, H. H.; RYAN, C. G.; TYLKO, G.; PATERSON, D. J.; BARNABAS, A. D.; KOPITTKE, P.M.; MESJASZ-PRZYBYŁOWICZ, J. X-ray elemental mapping techniques for elucidating the ecophysiology of hyperaccumulator plants. **New Phytologist**, Oxford, v. 218, n. 2, p. 432–452, 2018.

GUERRA, M. B. B.; ADAME, A.; ALMEIDA, E. de; BRASIL, M. A. S.; SCHAEFER, C. E. G. R.; KRUG, F, J. In situ determination of K, Ca, S and Si in fresh sugar cane leaves by handheld energy dispersive X-Ray fluorescence spectrometry. **Journal of the Brazilian Chemical Society**, São Paulo, v. 29, p. 1086–1093, 2018.

HAFEEZ, B. Role of zinc in plant nutrition: a review. **American Journal of Experimental Agriculture**, London, v. 3, n. 2, p. 374–391, 2014.

JO, Y. K.; KIM, B. H.; JUNG, G. Antifungal activity of silver ions and nanoparticles on phytopathogenic fungi. **Plant Disease**, St. Paul, v. 93, n. 10, p. 1037–1043, 2009.

LUYTS, K.; NAPIERSKA, D.; NEMERY, B.; HOET, P. H. M. How physico-chemical characteristics of nanoparticles cause their toxicity: Complex and unresolved interrelations. **Environmental Sciences: Processes and Impacts**, Cambridge, v. 15, n. 1, p. 23–38, 2013.

PARANT, A. World population prospects**. Futuribles**, Paris, v. 141, p. 49-78, 1990.

PARSONS, J. G.; ALDRICH, M. V.; GARDEA-TORRESDEY, J. L. Environmental and biological applications of extended X-ray absorption fine structure (EXAFS) and X-ray absorption near edge structure (XANES) spectroscopies. **Applied Spectroscopy Reviews**, Philadelphia, v. 37, n. 2, p. 187–222, 2002.

RODRIGUES, E. S.; GOMES, M. H. F.; DURAN, N. M.; CASSANJI, J. G. B.; CRUZ, T. N. M.; SANT'ANNA NETO, A.; SAVASSA, S. M.; ALMEIDA, E. de; CARVALHO, H. W. P. Laboratory microprobe X-ray fluorescence in plant science: emerging applications and case studies. **Frontiers in Plant Science,** Lausanne, v. 9, p. 1588, 2018. doi: 10.3389/fpls.2018.01588.

ROSER, M. **Future population growth**. Oxford: University of Oxford, 2019. Disponível em: <https://ourworldindata.org/future-population-growth>. Acessed date: 04 July 2019.

SAVASSA, S. M.; DURAN, N. M.; RODRIGUES, E. S.; ALMEIDA, E. de; VAN GESTEL, C. A. M.; BOMPADRE, T. F. V.; CARVALHO, H. W. P. de. Effects of ZnO nanoparticles on Phaseolus vulgaris germination and seedling development determined by X-ray spectroscopy. **ACS Applied Nano Materials**, Washington, DC, v. 1, n. 11, p. 6414–6426, 2018.

SMÝKAL, P.; VERNOUD, V.; BLAIR, M. W.; SOUKUP, A.; THOMPSON, R. D. The role of the testa during development and in establishment of dormancy of the legume seed. **Frontiers in Plant Science**, Lausanne, v. 5, p. 351, 2014. doi: 10.3389/fpls.2014.00351.

SOUZA, F. H. D. D. E.; MARCOS-FILHO, J. The seed coat as a modulator of seed-environment relationships in Fabaceae. **Brazilian Journal of Botany**, São Paulo, v. 24, p. 365–375, 2001.

UZU, G.; SOBANSKA, S.; SARRET, G.; MUÑOZ, M.; DUMAT, C. Foliar lead uptake by lettuce exposed to atmospheric fallouts. **Environmental Science & Technology**, Washington, DC, v. 44, n. 3, p. 1036–1042, 2010.

VIGANI, G.; BOHIC, S.; FAORO, F.; VEKEMANS, B.; VINCZE, L.; TERZANO, R. Cellular fractionation and nanoscopic x-ray fluorescence imaging analyses reveal changes of zinc distribution in leaf cells of iron-deficient plants. **Frontiers in Plant Science**, Lausanne, v. 9, p. 1112, 2018. doi: 10.3389/fpls.2018.01112.

YANO, J.; YACHANDRA, V. K. X-ray absorption spectroscopy. **Photosynthesis Research**, Dordrecht, v. 102, n. 2, p. 241-254, 2009. doi: 10.1007/s11120-009-9473-8.

2 EFFECTS OF ZnO NANOPARTICLES ON *Phaseolus vulgaris* GERMINATION AND SEEDLING DEVELOPMENT DETERMINED BY X-RAY SPECTROSCOPY[1]

Abstract

There is still little information on the potential use of nanomaterials for seed nutrient enhancement through seed priming. The use of nanoparticles (NPs) in agriculture is promising, but in-depth knowledge on their interaction with plants is required. The aim of this study was to evaluate the effects of different concentrations (1−5000 mg L^{-1}) and sizes (20, 40, and 60 nm) of uncoated ZnO NP compared to ionic $ZnSO_4$ (positive control) on common bean (Phaseolus vulgaris) seed germination. The seeds were soaked in ZnO NP aqueous dispersions for 20 min. The ZnO nanoparticles did not affect the germination rate. The 10 mg L^{-1} 40 nm ZnO treatment showed a tendency to increase weight after 5 days (8.26 ± 0.11 g) when compared to the negative control (7.7 ± 0.7 g). However, at 5000 mg L^{-1} 40 nm ZnO NP and $ZnSO_4$ weight was reduced to 7.7 ± 0.8 g and 6.05 ± 0.08 g, respectively. Microprobe X-ray fluorescence showed that most of the Zn absorbed was trapped in the seed coat, while a small fraction entered the cotyledon. X-ray absorption spectroscopy indicated the biotransformation of the ZnO NP. In the hilum and cotyledon, Zn was found associated with organic molecules such as citrate, malate, and histidine-like compounds. Seedling weight reduction depended on the concentration of Zn taken up by the tissue and on the biotransformation of ZnO into organically bound Zn. Considering the properties of the studied NP, in particular the slow Zn release and lower toxicity compared to $ZnSO_4$, the results represent a step forward toward the application of ZnO NP as an agrochemical

Keywords: *Phaseolus vulgaris*, nano ZnO, germination, X-ray absorption spectroscopy, X-ray fluorescence, nanoparticles, seed

---

[1] This chapter has already been published as a scientific paper in the *ACS Applied Nano Materials:* SAVASSA, S. M. et al. Effects of ZnO nanoparticles on *Phaseolus vulgaris* germination and seedling development determined by X-ray spectroscopy. **ACS Applied Nano Materials**, v. 1, n. 11, p. 6414–6426, 26 nov. 2018.

2.1 Introduction

Nearly 49% of worldwide soils are Zn-deficient (SILLANPÄÄ, 1982). This fact reduces agriculture productivity (EKIZ et al., 1998; CAKMAK, 2000) afflicting ~1.1 billion people (KUMSSA et al., 2015) and makes Zn one of the nutrients with the lowest adequate intake (BEAL et al., 2017). Seed treatment is a widespread practice that intends to supply micronutrients such as Zn (FAROOQ et al., 2012; PROM-U-THAI et al., 2012; MUHAMMAD et al., 2015; LAVRES et al., 2016). Zinc treatment in cultures of, for instance, rice, wheat, chickpea, maize, and cowpea resulted in grain yield increases varying from ~6% up to 36% compared to the control plants (FAROOQ et al., 2012; TAVARES et al., 2013). Specifically, for wheat, in calcareous Zn-deficient soils, the grain yield increase promoted by seed priming reached 204%. Several Zn sources can be employed for this purpose, e.g., $ZnSO_4$, Zn-EDTA, and ZnO (FAROOQ et al., 2012).

Soluble Zn sources such as sulfates make Zn ions readily available for absorption by plants, while low solubility ZnO can slowly release the nutrient. One has to find a delivering balance responding to the plant demand and avoiding nutrient-induced phytotoxicity. Several studies showed that the solubility of nano-ZnO is affected by particle size (MUDUNKOTUWA et al., 2011; REED et al., 2012; CRUZ, et al., 2017). Thus, in principle, one could employ ZnO nanoparticles for seed treatment when being able to tune the rate of Zn supply to match with that of plant demand. Nanomaterials can be absorbed or biotransformed by plants via seeds (RATNIKOVA et al., 2015; DURAN, et al., 2017) stomata (LARUE et al., 2014; KIM et al., 2015) and roots (HERNANDEZ-VIEZCAS et al., 2011; CRUZ, et al., 2017).

At first glance, the output of investigations on the effect of nanoparticles (NPs) on plants seems to be contradictory. Positive effects were found for seed germination of Cicer arietinum immersed at 2000 mg L^{-1} ZnO NP (PANDEY et al., 2010) and on seed germination and seedling vigor of peanut treated with ZnO NP at 1000 mg L^{-1} (PRASAD et al., 2012), as well as for tomato treated with carbon nanotubes (KHODAKOVSKAYA et al., 2013). Exposure to 6 mg L^{-1} Ag as Ag_2S NP, however, decreased fresh mass of cowpea and wheat, while 0.6 mg L^{-1} Ag as Ag NP reduced their root and shoot growth (WANG et al., 2015). Additionally, 125, 250, and 500 mg L^{-1} Ag NP increased water loss in radish, whereas 500 mg L^{-1} Ag NP decreased root and shoot length (ZUVERZA-MENA et al., 2016). The oxidative stress in rice seedlings depended on CeO_2 NP exposure concentration (RICO et al., 2013). In another study, the nutritional value of rice cultivated in soil with 500 mg kg^{-1} CeO_2 NP was modified (RICO et al., 2013). These discrepancies may be caused by the difference in reactivity of the tested nanoparticles, specific properties of each plant species, differences in test media used, the wide range of studied concentrations, and last but not least the lack of a unified protocol for such experiments.

Aside from the environmental concern, nanotechnology might bring benefits for agriculture (HONG et al., 2013; SABIR et al., 2014; PETERS et al., 2016), especially for seed priming. The amount of nutrients available to seeds is a key factor that will influence the germination rate and seedling development (WANG et al., 2017; LIU et al., 2017). To increase their nutrient content and improve germination rate and seedling quality, seeds were soaked for 12 h in 10 mM $ZnSO_4$ and 50 mM KH_2PO_4 (AJOURI et al., 2004). However, soaking the seeds in 1000 mM $ZnSO_4$ prevented their germination. The challenge is to supply the right amount of nutrients without losses by leaching and meantime avoid phytotoxicity.

From the physiological perspective, seed germination is a dynamic process of transport, degradation, and syntheses of compounds. First, seed hydration activates the transcription of the DNA region that encodes amylase enzymes. Then, the amylases convert the carbohydrate macromolecules of the seed into maltose. These small sugars act as a source of energy enabling the radicle to emerge and start the germination (OZTURK et al., 2006; IWAI et al., 2012; MIANO et al., 2016).

An important question to be answered is whether and how engineered nanoparticles affect the above-mentioned processes. X-ray fluorescence (XRF) and absorption (XAS) spectroscopy are powerful tools to evaluate the fate of nanomaterials in biological systems (CASTILLO-MICHEL et al., 2017). Zinc presents absorption edge (9659 eV) and emission lines (8640 eV) at energies that make it possible to study this element under air with simple or no sample preparation. XRF yields quantitative information for Zn either by fundamental parameters calculation or calibration curves. XAS is suitable for chemical speciation, which makes it possible to investigate Zn in the local chemical environment. Additionally, the use of microprobe grants analysis with lateral resolution for XRF and XAS.

This study is aimed at investigating whether market available ZnO NPs are toxic or can actually promote the development of plants in their very early stages. A thorough investigation employing X-ray based spectroscopy (CASTILLO-MICHEL et al., 2017) was performed by examining the effect of ZnO NP on the germination of the common (kidney) bean (*Phaseolus vulgaris*) to uncover the pathways of ZnO NP uptake and biotransformation over a large range of concentrations and particle sizes.

2.2 Materials and Methods

2.2.1 Nanoparticles and Dispersions Characterization.

Three sizes of ZnO NP were used in this study. Powdered NP were purchased from MK Impex Corp. (20 and 40 nm) (Canada) and Nanophase (60 nm) (USA). Bulk ZnO (7 µm) was kindly supplied by Agrichem Company (Brazil). $ZnSO_4 \cdot 7H_2O$ was purchased from MERCK KGaA (Germany) and used as the ionic (Zn^{2+}) treatment. Energy dispersive X-ray fluorescence spectroscopy (EDXRF) (EDX720, Shimadzu, Japan) was used to determine the chemical composition of the pristine powders. The quantitative method and the chemical composition of the ZnO NP tested and degree of purity of Zn sources are presented in Table 1.

Table 1. Degree of purity of Zn sources and concentration of the contaminants present are shown for each of the nanoparticles used in this work

Zn source	Producer	Purity (%)	Contaminants (mg kg^{-1})	
			Ni	Ca
ZnO 20 nm	MK Impex Corp.	> 99.7%	335	2183
ZnO 40 nm	MK Impex Corp.	> 99.8%	316	1013
ZnO 60 nm	Nanophase	> 99.9%	300	---
ZnO 7 µm	Agrichem	>99.8 %*		
$ZnSO_4.7\ H_2O$	MERCK KGaA	<= 100 %*		

Scanning electron microscopy (SEM; Inspect F50, FEI Company, USA) was employed to image the shape of the nanoparticles (Figure 1). X-ray diffraction (XRD) patterns (Figure 2) were recorded with a PW 1877 diffractometer (Philips, The Netherlands) using Cu Kα radiation. The crystallite sizes are displayed in Table 2. For these two methods the samples were analyzed in powder form as received from manufacturer.

Figure 1. Scanning electron microscopy micrographs of the ZnO NP tested in this study. See Table 1. (a) 20 nm, (b) 40 nm and c) 60 nm

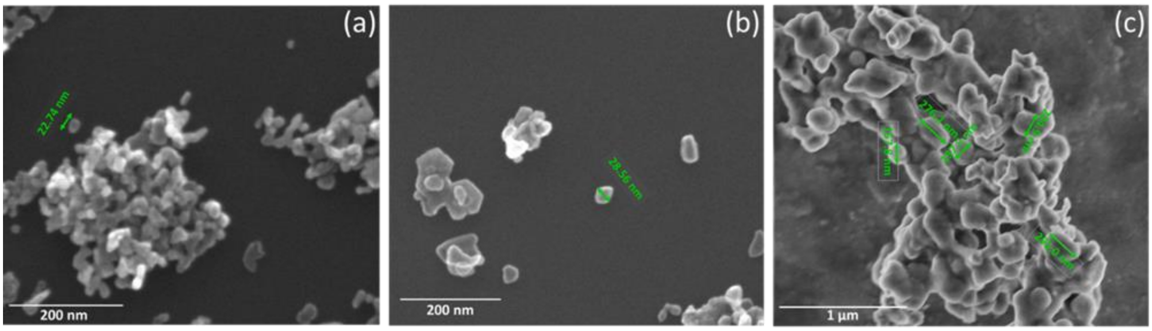

Figure 2. XRD pattern of the nano ZnO forms tested in this study. ZnO 20 nm, ZnO 40 nm and ZnO 60 nm

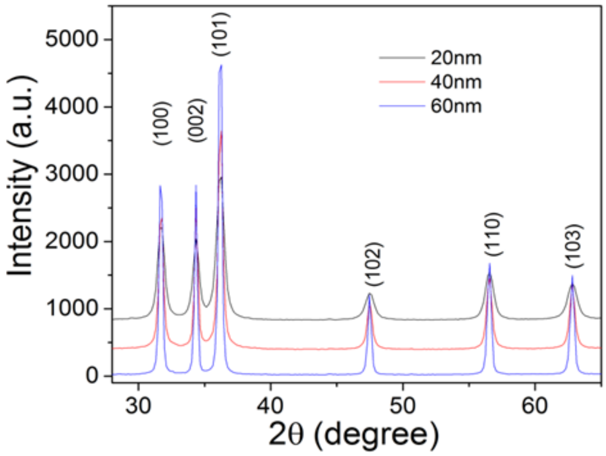

Table 2. Crystallite size (D) in different planes for XRD data of the ZnO NP tested in this study (20, 40 and 60 nm), hkl stands for the Miller indexes

Plane *(hkl)*	**D (nm)**		
	ZnO 20 nm	ZnO 40 nm	ZnO 60 nm
100	14.0	25.5	47.0
002	14.5	47.0	167.0
101	14.0	26.0	45.5

The solubility of the ZnO NP was evaluated by EDXRF (Figure 3). Hydrodynamic size was determined by dynamic light scattering (DLS), and the ζ potential was estimated using a Zetasizer Nano (Malvern Instruments Ltd., U.K.). The data are presented in Table 3. The concentration of the dispersions, expressed in mg L^{-1}, refers to the mass of ZnO in deionized water. The pH and conductivity of NP dispersions and $ZnSO_4$ solutions were measured using the pH/conductivity meter Mettler Toledo SG23, SevenGo Duo model. The ionic strength was estimated using the conductivity values as described in Table 4. For the $ZnSO_4$ reference compound, the concentration corresponds to the weight of Zn.

Figure 3. Concentrations of Zn in the supernatant solution of centrifuged dispersions of different ZnO NP and $ZnSO_4$ at different concentrations in deionized water. The measurements were performed in triplicate and error bars are the standard deviation of the mean

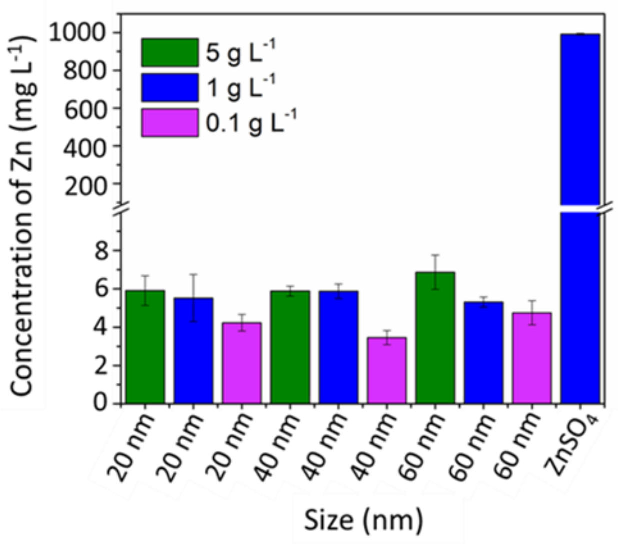

Table 3. ZnO NP characterization. Zeta potential and Dynamic Light Scattering for the different NP sizes (20, 40 and 60 nm) at 1 mg L^{-1}

Nominal size (nm)	Zeta-potential (mV)	Dynamic Light Scattering (agglomerate diameter – nm)		
		Peak 1	*Peak 2*	*Peak 3*
20	13 ± 4	913 (73%)	230 (27%)	--------
40	15 ± 4	5,442 (45%)	739 (31%)	124 (24%)
60	26 ± 4	299 (100%)	---------	--------

2.2.2 Germination Assay

The common bean is an economically important crop and significant source of dietary protein and carbohydrate for many countries. The seeds of *Phaseolus vulgaris* variety BRS Cometa (FARIA et al., 2008) (88% germination rate), obtained from the Brazilian Agricultural Research Corporation (Embrapa), are characterized by a low dormancy level, fast germination, and seedling development. These features make this variety suitable for laboratory experiments. Deionized water was used as the negative control and aqueous $ZnSO_4$ as the positive control. Seeds were previously weighed and washed in 10% sodium hypochlorite for 10 s and afterward rinsed in deionized water for another 10 s.

Twenty seeds were soaked for 20 min in the dispersions and then transferred to 15 cm Petri dishes covered with filter paper. The paper was moistened with 8 mL of the dispersion. Three replicates were used for each treatment. A plastic film (Parafilm) was used to wrap the dish edges and partially seal the dishes to avoid loss of moisture. The seeds were incubated for 5 days in a dark ventilated germination chamber (TE-4020, Tecnal, Brazil) at 27 °C. Subsequently, the germinated seed (seedling + seed coat) weight gains were determined (difference between the weight before and after 5 days of germination).

2.2.3 Statistical Analysis of Germination and Weight Gain

The germination assays were performed as a completely randomized designed with a factorial arrangement 5 × 5, with five sources of Zn (ZnO 20 nm, ZnO 40 nm, ZnO 60 nm, ZnO 7 μm, and $ZnSO_4$) and five concentrations (1, 10, 100, 1000 and 5000 mg L^{-1}), plus a control group (H_2O). Seventy-eight experimental units were used for the statistical analyses. The model that represents the fixed effects of treatments reads

$$Y_{ijk} = \mu + S_i + C_j + SxC_{ij} + e_{ijk}$$

where Y is the dependent variable (weight gain or germination rate), μ is the overall mean, S is the fixed effect of sources of Zn, C is the fixed effect of concentration, SC is the fixed effect of the interaction between source and concentration, and e is the random error assigned for each measurement, assuming that $e = iid \sim N(0,\sigma e^2)$. Dependent variable measurements were considered as outliers and were deleted from the database once the externally studentized residual was outside the range of −3 to 3.

The residues (observed − predicted) were plotted as a function of the predicted values to check the assumptions of error normality and homoscedasticity. If the assumption of normality failed, the data were mathematically transformed ($\log_{10}(x)$) for the analyses. However, the results presented are based on the original means. The mixed procedure was used and the means were tested by Tukey ($P < 0.05$).

2.2.4 Quantification of Zn Uptake and Root SEM Images

The germinated seeds were washed in deionized water to eliminate any externally adsorbed Zn, dried at 60 °C for 48 h, and separated in two fractions: seedling and seed coat. One gram of each fraction was weighed in a previously decontaminated porcelain crucible and placed into a muffle furnace (Fornitec, F-2, Brazil). The temperature was increased at a 100 °C h^{-1} ramp rate up to 500 °C, and the sample was ashed for 12 h. Subsequently, the ashes were dissolved in 5 mL of 1 M HNO_3 and an amount of 950 µL of the digest was transferred into vials to which 50 µL of Ga 1000 mg L^{-1} was added as internal standard. The sample was homogenized on a tube shaker (Marconi MA 162, Brazil). Zn quantification was carried out using external standard calibration.

Afterward, an amount of 15 µL of the sample was pipetted onto a 6.3 window XRF cuvette (no. 3577, Spex Ind. Inc., USA) sealed with 5 µm thick polypropylene film. The sample was dried at 60 °C in a laboratory oven. This procedure was performed twice. The thin-film sample analyses were carried out in triplicate using the same ZnO NP solubility analysis conditions. Considering the premise that Zn present in the seed coat was adsorbed, we evaluated the affinity of Zn for binding to this tissue using the Freundlich isotherm as explained in (HAMDAOUI; NAFFRECHOUX, 2007). The amount of adsorbed solute (qe) was the concentration of Zn determined by XRF, and the equilibrium concentration (Ce) was the content of Zn present in the solution and dispersions.

For SEM, five seedlings treated with 100 and 1000 mg L^{-1} ZnO dispersions were used. The primary root sampled was cross-sectioned below the secondary roots zones. The samples were processed according (MARQUES et al., 2017). They were fixed using a modified Karnovsky’s solution (KARNOVSKY, 1965) (2.5% glutaraldehyde, 2% paraformaldehyde, 0.05 M cacodylate buffer (pH 7.2), and 0.001 M $CaCl_2$), dehydrated in a graded acetone series (30, 50, 70, 90, and 100%), and critical point drying using CO_2 (Leica CPD300) mounted on aluminum stubs using double-sided carbon tape and gold coated (Bal-tec model SCD 050).

Images were captured using a scanning electron microscope (Jeol, JSM IT 300) at 15 kV.

2.2.5 µ-XRF and µ-XANES

Microprobe X-ray fluorescence spectroscopy (µ-XRF) (Orbis PC, EDAX, USA) was used to map the 2D spatial distribution of Zn and other elements, the experimental setup is shown in Figure 4 (a). The X-ray was provided with a Rh anode X-ray tube working at 40 kV and 300 µA. A 30 µm X-ray beam for the Mo Kα was produced by a polycapillary optical element. The detection was carried out by a 30 mm^2 silicon drift detector with resolution of 140 eV for Mn Kα. The maps were registered using a matrix of 128 × 100 points. The dwell time was 1 s per pixel, the measurements were performed under vacuum, and the dead time was around 3%.

The XRF intensity maps correspond to the net intensity (total Kα peak intensity minus background intensity). The calculation of the concentration of Zn spots in the seed hilum was performed by emission-transmission. Zn K edge microprobe X-ray absorption near edge structure (μ-XANES) was measured at the Brazilian Synchrotron Light Laboratory (LNLS) on the XRF beamline (PÉREZ et al., 1999). The beamline was equipped with a bending-magnet, Si (111) double crystal monochromator, KB mirror system resulting in a 20 μm diameter spot size, and silicon drift detector (SDD; KETEK GmbH, Germany). The experimental setup is presented in Figure 4 (b).

Figure 4. (a) μ-XRF experimental setup at the LIN-CENA-USP, Piracicaba, Brazil. (b) μ-XANES experimental setup at XRF beamline of the LNLS, Campinas, Brazil

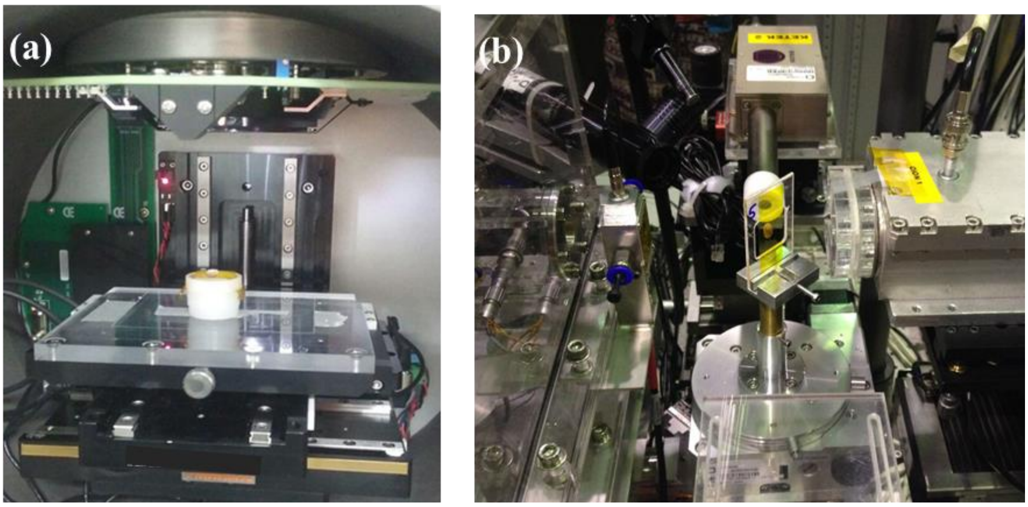

As the literature shows radiations of 10^7 Gy can damage biological tissues, the seeds were exposed to a dose of maximum ~5×10^5 Gy (calculated according to CRUZ et al., 2017). Additionally, we did observe the appearance of new spectral features in subsequently recorded spectra. These two factors suggest no radiation damage, such as induced changes in chemical compounds and cells rupture (YANO et al., 2005; JAMES et al., 2016).

Besides the bean seeds, using the microprobe, we measured several Zn reference compounds that were either purchased or prepared in our laboratory according to (SARRET et al., 2009). Briefly, a 3.15×10^{-4} M aqueous solution of $ZnCl_2$ (Exôdo Científica, Brazil) and then the ligand in acidic form (histidine (Exôdo Científica, Brazil), malate (Exôdo Científica, Brazil), citrate (J. T. Baker), phosphate (J. T. Baker), phytate (Sigma-Aldrich)) were slowly added in a ratio of 10 mol of ligand/mol of Zn, and finally pH was adjusted to 6 and the mixture was stirred for 2 h. For Zn sulfate (Dinamica Química Contemporânea LTDA) and acetate (Synth) PA reactants were used as purchased. The solutions were frozen and freeze-dried. The obtained powders were pelletized in cellulose at 0.2 and 1.0 Zn wt % and were included in the LC analysis as model spectra. To improve the signal-to-noise ratio, three μ-XANES spectra were merged. The energy calibration was done with a reference Zn foil.

Spectra normalization and linear combination fitting (LCF) analysis were performed through the module Athena in the IFEFFIT package (RAVEL; NEWVILLE, 2005). In the LCF procedure we first choose spectra that presented features similar to those exhibited by the seed samples, and then we evaluated their suitability through a combinatorial fit routine available at the Athena code. The following compounds were tested: Zn-histidine, Zn-malate, Zn-citrate, Zn-acetate, $ZnSO_4$, and ZnO. Finally, aiming at presetting more robust LCF results, we selected the least number of compounds that returned similar *R-factors*. The *R-factor* represents the mismatch between the actual data and the fitted curve, and more details can be found in (CALVIN, 2013).

2.3 Results and Discussion

2.3.1 Nanoparticles and Dispersions Characterization

Nanoparticles were characterized using different techniques. Figure 1 shows micrographs of the 20 nm, 40 nm, and 60 nm ZnO NPs. In the aggregates it is possible to verify different forms in different sizes of nanomaterial. The crystallite size determined by the Scherrer equation using XRD patterns (Figure 2) confirms that 20 nm ZnO NP had a spherical profile (almost same for the all plane sizes). The 40 and 60 nm ZnO NPs showed an elongated form (one plane is different to the others).

It is possible to verify by DLS (Table 3) that ZnO NP agglomerated in dispersion forming multimodal aggregates. The particle size varied from 124 nm to 5.4 μm. It is important to highlight that the particles were not dispersed by any surfactant. This was done aiming at avoiding the interference of surface agents on the biological results. The ζ-potential measurements showed that regardless of the particle, the surface charge was positive. The low magnitude of the potential, below 30 mV (Table 3), helps to understand the aggregation trend observed by DLS.

The amount of soluble Zn, shown in Figure 3, was determined using EDXRF. The ZnO NP dispersions presented similar amounts of soluble Zn regardless of the particle size (4−7 mg Zn L^{-1}). The overlap of the error bars, however, does not allow conclusion that the differences in solubility were a function of particle size. The soluble Zn concentrations were smaller than those reported by (BIAN et al., 2011), who found values from 10 to 57 mg Zn L^{-1} for ZnO particle sizes ranging from 241 nm down to 4 nm. Table 4 presents the pH values of all treatments. For all bulk and nano ZnO suspensions, the pH varied from 6.99 to 7.92 and was not affected by particle concentration. For $ZnSO_4$ treatments, pH decreased from 6.95 to 5.15 as the Zn concentration increased.

2.3.2 Germination Assay

We first determined the effect of ZnO NP size (20 nm, 40 nm, 60 nm, and 7 μm) and concentration (1, 10, 100, 1000, and 5000 mg L^{-1}) on the morphological development of the bean seedlings. Figure 5 shows the root development 5 days after soaking the seeds in the ZnO NP dispersions. For the 40 nm ZnO NP treatment, the most beneficial effect was found at 10 mg L^{-1} which presented one of the biggest elongation rates. All treatments at 5000 mg L^{-1} had deleterious effects on the bean seedlings; the root system was shortened and tangled compared to the negative control and lower concentrations.

Table 4. ZnO NP dispersion characterization. Values of pH, conductivity and estimated ionic strength for all dispersions and solutions used in this study

Treatments	**pH**	**Conductivity (μS cm^{-1})**	**Ionic strength calculated according to** (ZENG et al., 2011)^{a} **(mmol L^{-1})**	**Ionic strength calculated according to** (GRIFFIN; JURINAK, 1973)^{b} **(mmol L^{-1})**
H_2O	7.0	1.8	0.0022	0.028
20 nm 1 mg L^{-1}	7.6	4.1	0.0052	0.065
20 nm 10 mg L^{-1}	7.3	13.7	0.017	0.22
20 nm 100 mg L^{-1}	7.7	12.9	0.016	0.21
20 nm 1000 mg L^{-1}	7.6	33.0	0.042	0.53
20 nm 5000 mg L^{-1}	7.0	113	0.14	1.81
40 nm 1 mg L^{-1}	7.7	4.0	0.0051	0.064
40 nm 10 mg L^{-1}	7.6	12.1	0.015	0.19
40 nm 100 mg L^{-1}	7.6	15.3	0.019	0.24
40 nm 1000 mg L^{-1}	7.7	26.2	0.033	0.42
40 nm 5000 mg L^{-1}	7.7	59.1	0.075	0.95
60 nm 1 mg L^{-1}	7.9	2.9	0.0037	0.046
60 nm 10 mg L^{-1}	7.9	10.2	0.013	0.16
60 nm 100 mg L^{-1}	7.9	11.1	0.014	0.18
60 nm 1000 mg L^{-1}	7.8	17.7	0.022	0.28
60 nm 5000 mg L^{-1}	7.8	16.9	0.021	0.27
$ZnSO_4$ 1 mg L^{-1}	6.9	4.4	0.0056	0.071
$ZnSO_4$ 10 mg L^{-1}	6.6	32.2	0.041	0.51
$ZnSO_4$ 100 mg L^{-1}	6.2	267	0.34	4.27
$ZnSO_4$ 1000 mg L^{-1}	5.6	1,852	2.35	29.6
$ZnSO_4$ 5000 mg L^{-1}	5.1	8,650	0.011	0.14
ZnO 7 µm 1 mg L^{-1}	7.5	2.6	0.0032	0.041
ZnO 7 µm 10 mg L^{-1}	7.4	13.5	0.017	0.22
ZnO 7 µm 100 mg L^{-1}	7.4	11.7	0.015	0.19
ZnO 7 µm 1000 mg L^{-1}	7.5	15.1	0.019	0.24
ZnO 7 µm 5000 mg L^{-1}	7.1	14.8	0.019	0.24

[a] $I = 1.27 \times 10^{-6} \times \text{Conductivity } (\mu\text{S cm}^{-1})$ 1

[b] $I = 1.60 \times 10^{-5} \times \text{Conductivity } (\mu\text{S cm}^{-1})$ 2

Figure 5. Common bean (Phaseolus vulgaris) seedlings after 5 days incubation in a growth chamber: (a) $ZnSO_4$, (b) bulk ZnO, (c) 40 nm ZnO NP, (d) 60 nm ZnO NP, (e) 20 nm ZnO NP, and (f) control (H_2O). Higher concentrations of the treatments prevented proper root development, and lower concentrations such as ZnO 40 nm 10 mg L^{-1} presented one of the biggest root elongation and more lateral roots

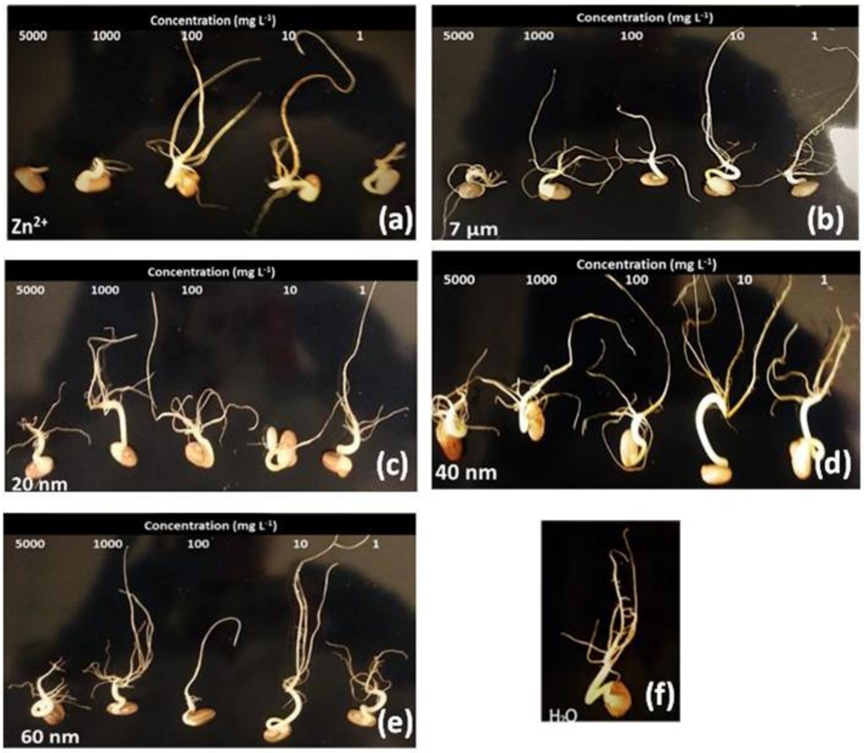

Table 5 presents the seed germination rate (%) as a function of treatment. Neither the nanoparticles nor bulk ZnO affected the seed germination rate; i.e., the particle size did not play any role in the effects on germination rate. On the other hand, $ZnSO_4$ at 5000 mg L^{-1} decreased the number of viable seeds. At the germination level, ZnO NP appeared to be less toxic compared to its free ion metal counterpart. This suggests that the deleterious effect is promoted by the excess of zinc ions. The NP released just a small quantity of Zn^{2+} that varied from 3 to 7 mg L^{-1} of Zn.

Table 6 presents the weight gain (g) of seedlings as a function of treatment. The control group (water treatment with weight gain of 7.6 ± 0.4 g) was tested by orthogonal contrast. The results indicated no significant differences among treatments ($P = 0.60$); therefore, the data shown in Table 6 are presented without water treatment. Concerning particle size, the only significant difference was found for 40 nm ZnO and 7 µm ZnO versus $ZnSO_4$. The 40 nm and bulk particles induced the highest weight gain, followed by 60 and 20 nm ZnO.

Table 5. Germination rate (%) in Phaseolus vulgaris bean seeds, five days after treatment with ZnSO$_4$ or differently sized ZnO NP and different concentrations of each source, in the germination assay

Concentration	**ZnO 20nm**	**ZnO 40nm**	**ZnO 60nm**	**ZnO 7µm**	**ZnSO$_4$**	**Mean**
1 mg L^{-1}	78	75	83	88	73^{A}	79
10 mg L^{-1}	68	90	83	78	78^{A}	79
100 mg L^{-1}	78	78	80	81	75^{A}	78
1000 mg L^{-1}	73	85	81	78	71^{A}	78
5000 mg L^{-1}	71^{a}	86^{a}	80^{a}	78^{a}	48$^{B\ b}$	73
Mean	74^{AB}	83^{A}	81^{A}	81^{A}	69^{B}	

$^{A,\ B,\ C}$ means followed by different uppercase letters differ in the column (different NP sizes, ZnO bulk and ZnSO$_4$). $^{a,\ b,\ c}$ means followed by different lowercase letters differ in the row (different concentration, 1 - 5000 mg L^{-1}). Tukey test (P = 5%). ^{1}mean of germination rate values (%) for a defined concentration, i.e. rows. ^{2}mean germination rate values (%) given by a defined source of Zn, i.e. columns.

Table 6. Weight gain of common bean seeds (g) on the fifth day of the germination assay following different treatments with ZnSO$_4$ or differently sized ZnO NP, and different concentrations of each source

Concentration	**ZnO 20nm**	**ZnO 40nm**	**ZnO 60nm**	**ZnO 7µm**	**ZnSO$_4$**	**Mean^{1}**
1 mg L^{-1}	7.6	7.2^{B}	7.7	8.2^{A}	7.5^{A}	7.6^{ab}
10 mg L^{-1}	7.6	8.3^{A}	7.7	7.8^{AB}	7.8^{A}	7.8^{a}
100 mg L^{-1}	7.6	7.6^{AB}	7.7	7.5^{AB}	7.3^{A}	7.6^{ab}
1000 mg L^{-1}	7.3	7.7^{AB}	7.3	7.5^{AB}	6.9^{AB}	7.3^{b}
5000 mg L^{-1}	6.9^{ab}	7.0$^{AB\ a}$	7.0^{ab}	7.0$^{B\ ab}$	6.0$^{B\ b}$	6.9^{b}
Mean^{2}	7.39^{AB}	7.7^{A}	7.5^{AB}	7.6^{A}	7.1^{B}	

$^{A,\ B,\ C}$ means followed by different uppercase letters differ in the column (different NP sizes, ZnO bulk and ZnSO$_4$). $^{a,\ b,\ c}$ means followed by different lowercase letters differ in the row (different concentration, 1 - 5000 mg L^{-1}). Tukey test (P = 5%).^{1}mean of weight gain values (g) for a defined concentration, i.e. rows. ^{2}mean weight gain values (g) given by a defined source of Zn, i.e. columns.

The lowest weight gain was found for ZnSO$_4$. The lower weight gains were associated with the highest concentrations (1000 and 5000 mg L^{-1}).

The seed germination was less sensitive than the seedling weight gain. The concentration of the treatment had more impact on the seedling development than the particle size. (GUERINOT, 2000) suggested that under Zn excess some genes, e.g., ZIP1, lose their regulation and affect the metal transporters, leading to toxic effects on the plant. Among the treatments, the highest weight gain was observed for 40 nm ZnO.

Figure 3 shows the lowest solubility (3.5 ± 0.4 mg Zn L^{-1}) for the 40 nm ZnO NP at 100 mg L^{-1} and the highest one (4.8 ± 0.6 mg L^{-1}) for 60 nm ZnO NP at 100 mg L^{-1}. Since $ZnSO_4$ was used as positive control, the observed trend for a beneficial effect of 40 nm ZnO dispersions on seedling development cannot be related to the soluble Zn concentration.

Similar results were presented for Arabidopsis thaliana, suggesting that Zn stress can alter the root system architecture. On the other hand, for maize, 10 mg L^{-1} ZnO NP induced the root growth, while 1000 mg L^{-1} ZnO NP was toxic, decreasing germination rate and hindering root development (ZHANG et al., 2015).

Wang et al. (2016) reported mass loss of Arabidopsis plants treated with 200 mg L^{-1} of ZnO NP. Another study showed that a concentration of 750 mg L^{-1} was highly toxic to rice, reducing germination compared to the control (without ZnO NP). The same happened with the roots that showed size reduction with increasing Zn concentrations (SALAH et al., 2015). Our results showed that seed priming with ZnO NP up to 100 mg L^{-1} did not harm seedling development. The 40 nm ZnO even presented a trend suggesting a positive effect at 10−100 mg L^{-1}.

2.3.3 Uptake of Zn by Seeds: Quantification and Spatial Distribution

The germinated seeds were washed to remove any excess of Zn from the surface, but since deionized water was used, the procedure did not remove the adsorbed Zn. Then, the germinated seeds were divided into seed coat and seedling. After dry digestion, they were analyzed by EDXRF. Figure 6 a shows the concentration of Zn found in the seed coat and Figure 6 b the concentration of Zn in the germinated seed (cotyledon + primary root). The concentration of Zn in both tissues increased as a function of the concentration of the ZnO NP dispersion/solution used for priming. The negative control, i.e., the seeds germinated in deionized water, presented Zn concentrations of 24.6 ± 1.2 mg kg^{-1} in the seed coat and 37.4 ± 0.9 mg kg^{-1} in the germinated seedling.

For ZnO NP treated seeds, the seed coat structure retained most of the Zn and had concentrations varying from nearly 50 up to 11 385 mg kg^{-1}. The amplitude of the concentrations presented lower variation in the seedling. In seeds soaked in 1mg L^{-1} ZnO NP dispersions the Zn did not reach the inner part of the seed.

Figure 6. Zinc concentrations, determined using X-ray fluorescence, in the (a) seed coat and (b) seedling of common beans (*Phaseolus vulgaris*) soaked in different concentrations of 20 nm, 40 nm, 60 nm, and 7 µm ZnO NP and $ZnSO_4$

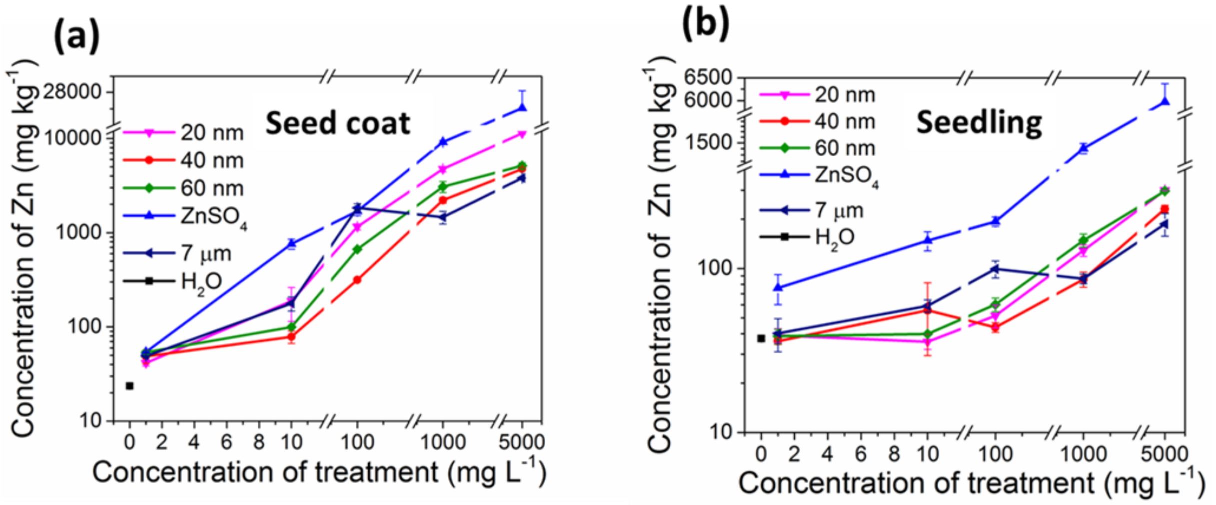

Figure 7 shows the concentration of Zn in the seedling as a function of the concentration of dissolved Zn. However, it does not show a clear correlation.

The data shown in Figure 6a and Figure 6b are also presented without breaks in Figures 8 and 9, respectively. These figures show that the uptake of Zn in the seed coat at different exposure concentrations followed an asymptotic function. A trend of saturation of Zn adsorption sites under high concentrations can be noticed.

Figure 7. Relation of concentration of Zn in seedling (mg L^{-1}) and concentration of Zn in supernatant solution (mg L^{-1})

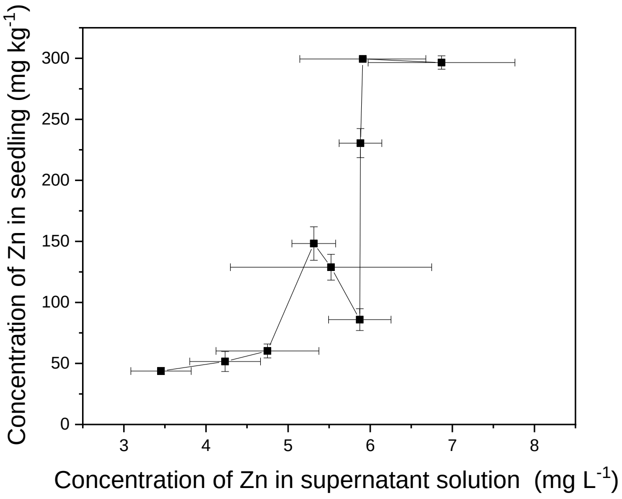

Figure 8. Uptake of Zn by the *Phaseolus vulgaris* seed coat as a function of the concentration of each treatment. The same data are shown in Figure 6 (a) with breaks. At high concentrations the Zn adsorption sites seem to become saturated. (a) $ZnSO_4$, (b) 20 nm ZnO NP, (c) 40 nm ZnO NP, (d) 60 nm ZnO NP and (e) 7 µm ZnO

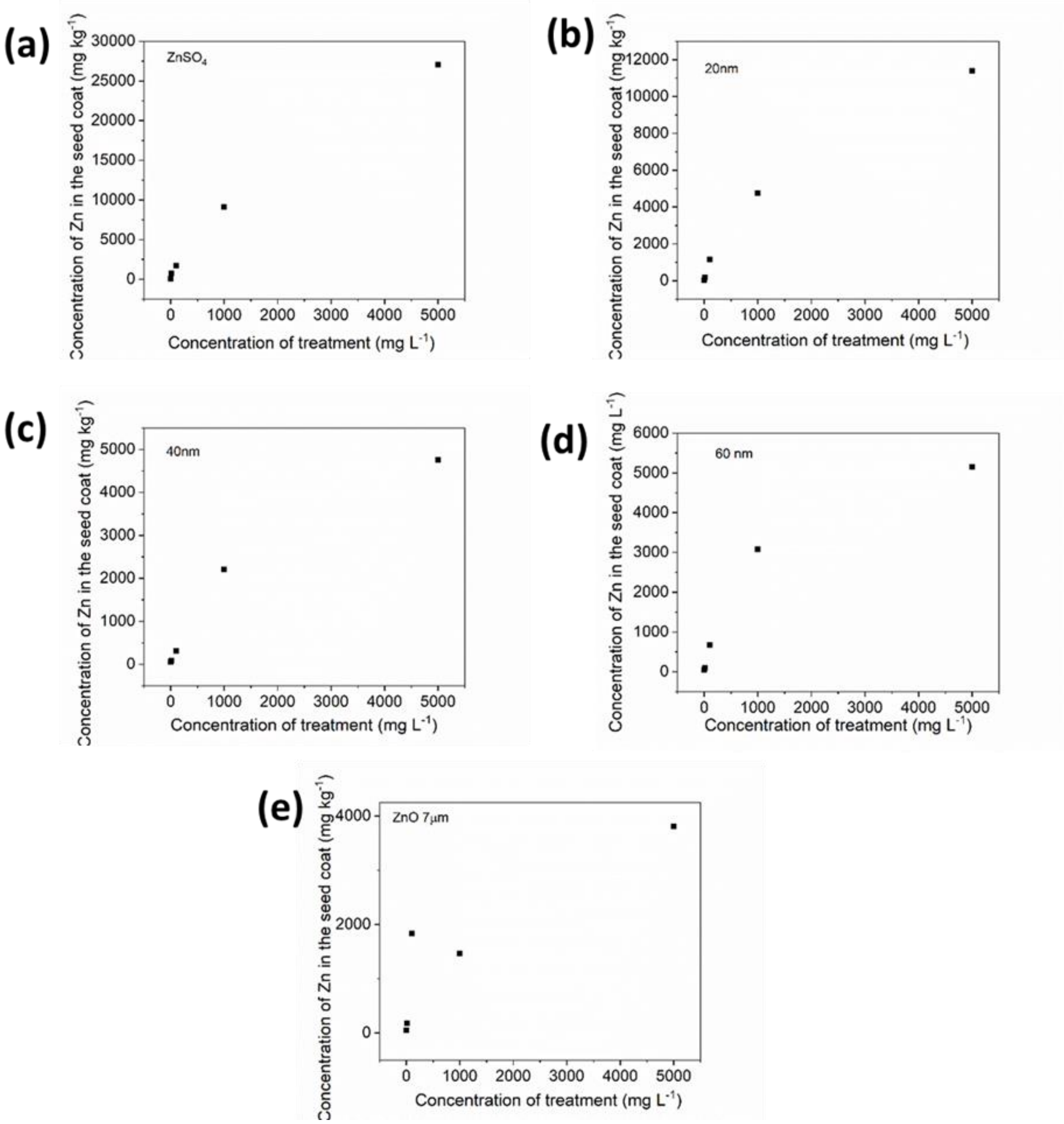

Figure 9. Uptake of Zn by the *Phaseolus vulgaris* seed embryo as function of the concentration of each treatment. The same data are shown in Figure 6 (b) with breaks. (a) $ZnSO_4$, (b) 20 nm ZnO NP, (c) 40 nm ZnO NP, (d) 60 nm ZnO NP and (e) 7 µm ZnO

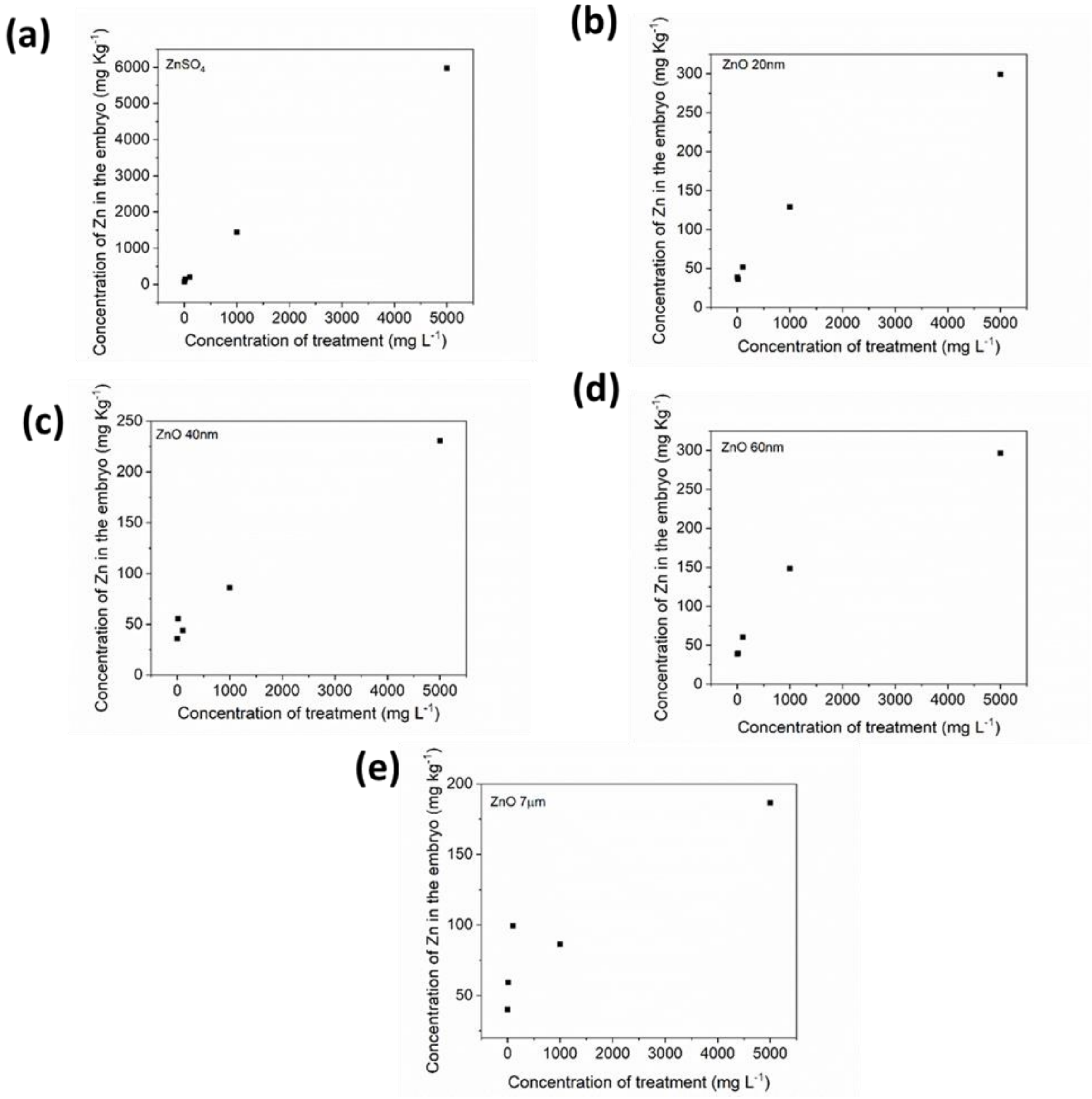

One of the simplest mathematical models for adsorption processes revealing constants with physical meaning is the Freundlich isotherm ($x/m = K_f c^{1/n}$), where x is the mass of adsorbate, m is the mass of the substrate, Kf is a measure of the binding strength, and $1/n$ is a measure of the linearity and thus of the concentration dependency of the sorption isotherm.

Due to the restrictions imposed by the experimental conditions of the present work, i.e., the experiments not carried out under isothermal conditions and the equilibrium concentrations not determined, the true Freundlich *K* and *1/n* could not be calculated. However, as the log–log plots of the concentration of Zn incorporated in the seed coat versus the concentration of the treatment returned straight lines with correlation coefficients (Pearson's R) higher than 0.95 (Figure 10), the obtained values were correlated to real Freundlich parameters.

Figure 10. Log-log plot of the concentration of zinc found in the *Phaseolus vulgaris* seed coat versus the concentration of each treatment. The straight lines give Pearson's R above 0.95. The parameters 1/n and Kf were calculated from the linearized form of the Freundlich isotherm equation

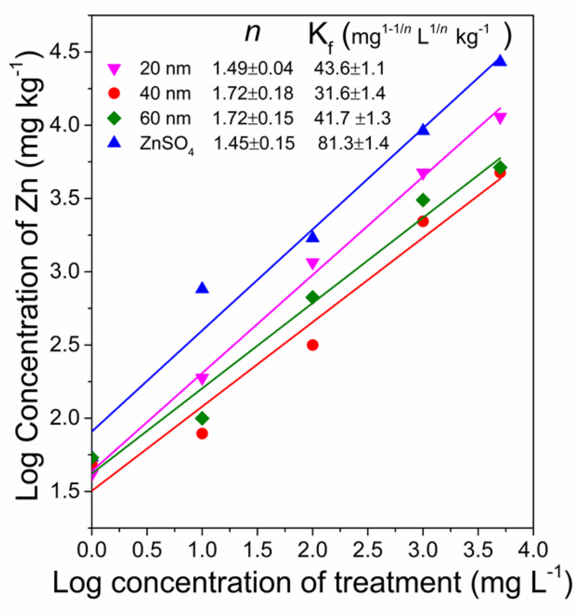

The *1/n* was similar for ZnO NP and $ZnSO_4$ treatments (Figure 10), but K_f values were between 31.6 and 43.6 mg$^{1-1/n}$ L$^{1/n}$ kg^{-1} for the different ZnO NP and 81.3 mg$^{1-1/n}$L$^{1/n}$ kg^{-1} for $ZnSO_4$. This indicates that the interaction strength between Zn and the seed coat was higher for $ZnSO_4$ than for the ZnO NP and for the latter not affected by nanoparticle size. This might be related to stronger binding of the ionic Zn compared to the ZnO NP.

Similar data processing and reasoning were followed for the data on Zn found in the germinated seedling. The log–log plots (not presented) showed a constant concentration of Zn in the seedlings for the treatments with ZnO NP between 1 and 100 mg L^{-1}, close to those found in the controls, indicating Zn was mostly trapped in the seed coat. The Zn content in the seedlings increased for ZnO NP treatment levels above 100 mg L^{-1}. In the case of $ZnSO_4$, the uptake of Zn by the inner part of the seed took place through two different regimes.

Figure 11 shows the pictures and the corresponding chemical images of the 2D location of Zn in the beans exposed to 20, 40, 60 nm ZnO NP (Figure 11 a) and $ZnSO_4$ (Figure 11 b) at 5000 mg L^{-1}. The images corroborate with the data obtained by quantitative EDXRF and show a Zn gradient from the seed coat toward the inner part of the cotyledon. The images also indicate the presence of Zn hotspots in the hilum region. The porous structure of this tissue allows, in addition to other structures, water entrance, radicle hydration, and the beginning of germination (MIANO et al., 2016). Figure 12 shows the quantitative analysis for a row of 16 points along the hilum region of a seed treated with 5000 mg L^{-1} $ZnSO_4$. The concentration of Zn is not homogeneous, it varied from 184 up to 10902 mg kg^{-1}. The three NP treatments also showed hotspots of Zn accumulation in the hilum region. So together these data show that the hilum structure might be the main entrance of Zn in the seed.

Figure 11. Pictures and zinc mapping of common bean (*Phaseolus vulgaris*) sections exposed to (a) 20, 40, 60 nm ZnO NP and (b) ZnSO4 at 5000 mg L^{-1}. The number of Zn K*α* photon counts is directly proportional to the Zn concentration. Zn hotspots were found in the seed coat, especially in the hilum

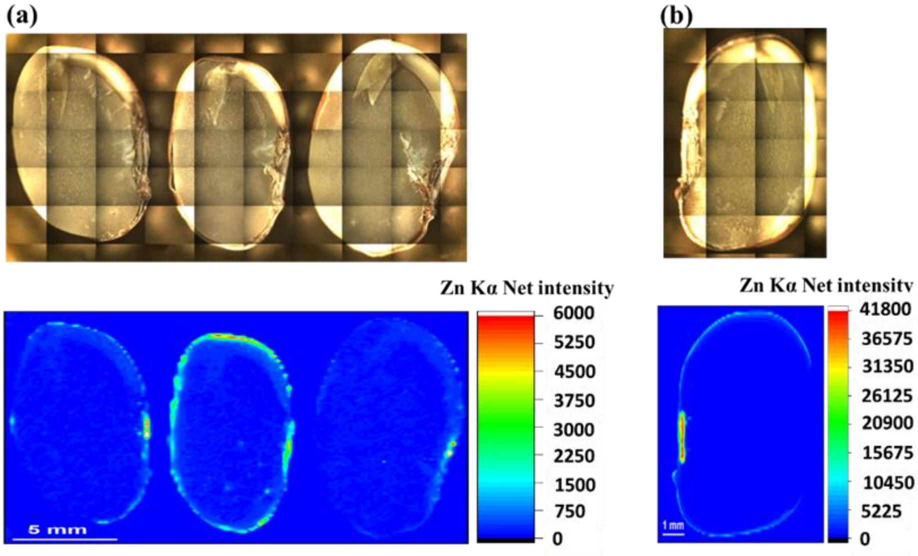

Figure 12. (a) picture of the *Phaseolus vulgaris* analyzed seed, the red line indicates the scanned region; (b) concentration of Zn (mg kg^{-1}) along the scanned point; (c) concentration of Zn determined by XRF versus the known concentration of Zn in standards

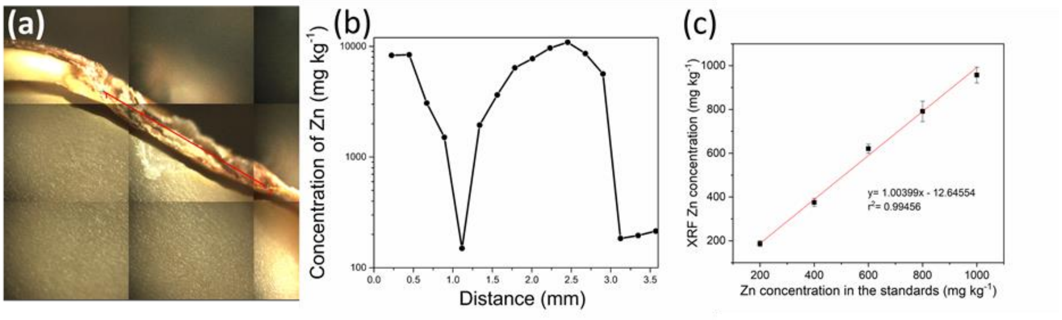

The quantification and chemical images also show that Zn seed priming can transfer the nutrient to the plant through two distinct mechanisms. First, the Zn can be absorbed by cells and might be available for use during germination and the first steps of seedling growth. Second, the Zn stuck to the outer part of the seed coat may be adsorbed by soil colloids and may be available for root absorption later. We did not find any other studies investigating the spatial distribution of Zn in the seed coat after seed priming.

2.3.4 Zinc Speciation

The quantitative assessment of the fraction of Zn species present in the seed is a challenging task. XANES spectra recorded in fluorescence geometry can be distorted by incident beam self-absorption (IBSA) that reduces the intensity amplitude of the fine structure. As a rule of thumb, it becomes visible when the sample concentration is high enough to record the spectra in transmission geometry (edge jump above ~0.1).

Figure 13 illustrates the effect of sample concentration on XANES spectra; it presents the spectra of pelletized Zn organic reference compounds at 0.2 and 1.0 Zn wt %. The energy in which the spectral features arises is the same regardless of the sample concentration; however, the intensities of their features, especially the white line (~9668 eV), the shoulder (~9684 eV), and the second absorption crest at ~9617 eV, are reduced in the 1 wt % references. An in-depth discussion of such effect, as well as the strategies to prevent and correct it, is outside the scope of the present study and can be found elsewhere (IIDA; NOMA, 1993; CARBONI et al., 2005).

Figure 13. (a) XANES spectra of Zn complexed to organic molecules. The data was recorded for 0.2 and 1.0 Zn wt.% cellulose pellets in fluorescence geometry and highlights the ISBA effect. (b) XANES spectra for ZnO NP recorded in fluoresce and transmission geometry, the IBSA is minimized by the Zn dilution. (c) XANES spectra for Zn-phytate and Zn-phosphate showing distinct features that were not observed in the spectra at the seeds

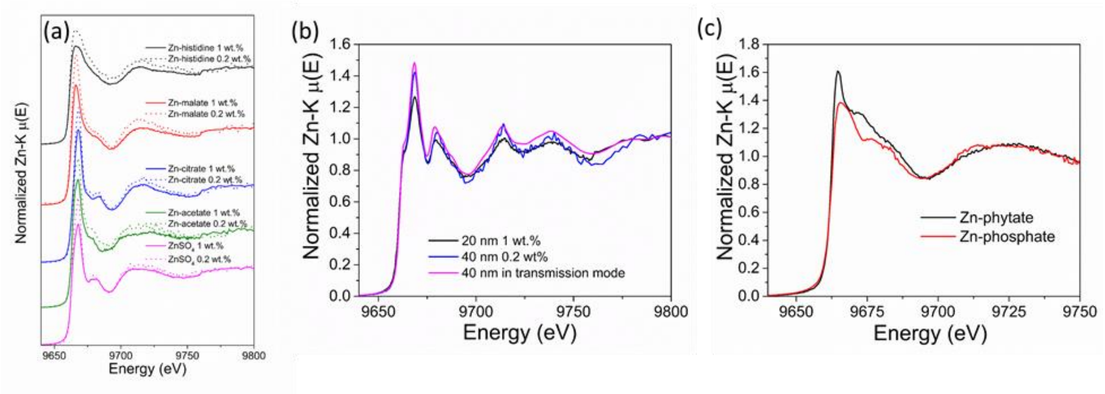

Aiming at avoiding such artifacts, we only performed LCF for the samples whose intensity of the feature at 9617 eV matched those of 0.2 wt % diluted standards. This spectral region was chosen because it is less sensitive to the chemical environment than the absorption edge. For all other samples we qualitatively explored the chemical environment based on the energy of the spectral features.

Another source of error in the LCF is the mismatch between the actual Zn chemical environment of the Zn incorporated by the seeds and that provided by the laboratory synthetized and pelletized reference compounds. Although the linear combination analysis indicated fractions of Zn-malate, it actually means that the Zn embedded in the sample presents a chemical environment similar to that of Zn-malate.

These compromises must be taken into account when investigating such complex biological matrices. In the context of this study, it is more important to unravel whether the incorporated Zn was biotransformed rather than providing the exact weight fractions of its constituents. The speciation was carried out using the seeds soaked in 5000 mg L^{-1} dispersions, which according to Figure 6 yielded Zn concentrations of 0.1−0.3 Zn wt % in the seed coat (except for the $ZnSO_4$ treatment). Additionally, due to the higher Zn concentrations in the sample in the latter treatment, the acquisition time for XANES measurements was shorter so that the sample was exposed to a lower radiation dose.

Figure 14 a show the points where the μ-XANES spectra were recorded for seeds soaked in the 5000 mg L^{-1} ZnO NP and $ZnSO_4$ solutions. The X-ray beam was focused on the outside, seed coat (hilum region), and inside the seed, and parts b−d of Figure 14 present the normalized XANES spectra recorded at these regions. The spectral features are a signature of the chemical environment. By overlapping the spectra measured on the sample with those recorded for reference compounds, one can infer the chemical environment of the Zn in the seed.

Figure 14 b shows that despite of intensity distortions attributed to ISBA, based on the matching of the energy of spectral features, one can state that the Zn present on the outside did not change compared to the pristine Zn salt and NP. The spectra recorded for $ZnSO_4$ and ZnO NP treated seeds presented similar features as the $ZnSO_4$ and ZnO NP references.

Figure 14 c shows the spectra measured on the seed coat. For the sample treated with $ZnSO_4$ the shoulder at 9680 eV is less intense than that of the $ZnSO_4$ reference compound, which suggests a different chemical environment. For the seeds treated with ZnO NP, the features at 9668 and 9679 eV allow detection of the presence of ZnO. The LCF indicated that 20 and 60 nm particles were biotransformed, and the spectra could be fitted as a mixture of ZnO and Zn-malate (Figure 15). The remaining fractions of ZnO were 78 ± 2 and 40 ± 2 for the 20 and 60 nm particles, respectively. The spectrum presented for the control seed presents similar features to that recorded for the Zn-histidine reference compound, which suggests that they have a comparable chemical neighborhood.

Inside the seed (cotyledon) (Figure 14 d), regardless of the treatment, the chemical environment of Zn was the same as for the seeds soaked in water, i.e., Zn-histidine-like chemical neighborhood. For the seeds soaked in 5000 mg L^{-1}, the quantitative XRF data showed a concentration of Zn inside the seed ranging from 187 up to 5975 mg kg^{-1}. These values were at least 5-fold higher than those found for the positive control seeds, suggesting biotransformation into Zn-histidine of the Zn incorporated within the seed. This kind of coordination was previously reported for Zn stored in cell vacuoles (KÜPPER et al., 1999). Despite the claimed ability of phytic acid to chelate divalent ions (LEE; KARUNANITHY, 1990), we did not find any evidence of the presence of Zn-\ phytate (spectrum shown in Figure 15 a).

Zn-malate reference compound represents a chemical environment in which Zn is surrounded by carboxyl groups, whereas histidine can complex it either via oxygen or nitrogen.

Extended X-ray absorption fine structure (EXAFS) analyses showed that Zn-malate is coordinated by four oxygen atoms in the first shell with interatomic distances of 2.01 Å, while the second one is composed by 2 carbon atoms at 2.80 Å (SARRET et al., 2002).

For Zn-histidine, the literature shows four N/O at nearly 2.06 Å and carbon second shell at ~3.00 Å (SARRET et al., 1998); however it is not clear whether the binding is realized via the carboxyl, amine or imidazole group.

Figure 14. Zn K edge XANES spectra recorded in different regions of common bean (*Phaseolus vulgaris*) seeds treated with 5000 mg L^{-1} dispersions of differently sized ZnO NP and $ZnSO_4$ solution: (a) picture of a bean seed highlighting the regions in which the spectra were recorded; (b) spectra recorded on the outside of the seed; (c) spectra recorded in the seed coat; (d) spectra recorded inside the seed

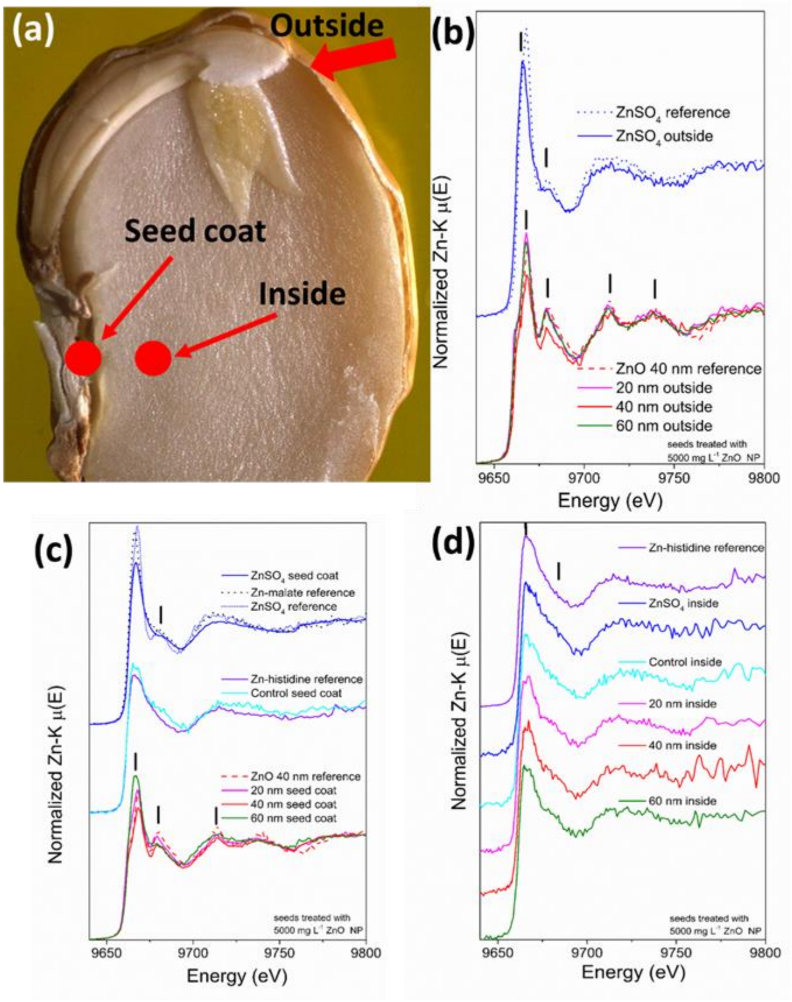

It is important to highlight that other organic acids present in the seed could produce chemical environments similar to those of Zn-malate and Zn-histidine. Although most of the incorporated Zn atoms were binding carboxyl, the presence of ZnO components in the linear combination analysis indicated the possible diffusion of nanoparticles through the spongy hilum tissue.

Figure 15. Linear combination fit for Zn-K edge XAS spectra recorded (a) outside and (b) at the seed coat-inside of a bean seed treated with 40 nm ZnO NP at 100 mg L^{-1}; Linear combination fit for the spectra recorded at the seed coat of the seed treated with 5000 mg L^{-1} of (c) 20 nm and (d) 60 nm ZnO; Linear combination fit for the spectra recorded at the primary root of the seedling whose seed was treated with (e) 20 nm, (f) 60 nm ZnO and (g) control root

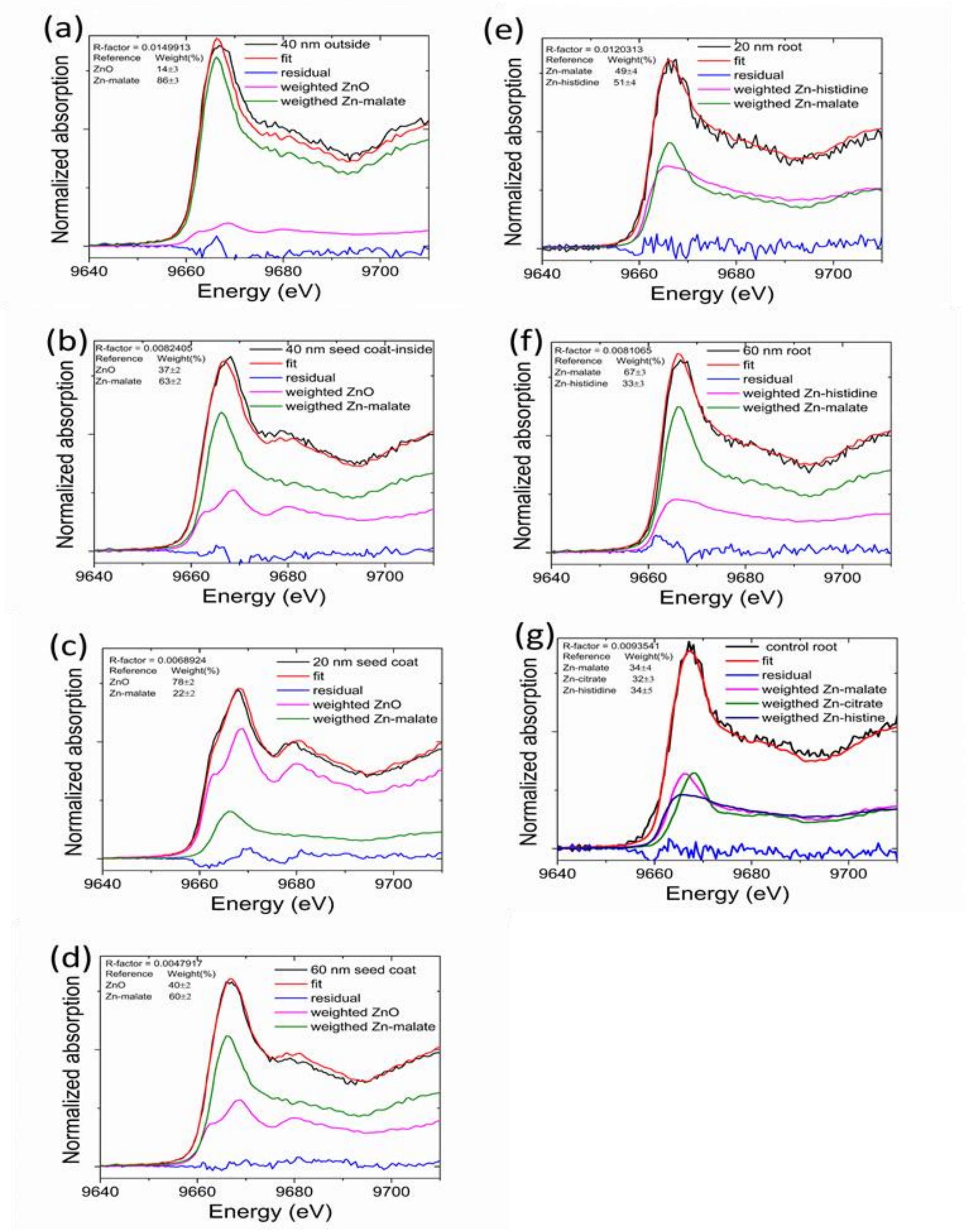

The seedling weight gain was influenced not only by the Zn concentration of the treatments but also by the size of the particles. Figure 16 presents the seedling weight gain as a function of the Zn concentration in the seed coat (Figure 16 a) and in the inner seed part (Figure 16 b). Figure 16 a show that the seedling weight gain tended to decrease for Zn concentrations in the seed coat above 1000 mg Zn kg^{-1}. This holds for the $ZnSO_4$ and 20 nm ZnO treatments but not for 40 nm ZnO, even though the seed coat incorporated as much as 4760 ± 140 mg Zn kg^{-1} upon exposure to this nanoparticle size.

Figure 16. Relation between weight gain of common bean seeds and different concentrations of Zn found in the seed coat (a) and inside the seed (b)

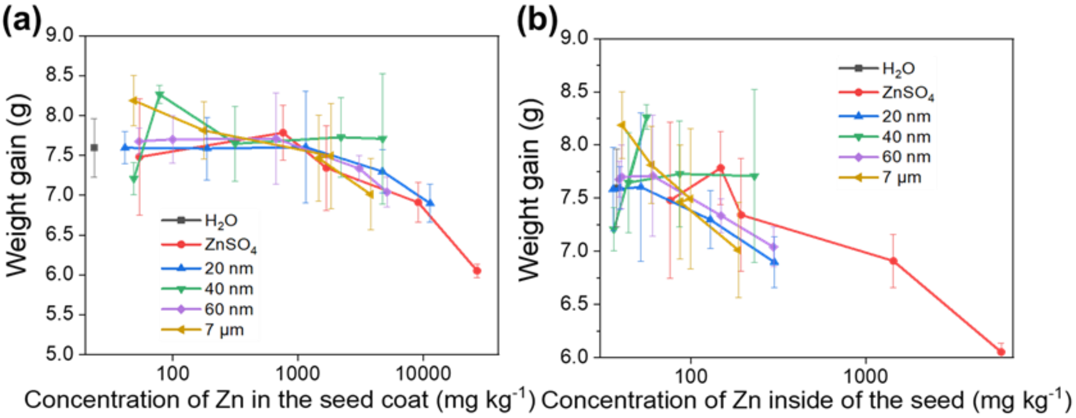

The data from Figure 15 a combined with the XANES fingerprints suggest that the reduction of weight, i.e., the deleterious effects, did not only depend on the amount of Zn absorbed by the seed. Although it was not possible to quantify the Zn fractions in the 40 nm ZnO treated seed, most of the Zn trapped in the seed coat remained in the ZnO form (Figure 14 c), while most of the Zn from $ZnSO_4$ and 20 nm ZnO was biotransformed into an organic Zn form (Figure 14 c and Table 7). Therefore, besides being metabolized by seedlings and bound to organic molecules (RICACHENEVSKY et al., 2015), i.e., malate or histidine, the Zn may also be stored in cell vacuoles and could be used along the plant development (SINCLAIR; KRÄMER, 2012).

Figure 17 a show the XANES spectra recorded on the outside of the seed coat and on the interface between seed coat and cotyledon for a seed soaked in the 100 mg L^{-1} 40 nm ZnO NP dispersion. Figure 17 b and Figure 17 c present pictures indicating the location of the measurements. The spectra uncovered the presence of mixtures of pristine ZnO and Zn-malate (Figure 15 a and Figure 15 b). The relative proportions of the compounds in the mixtures are presented in Table 7.

Table 7. Linear Combination Fittings for the XANES Spectra Recorded for Seeds and Seedlings of Common Beans (*Phaseolus vulgaris*) Treated with $ZnSO_4$ and Differently Sized ZnO NP[a]

Analysed sample region	**Percent composition**				**R-factor (x10^{-3})**
	ZnO	Zn-malate	Zn-histidine	Zn-citrate	
5000 mg L^{-1} 20 nm seed coat	78±2	22±2			6.9
5000 mg L^{-1} 60 nm seed coat	40±2	60±2			4.8
100 mg L^{-1} 40 nm outside	14±3	86±3			15.0
100 mg L^{-1} 40 nm seed coat-inside	37±2	63±2			8.2
Control		34±4	34±5	32±3	9.3
1000 mg L^{-1} 20 nm root		49±4	51±4		12.0
1000 mg L^{-1} 60 nm root		67±3	33±3		8.1

[a] R-factor = $\frac{\sum(data-fit)^2}{\sum(data)^2}$; The fitted curves and reference compounds are presented in Figures 13 and S15, respectively. Each XANES spectrum was obtained from the merging of three replicate spectra.

Figure 17. Zn K edge XAS spectra recorded in different regions of common bean (*Phaseolus vulgaris*) seeds treated with a 100 mg L^{-1} 40 nm ZnO NP dispersion: (a) picture of a bean seed highlighting the regions in which the spectra were recorded; (b) spectra recorded on the outside of the bean and in the middle region between the seed coat and the inside

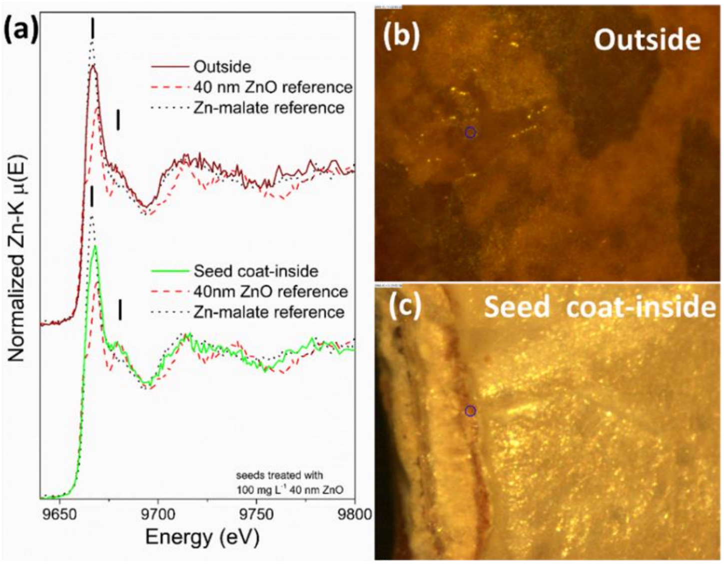

Different from the seeds soaked in 5000 mg L^{-1} dispersions, the low concentration treatment presented a smaller fraction of ZnO adsorbed on the outside of the seed coat. ZnO was found at the interface of the seed coat cotyledon, which means that nanoparticles could migrate from the dispersion and that part of them were biotransformed. Since ZnO is partially soluble (Figure 3) and some studies even indicate that the solubility increases for nanomaterials, it is still not clear if the biotransformed Zn comes from Zn(aq) that coexisted in dispersion and which was eventually coordinated by the organic compounds (MUDUNKOTUWA et al., 2011). The alternative hypothesis is that ZnO NPs were dissolved inside the hilum and complexed by malate and citrate-like compounds.

The μ-XANES facility was also used to probe the local chemical environment of the Zn in the radicle of seedlings on the fifth day of the germination experiment. Figure 18 a present the spectra recorded for samples treated with 1000 mg L^{-1} ZnO NP dispersions, for a control seedling germinated in water, and for the synthetic Zn-malate, Zn-citrate, and Zn-histidine reference compounds. The linear combination analysis is presented in Table 7, while the fitted spectra are shown in Figure S15.

Figure 18. Zn-K edge XANES spectra recorded in the root of a common bean (*Phaseolus vulgaris*) seedling on the fifth day of germination following exposure to 1,000 mg L^{-1} ZnO NP dispersions. (a) Spectra recorded for a control root, Zn-malate, Zn-citrate and for the seedlings previously treated with 20 nm, 40 nm and 60 nm ZnO NP. The blue circle in (b) and (c) show the points where the spectra for the 20 nm and40 nm ZnO were recorded, respectively

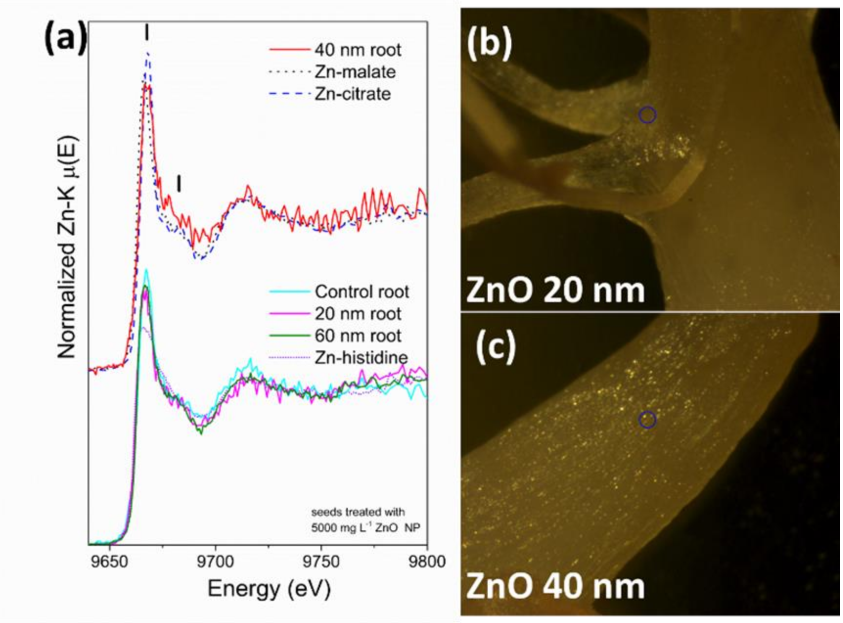

The non-normalized spectra consistently showed that the amount of Zn was higher in roots of treated seeds compared to the control one. The spectra for the control root and that treated with 40 nm ZnO were slightly higher than the line compared to the 20 and 60 nm ZnO treated ones. The spectrum for the control root could only be fitted with the addition of Zn-citrate component. The addition of this third component did not promote a significant decrease of the R-factor disagreement parameter.

Even though the seeds were germinated on filter paper moistened with ZnO NP dispersion, the data did not point out the presence of ZnO associated with the root. Such association was shown by (WANG et al., 2013), who found that ~65% of the Zn present in the roots of *Vigna unguiculata* was in ZnO form when seedling was exposed to a 25 mg L^{-1} ZnO NP dispersion for 4 weeks. In the present study the roots were washed before to the analysis; thus any ZnO adsorbed on the outer part of the root might have been removed.

Figure 19 shows representative SEM images recorded for cross sections of the primary root of *Phaseolus vulgaris* seedling treated with 100 and 1000 mg L^{-1} ZnO dispersions. The treatments did not cause any apparent damage in the cells of cortex and stele regions. On the contrary, the presence of the felogen tissue, i.e., a secondary growth structure, on the treated roots suggests that they developed faster than the control one. The micrographs show changes at the root hairs that are an outgrowth structure from the epidermis cells. The images show that the 100 mg L^{-1} treatments induced the hair growth for ZnO 20 nm (Figure 19 c and Figure 19 d) and 60 nm (Figure 19 h and Figure 19 l) compared to the control. Conversely, the 1000 mg L^{-1} treatments decreased the number and length of root hairs, with the exception of ZnO 20 nm (Figure 19 h and Figure 19 f). The most deleterious treatment was $ZnSO_4$ (Figure 19 q and Figure 19 r). It seems that the outer tissues were more affected by the treatments than the inner ones.

Finally, the present study fosters the potential use of NP in plant nutrition. Due to the NP peculiar behavior, it has the potential to act differently from the bulk chemical form, allowing a slower nutrient release compared to salts and faster release compared to the bulk counterpart. It is suitable particularly for micronutrients, in which the amount required is minimum and its toxicity, even at minor levels, is a matter of concern. To the authors' best knowledge, there is no clear sharp reasoning in the literature on the effect of the 20−60 nm nanoparticle size range on seed germination. Since the present work focused on the chemical speciation of Zn present in the seed coat and roots and their effects on total seedling weight gain, additional studies are necessary to uncover the effects of Zn on the development of other seedling parts such as the plumule and embryo axis.

Figure 19. Scanning electron micrographs of transversal section of primary roots of *Phaseolus vulgaris*. The sections were cut 5 days after germination: (a, b) control plants (soaked in water); (c, d) ZnO 20 nm 100 mg L^{-1}; (e, f) ZnO 20 nm 1000 mg L^{-1}; (g, h) ZnO 40 nm 100 mg L^{-1}; (i, j) ZnO 40 nm 1000 mg L^{-1}; (k, l) ZnO 60 nm 100 mg L^{-1}; (m, n) ZnO 60 nm 1000 mg L^{-1}; (o, p) ZnSO4 100 mg L^{-1}; (q, r) ZnSO4 1000 mg L^{-1}; H, root hairs; F, felogen

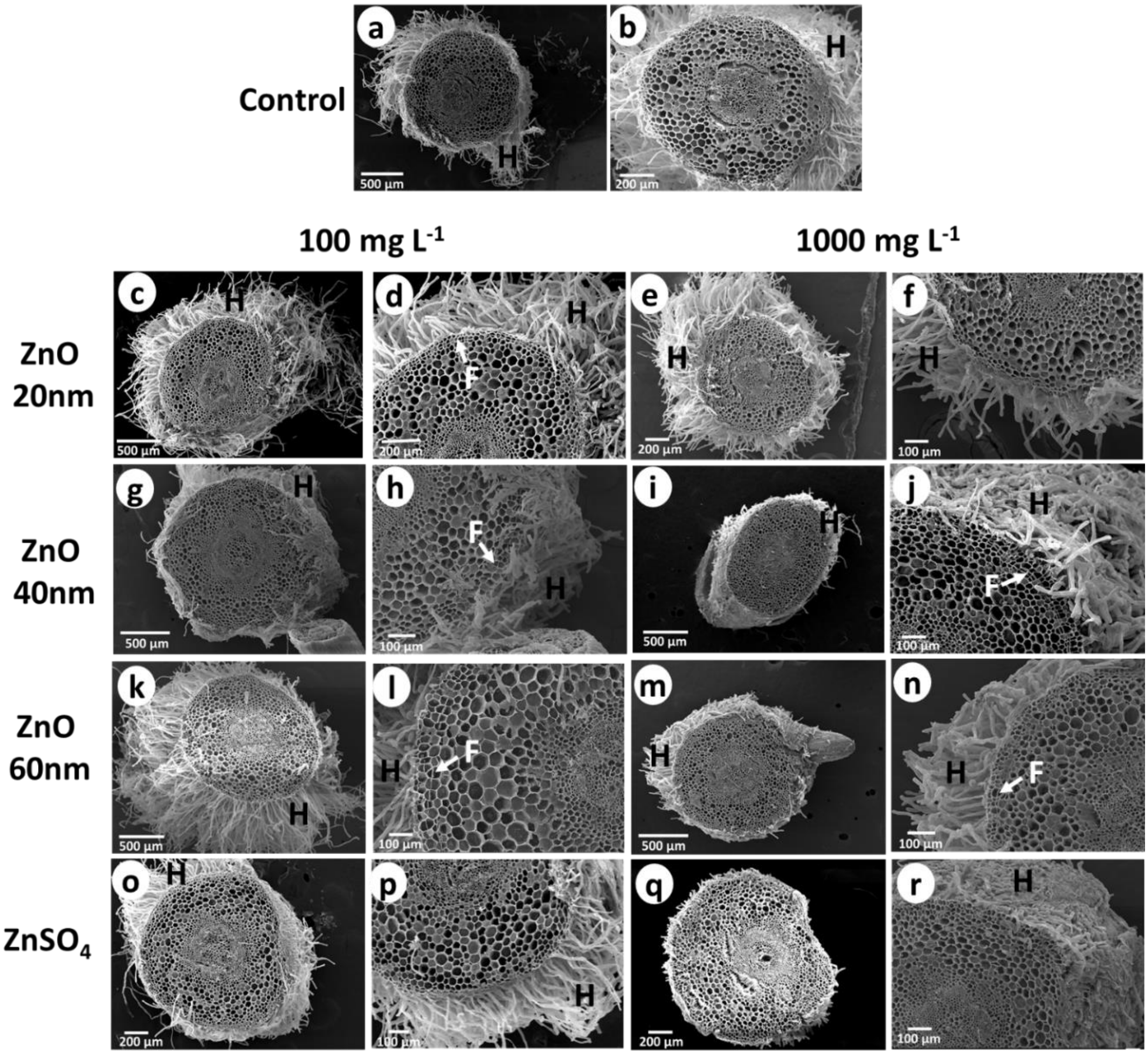

2.4 Conclusion

The weight gain, after the fifth day of germination, of *Phaseolus vulgaris* bean seeds was unequivocally affected by exposure to 20 nm ZnO NP and ZnSO4 at 5000 mg L^{-1}. None of the other ZnO NP treatments harmed seed germination and seedling development.

At an exposure level of 10 mg L^{-1} of both $ZnSO_4$ and ZnO NP, Zn was transferred to the inner part of the seeds. At 1 mg L^{-1}, the lowest exposure concentration, the Zn provided by the nanoparticles stayed in the seed coat and only in the case of $ZnSO_4$ did the Zn taken up reach the cotyledon.

For all treatments, most of the Zn (51−97%) was trapped in the seed coat. The amount of Zn absorbed by the seed followed an asymptotic function of the concentration, suggesting a saturation of the Zn adsorption sites at high exposure concentrations. The Zn uptake was facilitated for $ZnSO_4$ which is present as Zn^{2+} ions in solution. The μ-XRF showed the presence of Zn hotspots in the hilum region presenting a concentration gradient from the outer to the inner part of the seed.

Zn K edge μ-XANES showed that in the seed coat a fraction of Zn taken up from ZnO NP was present as ZnO, while part as biotransformed to Zn coordinated to organic molecules. The chemical speciation showed that ZnO NP neither entered the cotyledon nor was incorporated into the primary root.

Altogether, at a proper concentration and size, ZnO NP may be a suitable form of Zn to be used for *Phaseolus vulgaris* seed priming. Such ZnO NP form supplied Zn to the bean seeds, and additionally Zn was biotransformed into Zn bound to organic molecules. Compared to $ZnSO_4$ at similar concentrations, the ZnO NP presents the advantage of lower toxicity and provides a slow and controlled Zn delivering. In comparison with the bulk ZnO, the NP has the advantage of a greater active surface, thus minimizing the loss of this finite and limited resource nutrient in crop applications. Additionally, this study only evaluated the ZnO NP effect on the germination stage of the common bean. Further studies monitoring the effects of the treatments on plant development, grain production, Zn content, and speciation in other tissues are currently being carried out by our group and will soon be communicated.

References

AJOURI, A.; ASGEDOM, H.; BECKER, M. Seed priming enhances germination and seedling growth of barley under conditions of P and Zn deficiency. **Journal of Plant Nutrition and Soil Science**, Weinheim, v. 167, n. 5, p. 630–636, 2004.

BEAL, T.; MASSIOT, E.; ARSENAULT, J. E.; SMITH, M. R.; HIJMANS, R. J. Global trends in dietary micronutrient supplies and estimated prevalence of inadequate intakes. **Plos One**, San Francisco , v. 12, n. 4, p. e0175554, 2017.

BIAN, S.-W.; MUDUNKOTUWA, I. A.; RUPASINGHE, T.; GRASSIAN, V. H. Aggregation and dissolution of 4 nm ZnO nanoparticles in aqueous environments: influence of ph, ionic strength, size, and adsorption of humic acid. **Langmuir**, Washington, DC, v. 27, n. 10, p. 6059–6068, 2011.

CAKMAK, I. Possible roles of zinc in protecting plant cells from damage by reactive oxygen species. **New Phytologist**, Oxford ,v. 146, n. 2, p. 185–205, 2000.

CALVIN, S. **XAFS for Everyone**. CRC Press, Florida, 2013.

CARBONI, R.; GIOVANNINI, S.; ANTONIOLI, G.; BOSCHERINI, F. Self absorption correction strategy for fluorescenceyield soft X-ray near edge spectra. **Physica Scripta**, Stockholm, v. 2005, p. 986, 2005. doi: 10.1238/Physica.Topical.115a00986.

CASTILLO-MICHEL, H. A.; LARUE, C.; PRADAS DEL REAL, A. E.; COTTE, M.; SARRET, G. Practical review on the use of synchrotron based micro and nano X-ray fluorescence mapping and X-ray absorption spectroscopy to investigate the interactions between plants and engineered nanomaterials. **Plant Physiology and Biochemistry**, Amsterdam, v. 110, p. 13–32, 2017.

CRUZ, T. N. M. da; SAVASSA, S. M.; GOMES, M. H. F.; RODRIGUES, E. S.; DURAN, N. M.; ALMEIDA, E. de; MARTINELLI, A. P.; CARVALHO, H. W. P. de. Shedding light on the mechanisms of absorption and transport of ZnO nanoparticles by plants via in vivo X-ray spectroscopy. **Environmental Science: Nano**, London, v. 4, p. 2367-2376, 2017.

DURAN, N. M.; SAVASSA, S. M.; LIMA, R. G. D.; ALMEIDA, E. de; LINHARES, F. S.; VAN GESTEL, C. A. M.; CARVALHO, H. W. P. de. X-ray spectroscopy uncovering the effects of Cu based nanoparticle concentration and structure on *Phaseolus vulgaris* germination and seedling development. **Journal of Agricultural and Food Chemistry**, Washington, DC, v. 65, n. 36, p. 7874-7884, 2017.

EKIZ, H.; BAGCI, S. A.; KIRAL, A. S.; et al. Effects of zinc fertilization and irrigation on grain yield and zinc concentration of various cereals grown in zinc-deficient calcareous soils. **Journal of Plant Nutrition**, New York , v. 21, n. 10, p. 2245–2256, 1998.

FARIA, L. C. de.; Del PELOSO, M. J.; MELO, L. C.; COSTA, J. G. C. da; RAVA, C. A.; DÍAZ, J. A. L.; FARIA, J. C.; SILVA, H. T. da; SARTORATO, A. S.; BASSINELLO, P. S.; TROVO, J. B. CULTIVAR RELEASE-BRS Cometa: a carioca common bean cultivar with erect growth habit. **Crop Breeding and Applied Biotechnology**, Lismore, v. 8, p. 167-169, 2008.

FAROOQ, M.; WAHID, A.; SIDDIQUE, K. H. M. Micronutrient application through seed treatments: a review. **Journal of Soil Science and Plant Nutrition**, Temuco, v. 12, n. 121, p. 125–142, 2012.

GRIFFIN, B. A.; JURINAK, J. J. Estimation of activity coefficients from the electrical conductivity of natural aquatic systems and soil extracts. **Soil Science**, Baltimore, v. 116, n. 1, p. 26-30, 1973.

GUERINOT, M. L. The ZIP family of metal transporters. **Biochimica et Biophysica Acta (BBA) - Biomembranes**, Amsterdam, v. 1465, n. 1–2, p. 190–198, 2000.

HAMDAOUI, O.; NAFFRECHOUX, E. Modeling of adsorption isotherms of phenol and chlorophenols onto granular activated carbon: Part I. Two-parameter models and equations allowing determination of thermodynamic parameters. **Journal of Hazardous Materials**, Amsterdam, v. 147, n. 1, p. 381–394, 2007.

HERNANDEZ-VIEZCAS, J. A.; CASTILLO-MICHEL, H.; SERVIN, A. D.; PERALTA-VIDEA, J. R.; GARDEA-TORRESDEY, J. L. Spectroscopic verification of zinc absorption and distribution in the desert plant Prosopis juliflora-velutina (velvet mesquite) treated with ZnO nanoparticles. **Chemical Engineering Journal**, Lausanne, v. 170, n. 1–3, p. 346–352, 2011.

HONG, J.; PERALTA-VIDEA, J. R.; GARDEA-TORRESDEY, J. L. Nanomaterials in agricultural production: benefits and possible threats?. **Sustainable Nanotechnology and the Environment: Advances and Achievements**, Washington, dc, v. 1124, p. 5–73, 2013.

IIDA, A.; NOMA, T. Correction of the self-absorption effect in fluorescence X-Ray absorption fine structure. **Japanese Journal of Applied Physics**, Tokyo, v. 32, n. 6A, p. 2899–2902, 1993.

IWAI, T.; TAKAHASHI, M.; ODA, K.; TERADA, Y.; YOSHIDA, K. T. Dynamic changes in the distribution of minerals in relation to phytic acid accumulation during rice seed development. **Plant Physiology**, Rockville, v. 160, p. 2007–2014, 2012.

JAMES, S. A.; HARE, D. J.; JENKINS, N. L.; DE JONGE, M. D.; BUSH, A. I.; McCOLL, G. φXANES: In vivo imaging of metal-protein coordination environments. **Scientific Reports**, London, v. 6, p. 20350, 2016.

KARNOVSKY, M. J. A. formaldehyde-glutaraldehyde fixative of high osmolality for use in electron microscopy. **The Journal of Cell Biology**, New York, v. 27, n. 2, p. 1A-149A, 1965.

KHODAKOVSKAYA, M. V.; KIM, B. S.; KIM, J. N.; ALIMOHAMMADI, M.; DERVISHI, E.; MUSTAFA, T.; CERNIGLA, C. E. Carbon nanotubes as plant growth regulators: effects on tomato growth, reproductive system, and soil microbial community. **Small**, Weinheim, v. 9, n. 1, p. 115–123, 2013.

KIM, J. H.; OH, Y.; YOON, H.; HWANG, I.; CHANG, Y.-S. Iron nanoparticle-induced activation of plasma membrane H(+)-ATPase Promotes stomatal opening in Arabidopsis thaliana. **Environmental Science & Technology**, Washington, DC, v. 49, n. 2, p. 1113–1119, 2015.

KUMSSA, D. B.; JOY, E. J. M.; ANDER, E. L.; WATTS, M. J.; YOUNG, S. D.; WALKER, S.; BROADLEYE, M. R. Dietary calcium and zinc deficiency risks are decreasing but remain prevalent. **Scientific Reports**, London, v. 5, p. 10974, 2015.

KÜPPER, H.; ZHAO, F. J.; MCGRATH, S. P. Cellular compartimentation of zinc in the leaves of the hyperaccumulator Thlaspi caerulescens. **Plant Physiology**, Rockville, v. 212, p. 75–84, 1999.

LARUE, C.; CASTILLO-MICHEL, H.; SOBANSKA, S.; TRCERA, N.; SORIEUL, S.; CÉCILLON, L.; OUERDANE, L.; LEGROS, S.; SARRET, G. Fate of pristine TiO_2 nanoparticles and aged paint-containing TiO_2 nanoparticles in lettuce crop after foliar exposure. **Journal of Hazardous Materials**, Amsterdam, v. 273, p. 17–26, 2014.

LAVRES, J.; CASTRO FRANCO, G.; SOUSA CÂMARA, G. M. de. Soybean seed treatment with nickel improves biological nitrogen fixation and urease activity. **Frontiers in Environmental Science**, Lausanne, n. 4, p. 1-11, 2016.

LEE, C. K.; KARUNANITHY, R. Effects of germination on the chemical composition of Glycine and Phaseolus beans. **Journal of the Science of Food and Agriculture**, Chichester, v. 51, n. 4, p. 437–445, 1990.

LIU, K.; NIU, Y.; KONISHI, M.; WU, Y.; DU, H.; SUN CHUNG, H.; LI, L.; BOUDSOCQ, M.; MCCORMACK, M.; MAEKAWA, S.; ISHIDA, T.; ZHANG, C.; SHOKAT, K.; YANAGISAWA, S.; SHEEN, J. Discovery of nitrate–CPK–NLP signalling in central nutrient growth networks. **Nature**, London, v. 545, p. 311, 2017.

LUYTS, K.; NAPIERSKA, D.; NEMERY, B.; HOET, P. H. M. How physico-chemical characteristics of nanoparticles cause their toxicity: complex and unresolved interrelations. **Environmental Sciences: Processes and Impacts**, Cambridge, v. 15, n. 1, p. 23–38, 2013.

MARQUES, J. P. R.; APPEZZATO-DA-GLÓRIA, B.; PIEPENBRING, M.; MASSOLA JUNIOR, N. S.; MONTEIRO-VITORELLO, C. B.; VIEIRA, M. L. C. Sugarcane smut: shedding light on the development of the whip-shaped sorus. **Annals of Botany**, Oxford, v. 119, n. 5, p. 815–827, 2017.

MIANO, A. C.; PEREIRA, J. da C.; CASTANHA, N.; JÚNIOR, M. D. da M.; AUGUSTO, P. E. D. Enhancing mung bean hydration using the ultrasound technology: description of mechanisms and impact on its germination and main components. **Scientific Reports**, London, v. 6, n. 1, p. 38996, 2016.

MUDUNKOTUWA, I. A; RUPASINGHE, T.; WU, C. M.; GRASSIAN, V. H. Dissolution of ZnO nanoparticles at circumneutral pH: a study of size effects in the presence and absence of citric acid. **Langmuir**, Washington, DC, v. 28, n. 1, p. 396–403, 2011.

MUHAMMAD, I.; KOLLA, M.; VOLKER, R.; GÜNTER, N. Impact of nutrient seed priming on germination, seedling development, nutritional status and grain yield of maize. **Journal of Plant Nutrition**, New York, v. 38, n. 12, p. 1803–1821, 2015.

OZTURK, L.; YAZICI, M. A.; YUCEL, C.; TORUN, A.; CEKIC, C.; BAGCI, A.; OZKAN, H.; BRAUN, H.J.; SAYERS, Z.; CAKMAK, I. Concentration and localization of zinc during seed development and germination in wheat. **Physiologia Plantarum**, Hoboken, v. 128, n. 1, p. 144–152, 2006.

PANDEY, A. C.; SANJAY, S. S.; YADAV, R. S. Application of ZnO nanoparticles in influencing the growth rate of Cicer arietinum. **Journal of Experimental Nanoscience**, Abingdon, v. 5, n. 6, p. 488–497, 2010.

PÉREZ, C. A.; RADTKE, M.; SÁNCHEZ, H. J.; TOLENTINO, H.; NEUENSHWANDER, R. T.; BARG, W.; RUBIO, M.; BUENO, M. I. S.; RAIMUNDO, I. M.; ROHWEDDER, J. R. R. Synchrotron radiation X-Ray fluorescence at the LNLS: beamline instrumentation and experiments. **X-Ray Spectrometry**, Hoboken, v. 28, n. 5, p. 320–326, 1999.

PETERS, R. J. B.; BOUWMEESTER, H.; GOTTARDO, S.; AMENTA, V.; ARENA, M.; BRANDHOFF, P.; MARVIN, H. J. P.; MECH, A.; MONIZ, F. B.; PESUDO, L. Q.; RAUSCHER, H.; SCHOONJANS, R.; UNDAS, A. K.; VETTORI, M. V.; WEIGEL, S.; ASCHBERGER, K. Nanomaterials for products and application in agriculture, feed and food. **Trends in Food Science & Technology**, Cambridge, v. 54, p. 155–164, 2016.

PRASAD, T. N. V. K. V.; SUDHAKAR, P.; SREENIVASULU, Y.; LATHA, P.; MUNASWAMY, V.; RAJA REDDY, K.; SREEPRASAD, T. S.; SAJANLAL, P. R.; PRADEEP, T. Effect of nanoscale zinc oxide particles on the germination, growth and yield of peanut. **Journal of Plant Nutrition**, New York, v. 35, n. 6, p. 905–927, 2012.

PROM-U-THAI, C.; RERKASEM, B.; YAZICI, A.; CAKMAK, I. Zinc priming promotes seed germination and seedling vigor of rice. **Journal of Plant Nutrition and Soil Science**, Weinheim, v. 175, n. 3, p. 482–488, 2012.

RATNIKOVA, T. A.; PODILA, R.; RAO, A. M.; TAYLOR, A. G. Tomato seed coat permeability to selected carbon nanomaterials and enhancement of germination and seedling growth. **The Scientific World Journal**, New York, v. 2015, p. 419215, 2015.

RAVEL, B.; NEWVILLE, M. ATHENA, ARTEMIS, HEPHAESTUS: Data analysis for X-ray absorption spectroscopy using IFEFFIT. **Journal of Synchrotron Radiation**. Copenhagen, v. 12, p. 537–541, 2005.

REED, R. B.; LADNER, D. A.; HIGGINS, C. P.; WESTERHOFF, P.; RANVILLE, J. F. Solubility of nano-zinc oxide in environmentally and biologically important matrices. **Environmental Toxicology and Chemistry / SETAC**, Pensacola, v. 31, n. 1, p. 93–99, 2012.

RICACHENEVSKY, F. K.; MENGUER, P. K.; SPEROTTO, R. A.; FETT, J. P. Got to hide your Zn away: molecular control of Zn accumulation and biotechnological applications. **Plant Science**, Clare, v. 236, p. 1–17, 2015.

RICO, C. M.; HONG, J.; MORALES, M. I.; ZHAO, L.; BARRIOS, A. C.; ZHANG, J. Y.; PERALTA-VIDEA, J. R.; GARDEA-TORRESDEY, J. L. Effect of cerium oxide nanoparticles on rice: a study involving the antioxidant defense system and in vivo fluorescence imaging. **Environmental Science & Technology**, Washington, DC, v. 47, n. 11, p. 5635–5642, 2013.

RICO, C. M; MORALES, M. I.; BARRIOS, A. C.; MCCREARY, R.; HONG, J.; LEE, W. Y.; NUNEZ, J.; PERALTA-VIDEA, J. R.; GARDEA-TORRESDEY, J. L. Effect of cerium oxide nanoparticles on the quality of rice (Oryza sativa L.) grains. **Journal of Agricultural and Food Chemistry**, Washington, DC, v. 61, n. 47, p. 11278–11285, 2013.

SABIR, S.; ARSHAD, M.; CHAUDHARI, S. K. Zinc oxide nanoparticles for revolutionizing agriculture: synthesis and applications. **Scientific World Journal**, New York, v. 2014, 2014.

SALAH, S. M.; YAJING, G.; DONGDONG, C.; JIE, L.; AAMIR, N.; QIJUAN, H.; WEIMIN, H.; MINGYU, N.; JIN, H. Seed priming with polyethylene glycol regulating the physiological and molecular mechanism in rice (Oryza sativa L.) under nano-ZnO stress. **Scientific Reports**, London, v. 5, n. 1, p. 14278, 2015.

SARRET, G.; MANCEAU, A.; SPADINI, L.; ROUX, J.-C.; HAZEMANN, J.-L.; SOLDO, Y.; EYBERT-BÉRARD, L.; MENTHONNEX, J.-J. Structural determination of Zn and Pb binding sites in penicillium chrysogenum cell walls by EXAFS spectroscopy. **Environmental Science & Technology**, Washington, DC, v. 32, n. 11, p. 1648–1655, 1998.

SARRET, G.; SAUMITOU-LAPRADE, P.; BERT, V.; PROUX, O.; HAZEMANN, J. L.; TRAVERSE, A.; MARCUS, M. A.; MANCEAU, A. Forms of zinc accumulated in the hyperaccumulator Arabidopsis halleri. **Plant Physiology**, Rockville, v. 130, n. 4, p. 1815–1826, 2002.

SARRET, G.; WILLEMS, G.; ISAURE, M. P.; MARCUS, M. A.; FAKRA, S. C.; FRÉROT, H.; PAIRIS, S.; GEOFFROY, N.; MANCEAU, A.; SAUMITOU-LAPRADE, P. Zinc distribution and speciation in Arabidopsis halleri x Arabidopsis lyrata progenies presenting various zinc accumulation capacities. **New Phytologist**, Oxford, v. 184, n. 3, p. 581–595, 2009.

SILLANPÄÄ, M. **Micronutrients and the nutrient status of soils**: a global study. Rome: FAO, 1982. (FAO Soils Bulletin, 48).

SINCLAIR, S. A.; KRÄMER, U. The zinc homeostasis network of land plants. **Biochimica et Biophysica Acta (BBA) - Molecular Cell Research**, Amsterdam, v. 1823, n. 9, p. 1553–1567, 2012.

TAVARES, L. C.; RUFINO, C. de A.; BRUNES, A. P.; FRIEDRICH, F. F.; BARROS, A. C. S. A.; VILLELA, F. A. Physiological performance of wheat seeds coated with micronutrients . **Journal of Seed Science**, Lismore, v. 35, n. 1, p. 28-34, 2013.

TIAN, J.; WONG, K. K.; HO, C.-M.; LOK, C. N.; YU, W. Y.; CHE, C. M.; CHIU, J. F.; TAM, P. K. Topical delivery of silver nanoparticles promotes wound healing. **ChemMedChem**, Weinheim, v. 2, n. 1, p. 129–136, 2007.

TIBSHIRANI, R. Regression shrinkage and selection via the lasso. **Journal of the Royal Statistical Society. Series B - Methodological**, London, v. 58, n. 1, p. 267–288, 1996.

TOPLAK, M.; BIRARDA, G.; READ, S.; SANDT, C.; ROSENDAHL, S. M.; VACCARI, L.; DEMŠAR, J.; BORONDICS, F. Infrared orange: connecting hyperspectral data with machine learning. **Synchrotron Radiation News**, New York, v. 30, n. 4, p. 40–45, 2017.

WANG, M.; TANG, X.; ZHANG, H.; ZHOU, B. Nutrient enrichment outweighs effects of light quality in Zostera marina (eelgrass) seed germination. **Journal of Experimental Marine Biology and Ecology**, Amsterdam, v. 490, p. 23–28, 2017. Supplement C.

WANG, P.; MENZIES, N. W.; LOMBI, E.; McKENNA, B. A.; JOHANNESSEN, B.; GLOVER, C. J.; KAPPEN, P.; KOPITTKE, P. M. Fate of ZnO nanoparticles in soils and Cowpea (*Vigna unguiculata*). **Environmental Science & Technology**, Washington, DC, v. 47, n. 23, p. 13822–13830, 2013.

WANG, P.; MENZIES, N. W.; LOMBI, E.; SEKINE, R.; BLAMEY, F. P.; HERNANDEZ-SORIANO, M. C.; CHENG, M.; KAPPEN, P.; PEIJNENBURG, W. J.; TANG, C.; KOPITTKE, P. M. Silver sulfide nanoparticles (Ag_2S-NPs) are taken up by plants and are phytotoxic. **Nanotoxicology**, London, v. 9, n. 8, p. 1041–1049, 2015.

WANG, X.; YANG, X.; CHEN, S.; LI, Q.; WANG, W.; HOU, C.; GAO, X.; WANG, L.; WANG, S. Zinc oxide nanoparticles affect biomass accumulation and photosynthesis in arabidopsis. **Frontiers in Plant Science**, Lausanne, v. 6, p. 1243, 2016. doi: 10.3389/fpls.2015.01243.

YANO, J.; KERN, J.; IRRGANG, K.-D.; LATIMER, M. J.; BERGMANN, U.; GLATZEL, P.; PUSHKAR, Y.; BIESIADKA, J.; LOLL, B.; SAUER, K.; MESSINGER, J.; ZOUNI, A.; YACHANDRA, V. K. X-ray damage to the Mn4&Ca complex in single crystals of photosystem II: A case study for metalloprotein crystallography. **Proceedings of the National Academy of Sciences of the USA**, Washington, DC, v. 102, n. 34, p. 12047-12052, 2005.

ZENG, Y.; GRANDNER, S.; OLIVEIRA, C. L. P.; THÜNEMANN, A. F.; PARIS, O.; PEDERSEN, J. S.; KLAPP, S. H. L.; von KLITZING, R. Effect of particle size and Debye length on order parameters of colloidal silica suspensions under confinement. **Soft Matter**, Cambridge, v. 7, n. 22, p. 10899–10909, 2011.

ZHANG, R.; ZHANG, H.; TU, C.; HU, X.; LI, L.; LUO, Y.; CHRISTIE, P. Phytotoxicity of ZnO nanoparticles and the released Zn(II) ion to corn (Zea mays L.) and cucumber (Cucumis sativus L.) during germination. **Environmental Science and Pollution Research**, Berlin, v. 22, n. 14, p. 11109–11117, 2015.

ZUVERZA-MENA, N.; ARMENDARIZ, R.; PERALTA-VIDEA, J. R.; GARDEA-TORRESDEY, J. L. Effects of Silver Nanoparticles on Radish Sprouts: Root Growth Reduction and Modifications in the Nutritional Value. **Frontiers in Plant Science**, Lausanne, v. 7, p. 90, 2016. doi: 10.3389/fpls.2016.00090.

3 SYNCHRONTRON-BASED TECHNIQUE ASSOCIATED TO PLANT SCIENCE: A CASE OF Ag NANOPARTICLES IN COMMON BEAN GERMINATION

Abstract

The presence of nanoparticles (NP) in agricultural inputs is a clear fact, as can be seen in many patents involving this application. The nano form can improve the performance of these, but may cause risks to the environment since the fate of nanomaterials is poorly understood. Seed treatment is an extensive practice to provide micronutrients and disease protection. The treatment of the bean seed coat before sowing can be performed in a safer way compared to the common dispersion method in the field. This study investigates the effect of Ag_2S NP, Ag^0 NP and $AgNO_3$ (100, 1000 mg L^{-1} and 5000 mg L^{-1}) on the germination *Phaseolus vulgaris* seeds and the mechanism of interaction in the seed coat. Ag treatments did not affect the germination rate, but the development of the seedlings was significantly improved by Ag_2S NP while the $AgNO_3$ presented a negative effect compared to the control (water). The bean seed coat presents different layers, which are objects of this study. The treated seeds germinated for five days, seed coats were recovered and sectioned. Ag distribution and speciation were investigated in the bean testa by means of µ-XRF and µ-XANES, while the macromolecular composition was assessed by ATR-FTIR and micro-FTIR. The Ag biotransformation depended on the source. For the FTIR results it is possible to verify perturbations in carbohydrate region as well changes in the protein region. The combination of these results can contribute to building another step in the understanding of how nanoparticles can improve agricultural inputs and benefit food crops.

Keyword: X-ray absorption spectroscopy; X-ray fluorescence, synchrotron-based Fourier transform infrared, *Phaseolus vulgaris*

3.1 Introduction

Silver nanoparticles (Ag NP) are present in several materials for diverse applications. One of the most well-known utilizations is due to antimicrobial properties (PRABHU; POULOSE, 2012). Studies have highlighted the use in textiles (SPIELMAN-SUN et al., 2018), food conservation (CARBONE et al., 2016; KUMAR et al., 2018), cosmetics (KOKURA et al., 2010), drug delivery(TIAN et al., 2007; AUSTIN et al., 2014), and agricultural inputs (ANJUM et al., 2013; DESHPANDE, 2019). Previous investigations suggested that nanomaterials, including Ag NP can accumulate in the plants and induce toxic effects (WANG et al., 2017; CVJETKO et al., 2018; YAN; CHEN, 2019). Conversely, other studies show that plants can benefit from Ag NP, for instance it can enhance plant development (HOJJAT; HOJJAT, 2015; PALLAVI et al., 2016) and crop protection (KHOT et al., 2012; PARVEEN; RAO, 2015) once different silver-based nanoparticles present antifungal and bactericidal properties (ADISA et al., 2019). This property was explored against the Gibberella fujikuroi to rice seeds, Ag NP disinfected the seeds and improve the seedlings emergence (JO et al., 2015).

Seed priming is a strategy that aims at delivering nutrients or chemicals directly to seeds rather than broadcasting them in the field. This practice increases germination (VARIER et al., 2010) and productivity. One of the main advantages of this process is the reduced amount of employed chemicals compared to soil application. Since they are deposited on the seed, such chemicals can be assimilated by the seedling during the germination process or remain in the neighbouring soil and eventually being taken up by roots. Hence, since seed treatment is carried out in a warehouse, it also reduces the costs involved in application. Ag NP used in seed priming can positively affect aquaporin gene expression and in reactive oxygen species (ROS) production, improving the water uptake and consequently the germination (MAHAKHAM et al., 2017). Seed priming can be also a strategy to improve the crops in salinity soil (i. g. wheat) (MOHAMED et al., 2017).

Even though silver is not a nutrient, it can affect plant metabolism. Seeds of B. juncea (SHARMA et al., 2012) and rice (MAHAKHAM et al., 2017) treated with Ag NP yielded seedlings with improved root system and therefore healthier seedlings. On the other hand, seed treatment for tomatoes and radish, negatively affected root elongation (SONG et al., 2013; ZUVERZA-MENA et al., 2016). Silver primed rice seeds presented enhanced germination which was associated to increased α-amylase activity and up-regulation of aquaporin genes in germinating seeds (MAHAKHAM et al., 2017).

The germination rate, depending on the crop, is not significantly affected by Ag NP in general and one explanation can be the protective function of the seed coat. However, a previous work raised the possibility of nanoparticles to penetrate through the seed coat (MAHAKHAM et al., 2017). For corn, watermelon and zucchini, the germination rate was improved when seeds were treated with a range from 500 to 2500 mg L^{-1} of Ag NP (ALMUTAIRI; ALHARBI, 2019). The nanoparticles interaction with the seed coat is a subject not so explored.

We have previously shown that most of nutrient applied in soluble or nanoparticulate forms remains trapped in the seed coat and is latter absorbed by seedlings (DURAN et al., 2017; 2018; RODRIGUES et al., 2018; SAVASSA et al., 2018). However, the storage process within the seed coat and possible chemical transformations taking place in this tissue deserves deeper understanding.

Hence, this study investigated the behavior of silver nanoparticles in the seed coat of common bean (*Phaseolus vulgaris*) during the germination phase using synchrotron-based techniques, namely: microprobe X-ray fluorescence spectroscopy (μ-XRF), micro X-ray absorption near edge structure (μ-XANES), and Fourier transform infrared microscopy (μ-FTIR).

3.2 Materials and Methods

3.2.1 Characterization of Ag NPs

The metallic Ag nanoparticle (Ag^0 NP) (15 nm) dispersion was provided by TNS company, Brazil. Ag_2S nanoparticles (Ag_2S NP) (42 nm) were produced through the sulfidation of Ag NPs coated with polyvinylpyrrolidone (PVP) (NanoAmor, Nanostructured and Amorphous Materials Inc. (USA) according to (LEVARD et al., 2011) as stated in (PRADAS DEL REAL et al., 2017). The ionic control used was $AgNO_3$ (Nuclear, Brazil).

Aqueous dispersions at 1, 10 and 100 mg Ag L^{-1} were prepared in distilled water. Before application, the Ag_2S NP suspension was sonicated with a Fisher Scientific Model 750 Sonic Dismembrator probe operating at 60 W for three cycles of one minute each and 30 seconds interval between each cycle. These particles were previously characterized by (PRADAS DEL REAL et al., 2017).

For the Ag^0 NP the crystallite dimension (D) (Figure 1(a)) was determined using the Scherrer equation. The crystallite dimensions were corrected subtracting the instrumental broadening determined by measuring the 111 planes of Si monocrystal. X-ray diffraction (XRD) patterns were recorded using a Cu Kα radiation in a Philips PW 1877 diffractometer.

Scanning electron microscopy (SEM) images were acquired using a Magellan 400 microscope (FEI Company, USA). For these measurements, Ag^0 NP aqueous dispersions at 100 mg L^{-1} were dropped on a carbon tape adhered in a sample holder and dried at room temperature (Figure 1 b).

Figure 1. Ag^0 NP characterization. (a) XRD pattern and crystallite size. (b) SEM imagine and (c) DLS and Zeta potential

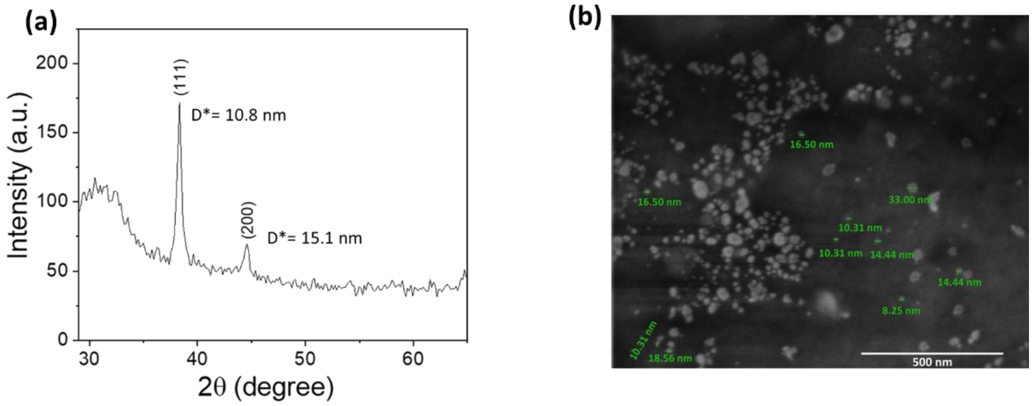

(c)

Dynamic Light Scattering	Zeta Potential
33.6 (± 0.7)	26.4 (± 0.4)

3.2.2 Germination assay

Bean seeds, variety IAC Sintonia (Agronomic Institute of Campinas, Brazil) (CHIORATO et al., 2018), were disinfected using 10% NaClO solution and rinsed in deionized water. After disinfection, the seeds were soaked for one hour in Ag^0 NP and Ag_2S NP dispersions and in the ionic control $AgNO_3$, all of them at 1, 10 and 100 mg L^{-1} (20 seeds per treatment). Deionized water was used as negative control. The seeds were transferred to Petri dishes with the bottom and top covered humid filter paper and finally incubated for germination during five days at 27 °C. The experiment was conducted with five replicates per treatment. After the period of germination, the seeds were counted, weighed and the radicle length of the seedlings was determined through the Seed Vigor Imaging System software (SVIS). The data (germination rate and radicle lenght) were submitted to statistical analysis. With the null hypothesis rejected in the analysis of variance (ANOVA), the Tukey's test at 95% confidence interval was applied using Minitab® 18.1.

3.2.3 Scanning electron microscopy (SEM)

Seeds from each treatment were used for SEM analysis. The hilum region was sampled with a scalpel blade and was immediately glued to carbon tape on aluminium stubs, gold coated (Bal-tec model SCD 050), and examined with a scanning electron microscope (Jeol - JSM IT 300, Japan) at 15 kV and digitally recorded at a working distance of 15 mm.

3.2.4 μ-XRF and μ-XANES

Microprobe X-ray fluorescence spectroscopy (μ-XRF) (Orbis PC, EDAX, USA) was used to perform line scans and access the spatial distribution of Ag in the hilum region of treated seeds. Seeds were sectioned as described elsewhere (RODRIGUES et al., 2018). A Rh anode X-ray working at 20 kV and 400 μA was used to generate the X-ray beam, and a poly-capillary optical element focused it down to 30 μm in diameter. The detection was carried out by a 30 mm^2 silicon drift detector with a resolution of 140 eV at Mn-Kα. Thirty-two points were scanned yielding a line. The dwell time was 30 s per point, the measurements were performed under vacuum, using an Al 25 μm filter and the dead time was around 9%. The Ag content was expressed in terms of Lα net count rate.

μ-XRF maps and μ-XANES were performed at the ID21 beam line at the European Synchrotron Radiation Facility (ESRF) in Grenoble, France (SALOMÉ et al., 2013). The beamline is equipped with a U42 undulator to generate the X-rays, a double-crystal fixed exit Kohzu monochromator with Si (111) crystals for energy selection, and Kirkpatrick-Baez fixed curvature focusing optics. μ-XRF maps were obtained with a beam size of 0.5 × 0.9 μm^2, incident energy of 3.42 keV and a flux of 7.9 x 10 9 photons s^{-1}. μ-XANES energy scans at Ag L_{III}-edge were done in the region from 3.34 keV to 3.42 keV with 0.5 eV constant steps and 0.1 ms dwell time per energy step. Samples obtained from the treated seed coats, approximately 0.2 x 0.2 cm^2, were embedded in OCT resin and cryofixed in liquid nitrogen (LN2) before cryo-sectioning. Cross-sections 20 μm thick were obtained using a motorized rotary microtome (Leica LN22, Germany) equipped with a binocular microscope and diamond blade. The samples were mounted between ultralene films in a cold copper sample holder and transfer to a cryo chamber to be analyzed.

3.2.5 Fourier Transform Infrared Analysis

Fourier Transform Infrared measurements were carried out in ID21 at the ESRF (SUSINI et al., 2007). The μ-FTIR end-station was equipped with a Thermo Nicolet Nexus infrared spectrometer (Thermo Scientific, Madison, WT, USA) and Thermo Nicolet Continuum infrared microscope (Thermo Scientific, Madison, WT, USA). Seed coat samples were prepared as 4 μm thick cross-sections using a cryomicrotome (Leica LN22, Germany). The sections were placed between two BaF_2 windows (0.4 mm thick) in a metallic sample holder, cooled down to LN2 temperature, and freeze-dried for 4 h under vacuum (2 x 10^{-4} mbar) and low temperature (-50˚C) followed by 4 h under vacuum and brought up to room temperature. Synchrotron FTIR microscopy was performed in transmission mode using a

10 × 10 μm² beam. Spectra (average of 128 scans) were recorded over a range of 3000 to 850 cm^{-1} with spectral resolution of 4 cm^{-1}. To analyze the external and internal surfaces of treated seed coats, circular samples (10 mm diameter) were punched from the treated seed coats. Then, they were snap frozen in LN2 and freeze-dried to be analyzed by attenuated total reflectance Fourier transform infrared (ATR-FTIR) using a bench top equipment Thermo Nicolet Nexus 4700 FT-IR Spectrometer.

Orange Data Mining software (DEMSAR et al., 2013) was used for statistical analysis, including the add-on for spectral data analysis (TOPLAK et al., 2017). Linear Discriminant Analysis (LDA) together with Principal Component Analysis (PCA) were used for clustering different treated samples. The feature extraction was done using Logistic Regression and Least Absolute Shrinkage as Selection Operator (LASSO). Using a K-fold cross validation method the model's robustness parameters AUC (Area Under Curve), receiver operating characteristic (ROC) curve, precision, and sensitivity (or recall) were monitored to ensure optimal performance of the model.

3.3. Results and Discussion

3.3.1 Germination assay

Germination assays were performed under a factorial design of three sources (Ag^0 NP, Ag_2S NP and $AgNO_3$) and three concentrations (1, 10, and 100 mg L^{-1}). Figure 2 show seedlings after five days of germination. The Ag_2S NP present the shorter hypocotyl and longer radicle compared with the other treatments and control. In this treatment the hypocotyl also show oscillation curves when compared to the others treatments (SPURNÝ, 1966). For Ag^0 NP treated seeds, the seed coat seems to come off more easily than in other treatments. Significant differences are present in Figure 3.

Figure 2. *Phaseolus vulgaris* seedlings after five days of germination. Seeds were treated with H_2O (control) and three different Ag sources: $AgNO_3$, Ag^0 NP and Ag_2S NP

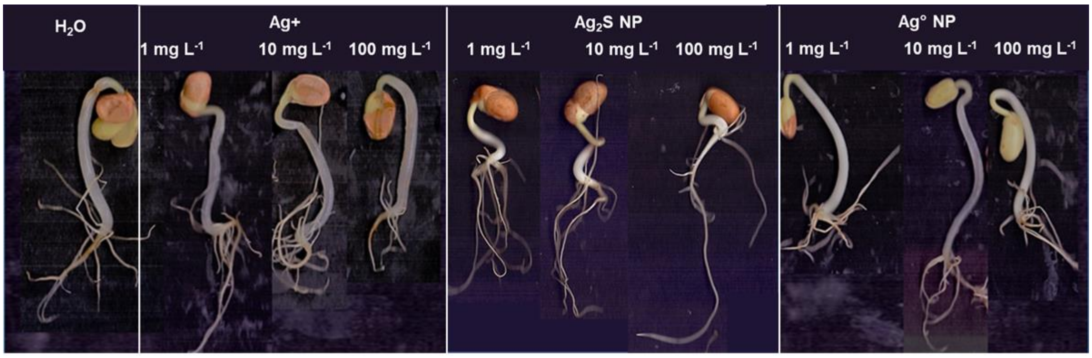

Figure 3a presents the effects of the treatments on radicle length after five days of germination. Overall positive impact on radicle length was observed for the seeds treated with Ag_2S NP (statistically significant at 1 mg L^{-1}), and negative impact was observed for $AgNO_3$ treated seeds (statistically significant at 10 mg L^{-1}). The Ag^0 NP treatments did not show any significant effect on radicle length. Figure 3(b) presents the germination rate after five days. Tukey's test was applied and no statistical difference was observed between treatments and control. Thus, even though the treatments did not affect the germination rate, it positively impacted seedling development.

The results described above are in line with Vannini et al. (2013) that showed that seeds of *Eruca sativa* (Arugula) treated with Ag-PVP NP (14 nm) at different concentrations (0, 0.1, 1, 10, 20, and 100 mg L^{-1}) presented no significant difference in the germination rate, while the root elongation was increased, and $AgNO_3$ up to 20 mg L^{-1} blocked the germination process (VANNINI et al., 2013). On the other hand, results reported by El-Temsah and Joner (2012) for flax, barley, and ryegrass at 10 mg L^{-1} Ag NP treatments showed reduced germination, but higher concentrations did not present concentration dependent effect (EL-TEMSAH; JONER, 2012). For corn, zucchini and watermelon, germination rate was improved in comparison with control (untreated plants) at all tested concentrations of AgNPs (0.05, 0.1, 0.5, 1, 1.5, 2 and 2.5 g L^{-1}) (ALMUTAIRI; ALHARBI, 2019).

Figure 3. Germination assay. (a) Radicle length (cm) and (b) germination rate (%) of common bean seeds on the fifth day of the germination assay following different treatments with Ag_2S NP, Ag^0 NP, $AgNO_3$ at 1, 10, and 100 mg L^{-1} and H_2O (control).a, b, c, d letters represent groups. Tukey test (P = 5%)

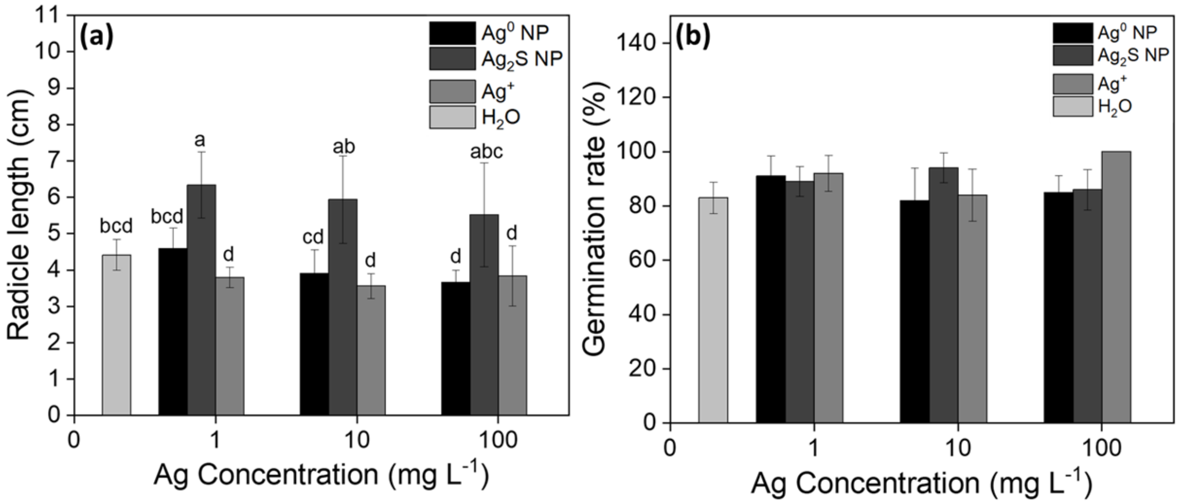

3.3.2 Spatial distribution of Ag in the hilum of *Phaseolus vulgaris* seeds

Due to the limit of detection imposed by the benchtop μ-XRF equioment (ca. 0.0292 cps mg kg^{-1} tissue), to determine the spatial distribution of Ag in the hilum the seeds were soaked in 1000 mg Ag L^{-1} treatments.

Figures 4 and 5 presents scanning electron-micrographs of seed surface after the treatments. It is clear that Ag_2S NP formed clusters around the hilum, micropyle, and lens. The same pattern is not verified to Ag^0 NP.

The nanoparticles are trapped in the seed coat, mostly in the hilum region. The hilum is a water entrance structure in the seed (AGBO et al., 1987; KIKUCHI et al., 2006) as well as micropyle and lens. Thereby, the NPs are carrying more easily to these parts compared with the rest of the cuticle in seed coat extension.

Figure 4. Scanning electron-micrographs of *Phaseolus vulgaris* seed surface after different treatments with silver sources. (a)-(d) Control Plants; (e)-(h) silver nitrate; (i)-(l) metallic silver nanoparticles; (m)-(p) silver sulfide nanoparticles. Arrows show Ag deposit around the hilum (n); micropyle (o) and lens (p). Note that in Ag0 the particles are not visible. HI – Hilum; MI- Micropyle, RA – Rafe, LE - Lens

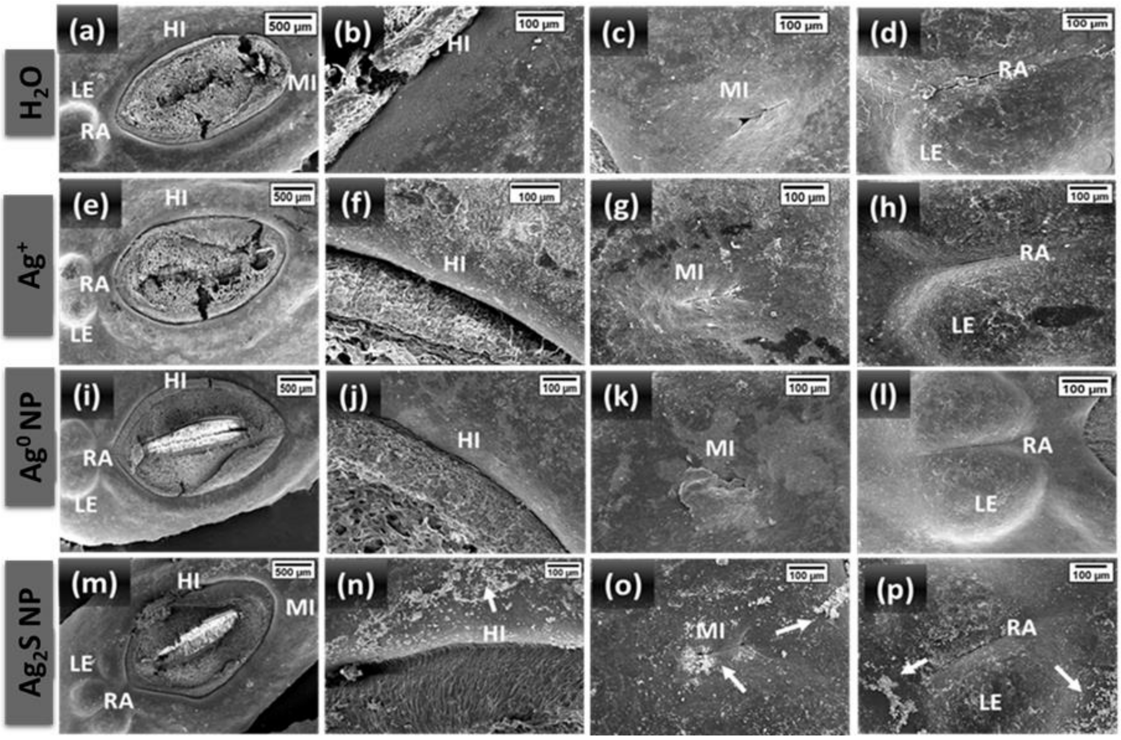

Figure 5. Scanning electron microscope with energy dispersive X-ray spectroscopy (SEM-EDS) microanalysis for samples treated with (a) H_2O (control), (b) Ag^0 NP, (c) Ag_2S NP and (d) $AgNO_3$

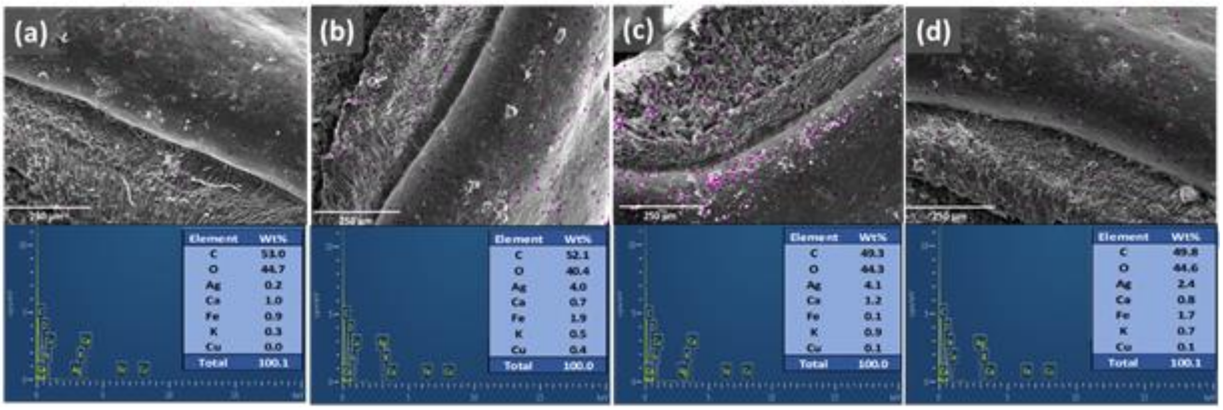

Figure 6(a) illustrates the scanned region (red line) and Figure 6(b) shows the Ag intensity along the hilum. Figures 7, 8 and 9 present additional scans at distinct regions. All Figures present points of analysis of the Ag net intensity and the respective limit of quantification (LOQ) for Ag.

The ILOQ was determined using the following equation:

$$ILOQ = 10\,x\,\sqrt{\frac{BG}{t}}$$

ILOQ: Instrumental Limit of Quantification

BG: background measurement

t: Time of spectra acquisition (s)

Figure 6. (a) Representation of the analyzed region. (b) Ag line scans of hilum in common bean (*Phaseolus vulgaris*) sections exposed to Ag_2S NP, Ag0 NP and $AgNO_3$ at 1000 mg L-1. The path of the points of analysis was from outside to inside the seed, passed through the endosperm and tegument. E – endosperm, T – tegument, checkered region the hilum

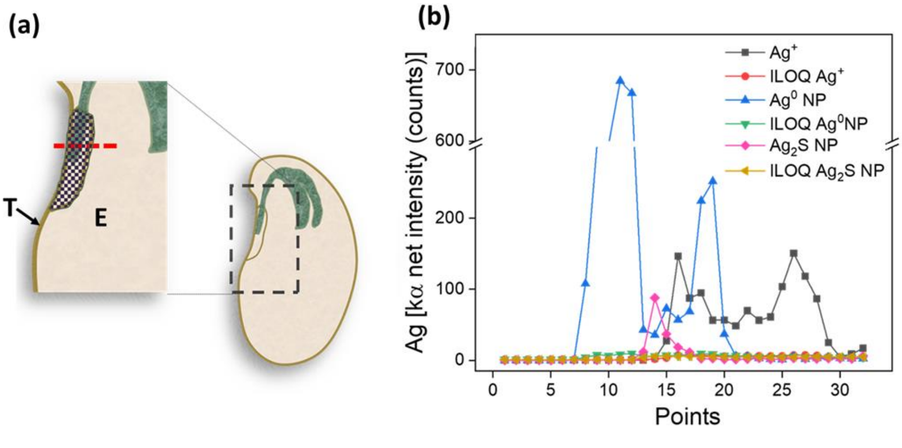

Figure 7. Picture (a) and Ag line scans of hilum in common bean (*Phaseolus vulgaris*) sections exposed to Ag_2S NP. Points acquired from (b) X line region, (c) Y line region and (d) Z line region. Black points are the Ag net intensity and red points the limit of quantification (LOQ) for Ag. 1 and 32 indicate the start direction of acquisition of the points of each analyzed region

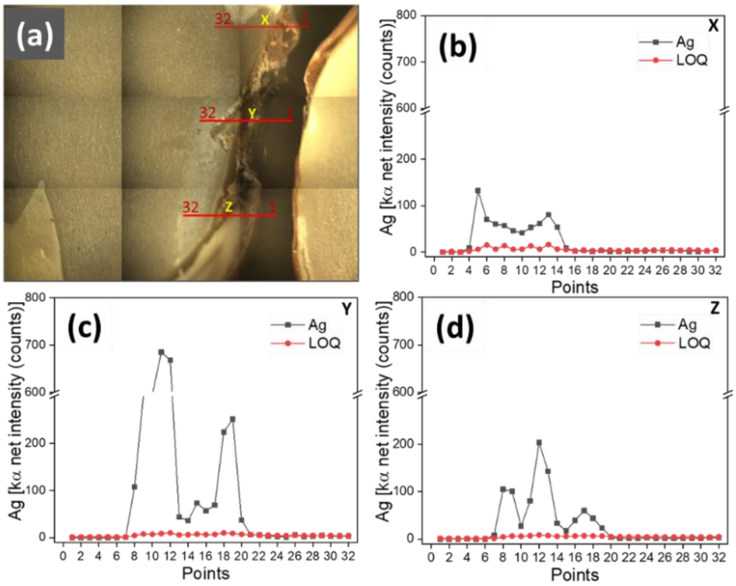

Figure 8. Picture (a) and Ag line scans of hilum in common bean (*Phaseolus vulgaris*) sections exposed to Ag^0 NP. Points acquired from (b) X line region, (c) Y line region and (d) Z line region. Black points are the Ag net intensity and red points the limit of quantification (LOQ) for Ag. 1 and 32 indicate the start direction of acquisition of the points of each analyzed region

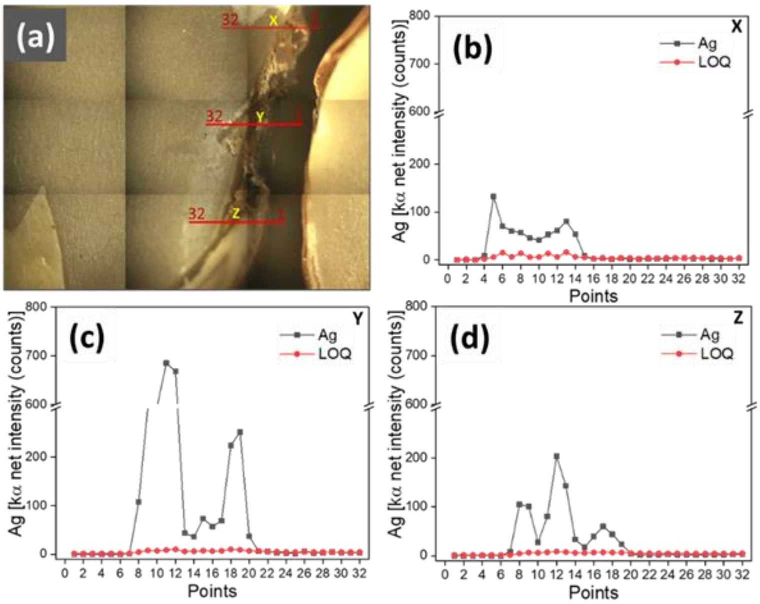

Figure 9. Picture (a) and Ag line scans of hilum in common bean (*Phaseolus vulgaris*) sections exposed to $AgNO_3$. Points aquired from (b) X line region, (c) Y line region and (d) Z line region. Black points are the Ag net intensity and red points the limit of quantification (LOQ) for Ag. 1 and 32 indicate the start direction of acquisition of the points of each analyzed region

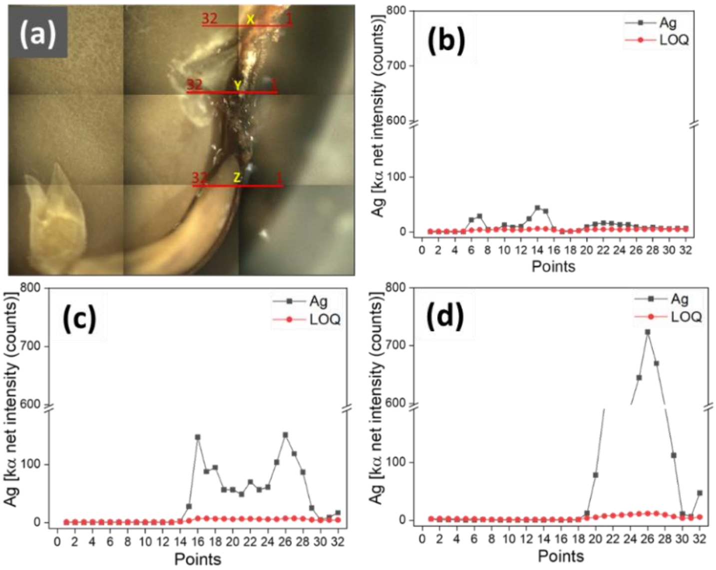

According to Figures 6 and 7, 8 and 9, Ag is concentrated in the hilum region, a layer of palisade cells connected externally by remaining subcuticular tissue, a “spongy like” one of the entries for water to seed (AGBO et al., 1987; ALVES JUNIOR et al., 2016). This is in agreement with previous studies that showed that Cu, Zn, and Fe ions and nanoparticles remained within the seed coat of common bean seed coat (DURAN et al., 2017; 2018; SAVASSA et al., 2018).

The results showed that Ag_2S NP did not penetrate as much as Ag^0 NP and $AgNO_3$ since the net intensity values are half or less than found in Ag^0 NP and $AgNO_3$ treatments. The uptake through the hilum can depend on NPs dispersion in water. The nominal size of Ag_2S NPs (42 nm, Zeta potential - 17mV) is bigger compared to Ag^0 NP (15 nm, Zeta potential + 26.4 mV) and due to its negative charge would tend to aggregate (as seen Figures 4 and 5) resulting in lower uptake through the hilum. Regarding the accumulation on the seed coat, it would be an effective barrier against NPs, only ions and small enough NPs would diffuse through the seed coat. Given the tendency to aggregate of Ag_2SNPs, the probability of finding an Ag_2S NP aggregate in the hilum is lower than for the other Ag treatments. This can explain the lower Ag intensity found for Ag_2S NPs treatment outside the hilum in the XRF line scans.

3.3.3 Ag localization and speciation in the seed coat

Considering that most of the nanoparticles are agglomerated in the bean seed coat, it is important to investigate the chemical speciation of Ag in this region.

Figure 10 a shows that despite its short thickness, the seed coat consists of several stacked tissue layers. It is possible to identify the cuticle, macrosclereids, osteosclereids and parenchyma layers. Therefore, one can hypothesize that chemicals might interact with these tissues distinctly.

From µ-XRF maps, it is possible to determine the localization of Ag in the different tissue layers of the seed coat. Silver in ionic treated seeds (Figure 10 b) is mainly located at the external layer (epidermis and macrosclereids). Conversely, Ag^0 NP treated sample (Figure 10 c) present Ag along the internal layer (parenchyma layers). In agreement with µ-XRF linescans (Figure 6), the intensity (comparable with concentration) of silver in the treatment with Ag_2S NP is lower compared with the other treatments.

µ-XANES allowed investigating Ag chemical speciation in the seed coat of treated samples. Figure 10 e shows Ag from ionic treatment was forming AgCl at the surface layer and is bound to O in the parenchyma layer. These two species are thermodynamically favoured, AgCl more than Ag_2CO_3 (LEVARD et al., 2012). Once have an abundance of ions in this treatment the formation of these molecules is favored. It is necessary to take into account that the disinfection of the seed before soaking was done with sodium hypochlorite, so there may be traces of Cl ions on the surface.

For Ag^0 NP (Figure 10 f) treatment, the spectra suggest that NP are suffering oxidative dissolution and forming thiolate complexes in the parenchyma layer, this result was expected, since Ag-thiol-containing organic ligand (Ag-cysteine) has a high stability constant (LEVARD et al., 2012), so ease of formation considering that the analyzed point is closer to the richer tissue (in contact with the embryo) of the sample. For Ag^0 NP the oscillation at 3380 eV, characteristic of metallic Ag can be related to dissolution and reprecipitation inside bean (theory is possible but less likely since with $AgNO_3$ treatment we do not see this behaviour) or Ag^0 NP enter through seed coat pores or scarifications. In Figure 10 (g), Ag_2S NPs are not suffering significant chemical modifications both in the surface and parenchyma layers.

Figure 10. Cross sections of *Phaseolus vulgaris* seed coat. (a) light microscopy after toluidine blue staining method. b-d μ-XRF maps showing Ag (red), P(green) and S (blue) distributions of seed sections exposed to: (b) $AgNO_3$ 100 mg Ag L^{-1}, (c) Ag^0 NP 100 mg Ag L^{-1} and (d) Ag_2S NP 100 mg Ag L^{-1} NP. (e) – (f) Ag-L edge XANES spectra recorded in different regions of the cross sections and standards (Ag_2CO_3, AgCl, Ag-Glutathione, Ag-foil, Acanthite): (e) sample treated with $AgNO_3$ 100 mg Ag L^{-1} , (f) Ag^0 NP 100 mg Ag L^{-1} and (g) Ag_2S NP 100 mg Ag L^{-1} NP. Number from 1 to 5 indicate the regions analyzed. C – cuticle, EP - epidermis, MS – macrosclereids, OS – osteosclereids, PA – parenchyma layers

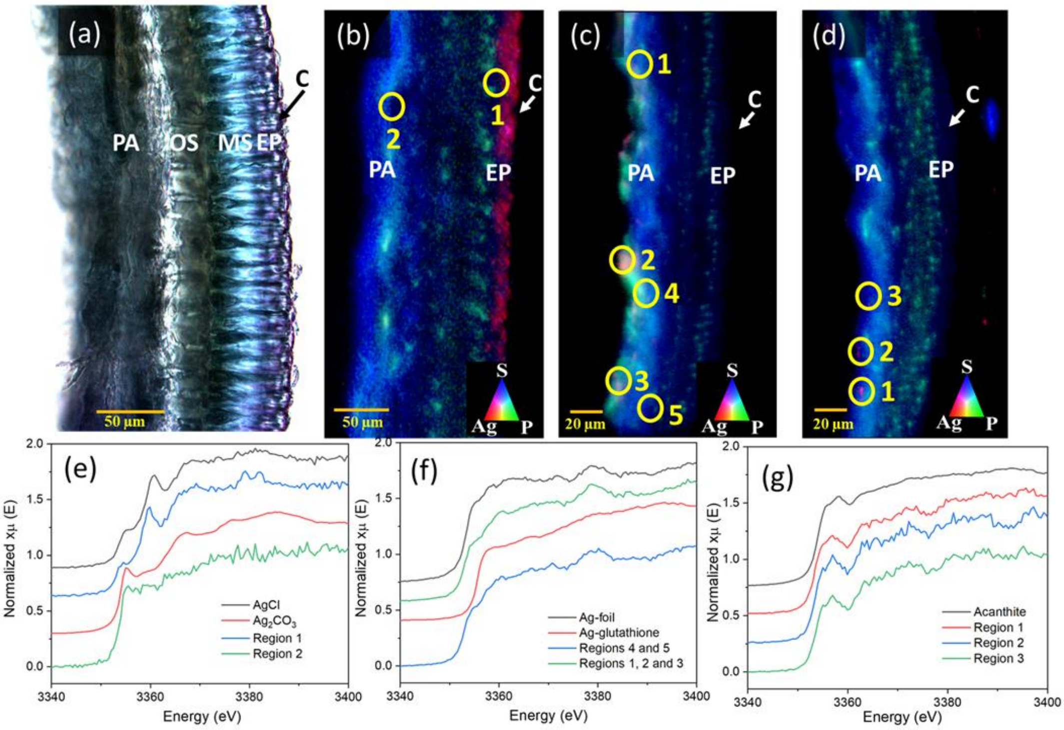

Figure 11 shows linear combination fits for some of spots. Due to the challenging conditions faced in the present study, i.e. low Ag concentration and high lateral resolution, it was not possible to obtain adequate spectra for all treatments and spots. In any case, the linear combination fits confirm the transformations occurred by the treatments with $AgNO_3$ and Ag^0 NP and also shows that there was no change with the silver binder in the treatment with Ag_2S NP, comparison done in Figure 10.

Figure 11. Linear combination fit for Ag-L edge XAS spectra recorded (a) regions 1, 2 and 3 from seeds treated with Ag^0 NP (R-factor: 0.0055732, pattern weights: Ag-foil - 0.640, Ag-glutathione 0.360), (b) regions 4 and 5 from seeds treated with Ag^0 NP (R-factor: 0.0053021, pattern weights: Ag-foil - 0.606, Ag-glutathione 0.394), (c) region 1 from seeds treated with $AgNO_3$ (R-factor: 0.0089423, pattern weights: AgCl - 0.882, Ag_2CO_3 0.118) and (d) region 1 from seeds treated with Ag_2S NP (R-factor: 0.0187312, pattern weights: Acanthite - 1.000)

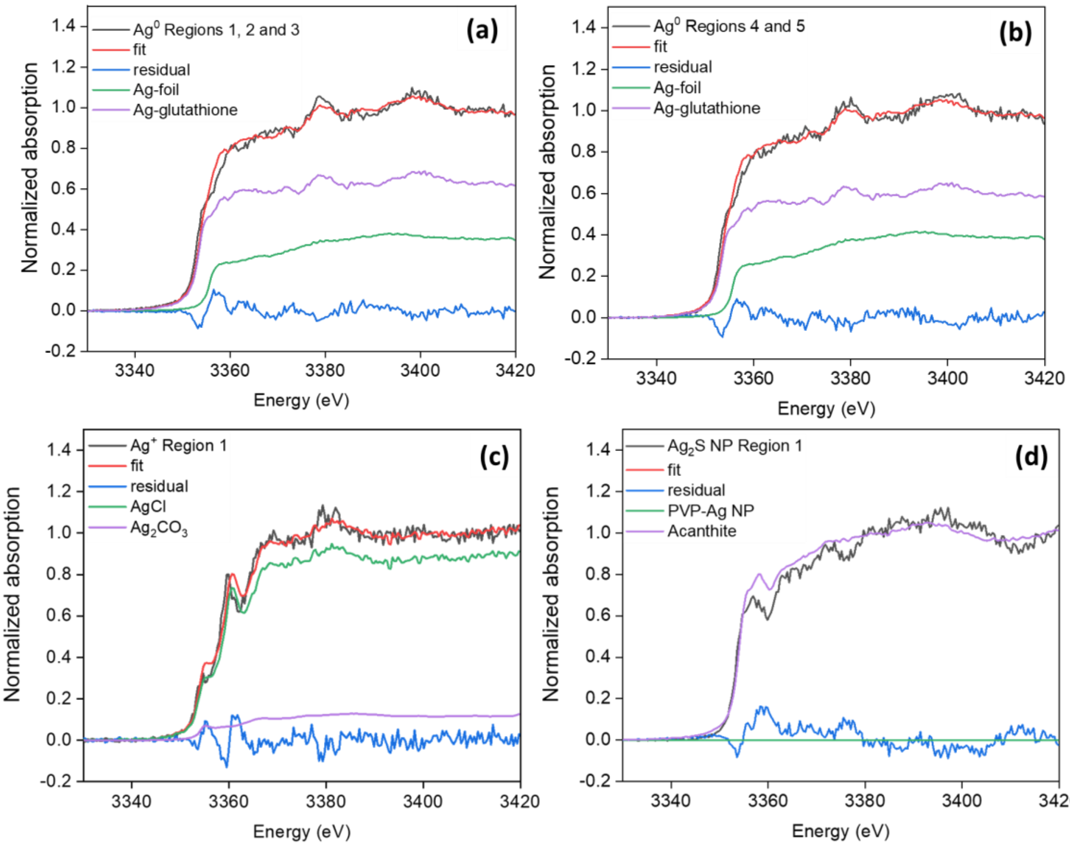

3.3.4 Fourier Transform Infrared Analysis

Vibration spectroscopy herein employed allowed probing the samples from the organic tissue standpoint. ATR-FTIR for outer surface (cuticle) and inner tegument surface (in contact with the embryo), provides information about possible changes in the main regions of the mid-IR spectrum i.e. carbohydrates (800 - 1300 cm^{-1}), proteins (1400 – 1700 cm^{-1}) and lipids (2800 – 3000 cm^{-1}).

Intending to reduce the large acquired data set, and highlight the most important and significant differences, the data was subjected to principal component analysis (PCA) and linear discriminant analysis (LDA).

There are intrinsic differences in organic composition between external and internal seed coat tissues (SMÝKAL et al., 2014; SHTEIN et al., 2018). Therefore, the data analysis was conducted separately for these two data sets. The PC-LDA (Figure 12) allowed grouping the treatments for both the internal part (Figure 12 a) and the external part (Figure 12 b).

Figure 12. PC-LDA plots from ATR analysis for different Ag treatments in (a) inner seed coat surface (parenchyma tissue) and (b) outer seed coat surface (cuticle tissue). Different colours correspond to different groups

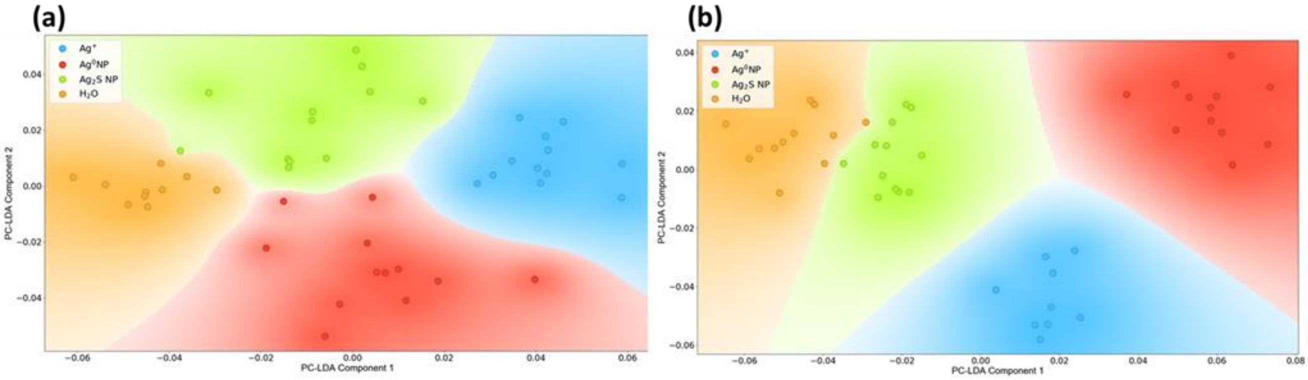

The results highlight the differences between the treatments, so much that they are grouped in different clusters as it is possible to see in Figure 12. At the inner tegument surface (Figure 12 a) the Ag ionic treated samples are grouped in the most opposite side of the control and even the Ag_2S NP treatment that does not appear with intensity in the internal part in the Figure 12 (b) appears grouped differing to control treatment as well as Ag^0 NP.

In the outer tegument surface the cluster in the most opposite side is the $AgNO_3$ treated samples, result in agreement with Figure 10 b that present more silver in epidermis. Again, all the treatments are grouped, presenting differences in comparison to the control.

The next step consists in extracting features from this large FTIR data set. A consistent statistical regression model, based principally in Logistic Regression and LASSO (Least Absolute Shrinkage and Selection Operator) was used to unfold it (TIBSHIRANI, 1996; MUTHUKRISHNAN; ROHINI, 2016).

Figure 13 present mean spectra from internal layer (parenchyma layers) with weighted LASSO logistic regression coefficients. Two-fold cross validation parameters for this model are AUC = 0.997, Precision = 0.963, and Recall = 0.957 (which are averages over treatments). These values are considered optimal according to (GAUTAM et al., 2015).

Figure 13. Mean spectra from the inner tegument surface (parenchyma layers) of common bean seed coat treated samples with weighted Lasso logistic regression coefficients. Differences in all spectra: in carbohydrate region (800 - 1300 cm^{-1}), proteins (1400 – 1700 cm^{-1}) and lipids (2800 – 3000 cm^{-1})

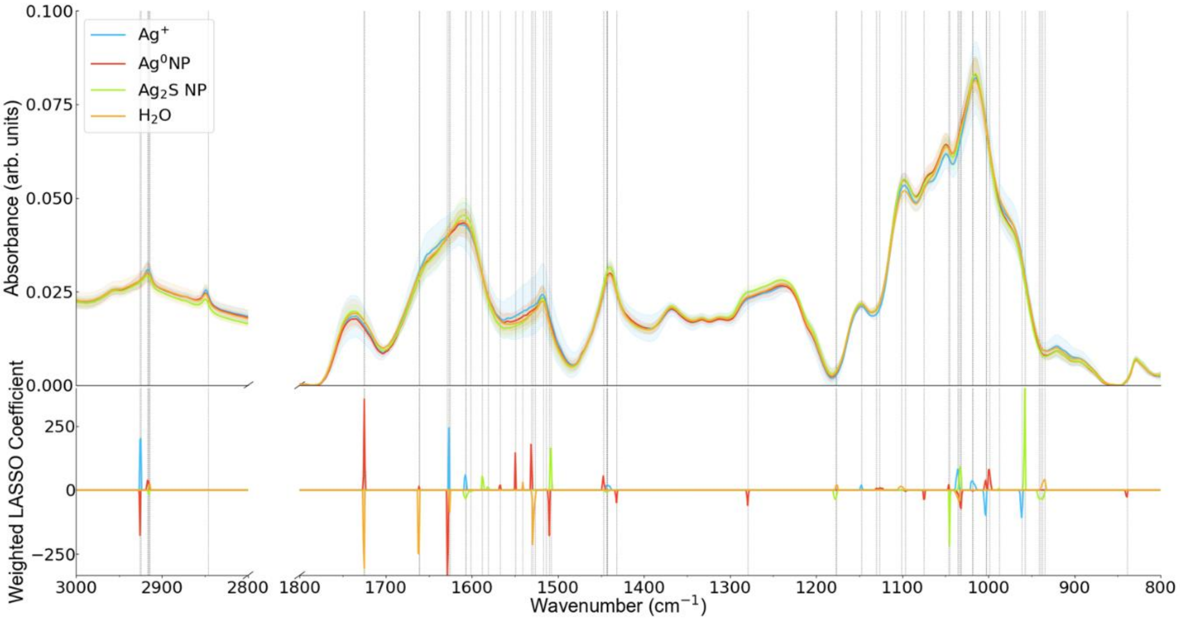

The chemical assignment, based on the literature, was performed examining each of the peaks obtained by LASSO. The main assignments are shown in Table 1.

In the carbohydrate region it is possible to observe differences associated with polysaccharides in general: 935-998 cm^{-1}, 1032 cm^{-1} and 1177 cm^{-1} (cellulose), 1074 cm^{-1} and 1148 cm^{-1} (amylopectin and amylose). These disturbing can be associated with modifications in the content of carbohydrate provided by the Ag NP treatment like showed by Salama (2012) for *Phaseolus vulgaris L*. and *Zea mays* L. (SALAMA, 2012).

In the protein region, one can observe peaks corresponding to the cell wall polysaccharide (1430 cm^{-1}, 1441-1447 cm^{-1}), amide II bands of proteins (1531 cm^{-1}, 1540-1549 cm^{-1}, and 1567-1587 cm^{-1}). The lipid region showed fewer differences, mainly in the 2924-2925 cm^{-1} region. Salama (2012) shows further that protein contains can be altered (in this case increased) by the Ag NP treatment in *Phaseolus vulgaris L*. and *Zea mays* L. (SALAMA, 2012)

Table 1. The FTIR spectral bands assignment selected by LASSO method for inner tegument surface seed coat samples

Wavenumber range (cm^{-1})	**Attributions**	**Main Compounds**	**Ref.**
838	C–O–C (α-glycosidic bond)	Carbohydrate molecule	(BUTA et al., 2015)
935 – 998	ν(CO)	C-O-C linkages	(KAČURÁKOVÁ; MATHLOUTHI, 1996)
1018	ν(CO), ν(CC), δ(OCH)	polysaccharides, pectin	(TALARI et al., 2017)
1032	ν(C–O), ν(C–C)	Cellulose	(MONNIER et al., 2017)
1035	ν(OH), ν(C–OH)	Cell wall polysaccharides (arabinan)	(ZHU; TAN, 2016)
1044	ν(C-O), ν(C-C), ν(C=C), ν(COC)	Pectin, various polysaccharides, also suberin or cutin	(REGVAR et al., 2013)
1046	ν(C-O)	L-(+)-arabinose	(KAČURÁKOVÁ; MATHLOUTHI, 1996)
1074	β(COH)	Amylopectin and amylose	(KAČURÁKOVÁ; MATHLOUTHI, 1996)
1126	ν(C–O)	disaccharides	(TALARI et al., 2017)
1130	ν(C-O)	L-(+)-arabinose	(KAČURÁKOVÁ; MATHLOUTHI, 1996)
1148	ν(COC), ν(CC)	Amylopectin and amylose	(KAČURÁKOVÁ; MATHLOUTHI, 1996)
1177	ν(C-O)	Ester bonds O=C-O of cellulose	(ZEIER; SCHREIBER, 1999)
1279	τ(CH2)	D-(−)-ribose	(WIERCIGROCH et al., 2017)
1430	δ(O–H)	cell wall polysaccharide, alcohol, and carboxylic acid	(TÜRKER-KAYA; HUCK, 2017)
1441-1447	δ_{as}(C–H) of CH_2 and CH_3	cell wall polysaccharide, alcohol, and carboxylic acid	(TÜRKER-KAYA; HUCK, 2017)
1507-1509	ν(C=C) aromatic	lignin	(TÜRKER-KAYA; HUCK, 2017)
1513	C=C–C	approximation of aromatic ring bonding	(BUTA et al., 2015)
1531	δ(NH); ν(CN)	amide II bands of proteins	(KONG; YU, 2007)
1540-1549	ν(C=N); ν(N–H)	Amide II	(TÜRKER-KAYA; HUCK, 2017)
1567-1587	δ(NH); ν(CN)	amide II bands of proteins	(KONG; YU, 2007)
1607	ν(C=O) aromatic	lignin, alkaloid	(TÜRKER-KAYA; HUCK, 2017)
1626-1628	C=C stretch	phenolic compound	(TÜRKER-KAYA; HUCK, 2017)
1661	ν(C=O)	amide I-proteins	(BUTA et al., 2015)
1725	ν(C=O), ν(COO^-)	Fatty acids and various polysaccharides	(REGVAR et al., 2013)
2846	ν(CH_2)	mainly lipids with a little contribution from protein, carbohydrate, and nucleic acid	(WIERCIGROCH et al., 2017)
2914-2916	ν(CH)	Carbohydrate molecule	(WIERCIGROCH et al., 2017)
2924-2925	ν_{as}(CH_2)	mainly lipid with a little contribution from protein, carbohydrate, and nucleic acid	(TÜRKER-KAYA; HUCK, 2017)

Key: ν - stretching, as – asymmetric, s - symmetric, β – in-plane bending, δ - scissoring, ω - wagging, τ - twisting, def – deformation.

The spectra from outer tegument surface, in Figure 14, presented fewer differences compared to the inner tegument surface (Figure 13). Still, the two-fold cross validation parameters present optimal values: AUC = 1.000, Precision = 1.000 and Recall = 1.000 (which are the averages over treatments).

In this case, the main differences are in carbohydrate region (800 - 1300 cm^{-1}), followed by proteins region (1400 – 1700 cm^{-1}) and, finally, in the lipid region (2800 – 3000 cm^{-1}).

Figure 14. Mean spectra from outer tegument surface (cuticle) of common bean seed coat treated samples with weighted Lasso regression coefficients. Differences in all spectra and in carbohydrate region (800 - 1300 cm^{-1}), (c) proteins (1400 – 1700 cm^{-1}) and (d) lipids (2800 – 3000 cm^{-1})

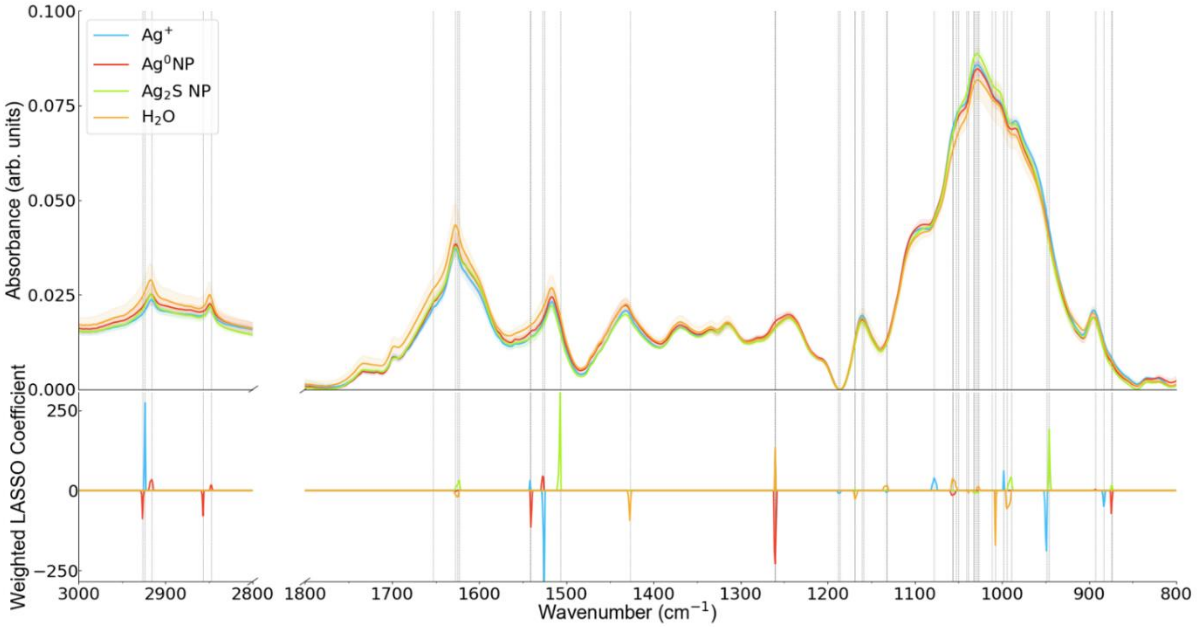

The main assignments are shown in Table 2. The carbohydrate region presents differences associated to general polysaccharides: 874 cm^{-1}, 989 cm^{-1} and 1259 cm^{-1} (cellulose), 1077 cm^{-1} (amylopectin and amylose). The protein region shows differences in peaks corresponding to the lignin (1507 cm^{-1}), amide II (1540 - 1541 cm^{-1}) and phenolic compound (1622-1623 cm^{-1}). Finally, the lipid region presented the least differences, mainly at 2847-2856 cm^{-1} and 2923-2926 cm^{-1}.

Table 2. The FTIR spectral bands assignment selected by LASSO method for outer tegument surface seed coat samples

Wavenumber range (cm-1)	**Attributions**	**Main Compounds**	**Ref.**
873-874	ν(C–O)	β–d-fructose	(TÜRKER-KAYA; HUCK, 2017)
892	ν(CC), β(CCH)	carbohydrate molecule	(WIERCIGROCH et al., 2017)
948	combination of ν(CO)ring, ν(CC) and β(CCH)	D-(-)-ribose	(WIERCIGROCH et al., 2017)
989	δ(CO)	Cellulose	(MARÉCHAL; CHANZY, 2000)
993	C–O stretch	Cutin	(TÜRKER-KAYA; HUCK, 2017)
998	ν(CO)	α-(1–6) glycosidic bond	(KAČURÁKOVÁ; MATHLOUTHI, 1996)
1011	ν(CO), ν(CC), β(COH)	carbohydrate molecule	(WIERCIGROCH et al., 2017)
1026	ν(CO), ν(CC)	D-(-)-ribose	(WIERCIGROCH et al., 2017)
1029	O–CH3 stretching	methoxy groups	(TALARI et al., 2017)
1032	ν(C–O), ν(C–C)	Cellulose	(MONNIER et al., 2017)
1050-1052	C–O–C stretch; C–OH stretch; C–OH deformation; C–O–C deformation	carbohydrate molecule	(BUTA et al., 2015)
1055	ν(C–O–C); ν(C–OH); def(C–OH); def(C–O–C)	pyranose, and furanose ring (carbohydrate molecule)	(BUTA et al., 2015)
1077	β(COH)	Amylopectin and amylose	(KAČURÁKOVÁ; MATHLOUTHI, 1996)
1132	ν(CO)	L-(+)-arabinose	(WIERCIGROCH et al., 2017)
1160-1168	νas (C–O–C)	Cutin	(TÜRKER-KAYA; HUCK, 2017)
1260	ν(C-C), ν(C-O), ν(C=O), ν(C-N), δ(N-H), νas(PO2), ν(P=O)	Lignin, proteins (amide III), and various polysaccharides	(REGVAR et al., 2013)
1427	δ(O–H)	Cell wall polysaccharide, alcohol, and carboxylic acid	(TÜRKER-KAYA; HUCK, 2017)
1507	ν(C=C) aromatic	Lignin	(TÜRKER-KAYA; HUCK, 2017)
1527	Stretching C = N, C = C	Amide groups	(TALARI et al., 2017)
1540-1541	ν(C=N); ν(N–H)	Amide II	(TÜRKER-KAYA; HUCK, 2017)
1627	ν(C=C)	Phenolic compound	(WIERCIGROCH et al., 2017)
1622-1623	ν(C=C)	Phenolic compound	(TÜRKER-KAYA; HUCK, 2017)
2847-2856	$\nu_s(CH_2)$	Mainly lipids with a little contribution from protein, carbohydrate, and nucleic acid	(TÜRKER-KAYA; HUCK, 2017)
2915	ν(CH)	carbohydrate	(WIERCIGROCH et al., 2017)
2923-2926	$\nu_{as}(CH_2)$	Mainly lipid with a little contribution from protein, carbohydrate, and nucleic acid	(TÜRKER-KAYA; HUCK, 2017)

Key: ν - stretching, as – asymmetric, s - symmetric, β – in-plane bending, δ - scissoring, ω - wagging, τ - twisting, def – deformation.

3.4 Conclusion

The Ag applied to the common bean seeds did not affect the germination rate, but the development of the seedlings was statistically improved by Ag_2S NP, while the $AgNO_3$ presented a negative effect compared to the control (water).

Most part of Ag, regardless of the source, remained associated to the seed coat. However, the highest penetration was observed for Ag^0 NP and the lowest for Ag_2S NP. Possibly why Ag^0 NP enter into the seed coat as entire nanoparticle, and/or due its high reactivity with organic molecules like thiol groups while the Ag_2S NP is not so toxic as Ag_2S NP, once less Ag ions are released and consequently less interaction occours (LEVARD et al., 2012).

It was possible to observe that, depending on the source of Ag, it was accumulated and biotransformed in different tissues of the seed coat. Ag from ionic treatment was found as AgCl at the surface layer and bound to O in the parenchyma layer, while Ag_2S NPs did not show any detectable chemical changes both in the surface and parenchyma layers.

For the FTIR results it was possible to verify perturbations in carbohydrate region associated with polysaccharides in general: 935-998 cm^{-1}, 1032 cm^{-1} and 1177 cm^{-1}, 1074 cm^{-1} and 1148 cm^{-1}. These facts can be associated with modifications in the content of carbohydrate induced by the Ag NPs treatment as well as the changes observed in the protein region of the FTIR spectra, 1507 cm^{-1}, 1540-1541 cm^{-1} and 1622-1623 cm^{-1}. Since carbohydrates and proteins are involved in seed protection mechanisms like: water movement, protecting the embryo against injuries (MELLO et al., 2010; ZANOTTI et al., 2012), it is possible to conclude that besides disturb the nutrient profile of the seeds, the Ag treatments may affect the seed protection.

References

ADISA, I. O.; PULLAGURALA, V. L. R.; PERALTA-VIDEA, J. R.; DIMKPA, C. O.; ELMER, W. H.; GARDEA-TORRESDEY, J. L.; WHITE, J. C. Recent advances in nano-enabled fertilizers and pesticides: a critical review of mechanisms of action. **Environmental Science: Nano**, London, v. 6, p. 2002-2030, 2019.

AGBO, G. N.; HOSFIELD, G. L.; UEBERSAX, M. A.; KLOMPARENS, K. Seed microstructure and its relationship to water uptake in isogenic lines and a cultivar of dry beans (Phaseolus vulgaris L.). **Food Structure**, Chicago, v. 6, n. 1, p. 91–102, 1987.

ALMUTAIRI, Z.; ALHARBI, A. Effect of silver nanoparticles on seed germination of crop plants. **Journal of Advances in Agriculture**, Punjab, v. 4, n. 1, p. 280–285, 2019.

ALVES JUNIOR, C.; OLIVEIRA VITORIANO, J. de; SILVA, D. L. S. da; LIMA FARIAS, M. de; LIMA DANTAS, N. B. de. Water uptake mechanism and germination of Erythrina velutina seeds treated with atmospheric plasma. **Scientific Reports**, London, v. 6, p. 33722, 2016.

ANJUM, N. A.; GILL, S. S.; DUARTE, A. C.; PEREIRA, E.; AHMAD, I. Silver nanoparticles in soil plant systems. **Journal of Nanoparticle Research**, London, v. 15, n. 9, p. 1896, 2013.

AUSTIN, L. A.; MACKEY, M. A.; DREADEN, E. C.; EL-SAYED, M. A. The optical, photothermal, and facile surface chemical properties of gold and silver nanoparticles in biodiagnostics, therapy, and drug delivery. **Archives of Toxicology**, Berlin, v. 88, n. 7, p. 1391–1417, 2014.

BUTA, E.; CANTOR, M.; ŞTEFAN, R.; POP, R.; MITRE JUNIOR, I.; BUTA, M.; SESTRAŞ, R. E. FT-IR Characterization of pollen biochemistry, viability and germination capacity in Saintpaulia H . Wendl. Genotypes. **Journal of Spectroscopy**, New York, v. 2015, art. ID 706370, 2015. doi: 10.1155/2015/7063702015.

CARBONE, M.; DONIA, D. T.; SABBATELLA, G.; ANTIOCHIA, R. Silver nanoparticles in polymeric matrices for fresh food packaging. **Journal of King Saud University - Science**, Riyadh, v. 28, n. 4, p. 273–279, 2016.

CHIORATO, A. F.; CARBONELL, S. A. M.; GONÇALVES, J. G. R.; SILVA, D. A. da; Benchimol-Reis, L. L.; CARVALHO, C. R. L.; BARROS, V. L. N. P. de; FREITAS, R. S. de; TICELLI, M.; GALLO, P. B.; SANTOS, N. C. B. dos. IAC Sintonia: new carioca common bean cultivar. **Crop Breeding and Applied Biotechnology**, Stockholm, v. 18, p. 338-342, 2018.

CVJETKO, P.; ZOVKO, M.; ŠTEFANIĆ, P. P.; BIBA, R.; TKALEC, M.; DOMIJAN, A. M.; VRČEK, I. V.; LETOFSKY-PAPST, I.; ŠIKIĆ, S.; BALEN, B. Phytotoxic effects of silver nanoparticles in tobacco plants. **Environmental Science and Pollution Research**, Berlin, v. 25, n. 6, p. 5590–5602, 2018.

DEMŠAR, J.; CURK, T.; ERJAVEC, A; GORUP, Č.; HOČEVAR, T.; MILUTINOVIČ, M.; MOŽINA, M.; POLAJNAR, M.; TOPLAK, M.; STARIČ, A.; ŠTAJDOHAR, M.; UMEK, L.; ŽAGAR, L.; ŽBONTAR, J.; ŽITNIK, M.; ZUPAN, B. Orange: data mining toolbox in python. **Journal of Machine Learning Research**, Cambridge, v. 14, p. 2349–2353, 2013.

DESHPANDE, M. V. Nanobiopesticide perspectives for protection and nutrition of plants. In: KOUL, O. (Ed.). **Nano-biopesticides today and future perspectives**. San Diego: Academic Press, 2019. chap. 3, p.47–68. doi: 10.1016/B978-0-12-815829-6.09993-9.

DURAN, N. M.; MEDINA-LLAMAS, M.; CASSANJI, J. G. B.; LIMA, R. G. de; ALMEIDA, E. de; MACEDO, W. R.; MATTIA, D.; CARVALHO, H. W. P. de. Bean seedling growth enhancement using magnetite nanoparticles. **Journal of Agricultural and Food Chemistry**,Washington, DC, v. 66, n. 23, p. 5746–5755, 2018.

DURAN, N. M.; SAVASSA, S. M.; LIMA, R. G. D.; ALMEIDA, E. de; LINHARES, F. S.; VAN GESTEL, C. A. M.; CARVALHO, H. W. P. de. X-ray spectroscopy uncovering the effects of Cu based nanoparticle concentration and structure on *Phaseolus vulgaris* germination and seedling development. **Journal of Agricultural and Food Chemistry**, Washington, DC, v. 65, n. 36, p. 7874-7884, 2017.

EL-TEMSAH, Y. S.; JONER, E. J. Impact of Fe and Ag nanoparticles on seed germination and differences in bioavailability during exposure in aqueous suspension and soil. **Environmental Toxicology**, New York, v. 27, n. 1, p. 42–49, 2012.

GAUTAM, R.; VANGA, S.; ARIESE, F.; UMAPATHY, S. Review of multidimensional data processing approaches for Raman and infrared spectroscopy. **EPJ Techniques and Instrumentation**, Heidelberg, v. 2, n. 1, p. 8, 2015.

GRIFFIN, B. A.; JURINAK, J. J. Estimation of activity coefficients from the electrical conductivity of natural aquatic systems and soil extracts. **Soil Science**, Baltimore, v. 116, n. 1, p. 26-30, 1973.

HOJJAT, S. S.; HOJJAT, H. Effect of nano silver on seed germination and seedling growth in Fenugreek Seed. **ETP International Journal of Food Engineering**, v. 1, n. 2, 2015.

JO, Y. K.; CROMWELL, W.; JEONG, H.-K.; THORKELSON, J.; ROH, J.-H.; SHIN, D.-B. Use of silver nanoparticles for managing Gibberella fujikuroi on rice seedlings. **Crop Protection**, Guildford, v. 74, p. 65–69, 2015.

KAČURÁKOVÁ, M.; MATHLOUTHI, M. FTIR and laser-Raman spectra of oligosaccharides in water: characterization of the glycosidic bond. **Carbohydrate Research**, Amsterdam, v. 284, n. 2, p. 145–157, 1996.

KHOT, L. R.; SANKARAN, S.; MAJA, J. M.; EHSANI, R.; SCHUSTER, E. W. Applications of nanomaterials in agricultural production and crop protection: a review. **Crop Protection**, Guildford , v. 35, p. 64–70, 2012.

KIKUCHI, K.; KOIZUMI, M.; ISHIDA, N.; KANO, H. Water uptake by dry beans observed by micro-magnetic resonance imaging. **Annals of Botany**, Oxford ,v. 98, n. 3, p. 545–553, 2006.

KOKURA, S.; HANDA, O.; TAKAGI, T.; ISHIKAWA, T.; NAITO, Y.; YOSHIKAWA, T. Silver nanoparticles as a safe preservative for use in cosmetics. **Nanomedicine: Nanotechnology, Biology and Medicine**, New York, v. 6, n. 4, p. 570–574, 2010.

KONG, J.; YU, S. Fourier transform infrared spectroscopic analysis of protein secondary structures. **Acta Biochimica et Biophysica Sinica**, Shanghai, v. 39, n. 8, p. 549–559, 2007.

KUMAR, S.; SHUKLA, A.; BAUL, P. P.; MITRA, A.; HALDER, D. Biodegradable hybrid nanocomposites of chitosan/gelatin and silver nanoparticles for active food packaging applications. **Food Packaging and Shelf Life**, Amsterdam, v. 16, p. 178–184, 2018.

LEVARD, C.; HOTZE, E. M.; LOWRY, G. V; BROWN, G. E. Environmental transformations of silver nanoparticles: impact on stability and toxicity. **Environmental Science & Technology**, Washington, v. 46, n. 13, p. 6900–6914, 2012.

LEVARD, C.; REINSCH, B. C.; MICHEL, F. M.; OUMAHI, C.; LOWRY, G. V.; BROWN, G. E. Sulfidation processes of PVP-Coated silver nanoparticles in aqueous solution: impact on dissolution rate. **Environmental Science & Technology**, Washington, DC, v. 45, n. 12, p. 5260–5266, 2011.

MAHAKHAM, W.; SARMAH, A. K.; MAENSIRI, S.; THEERAKULPISUT, P. Nanopriming technology for enhancing germination and starch metabolism of aged rice seeds using phytosynthesized silver nanoparticles. **Scientific Reports**, London, v. 7, n. 1, p. 8263, 2017.

MARÉCHAL, Y.; CHANZY, H. The hydrogen bond network in Iβ cellulose as observed by infrared spectrometry. **Journal of Molecular Structure**, Amsterdam , v. 523, n. 1, p. 183–196, 2000.

MELLO, J. I. de O.; BARBEDO, C. J.; SALATINO, A.; FIGUEIREDO-RIBEIRO, R. de C. L. Reserve carbohydrates and lipids from the seeds of four tropical tree species with different sensitivity to desiccation. **Brazilian Archives of Biology and Technology**, Curitiba, v. 53, n. 4, p. 889-899, 2010.

MOHAMED, A. K. S. H.; QAYYUM, M. F.; ABDEL-HADI, A. M.; REHMAN, R. A.; ALI, S.; RIZWAN, M. Interactive effect of salinity and silver nanoparticles on photosynthetic and biochemical parameters of wheat. **Archives of Agronomy and Soil Science**, Abingdon, v. 63, n. 12, p. 1736–1747, 2017.

MONNIER, G.; FRAHM, E.; LUO, B.; MISSAL, K. Developing FTIR microspectroscopy for analysis of plant residues on stone tools. **Journal of Archaeological Science**, London, v. 78, p. 158–178, 2017.

MUTHUKRISHNAN, R.; ROHINI, R. LASSO: A feature selection technique in predictive modeling for machine learning. 2016 IEEE International Conference on Advances in Computer Applications (ICACA).. p.18–20, 2016.

PALLAVI; MEHTA, C. M.; SRIVASTAVA, R.; ARORA, S.; SHARMA, A. K. Impact assessment of silver nanoparticles on plant growth and soil bacterial diversity. **3 Biotech**, Heidelberg, v. 6, n. 2, p. 254, 2016.

PARVEEN, A.; RAO, S. Effect of nanosilver on seed germination and seedling growth in *Pennisetum glaucum*. **Journal of Cluster Science**, New York, v. 26, n. 3, p. 693–701, 2015.

PRABHU, S.; POULOSE, E. K. Silver nanoparticles: mechanism of antimicrobial action, synthesis, medical applications, and toxicity effects. **International Nano Letters**, Kermanshah, v. 2, n. 1, p. 32, 2012.

PRADAS DEL REAL, A. E.; VIDAL, V.; CARRIÈRE, M.; CASTILLO-MICHEL, H.; LEVARD, C.; CHAURAND, P.; SARRET, G. Silver nanoparticles and wheat roots: a complex interplay. **Environmental Science & Technology**, Washington, DC, v. 51, n. 10, p. 5774–5782, 2017.

REGVAR, M.; EICHERT, D.; KAULICH, B.; GIANONCELLI, A.; PONGRAC, P.; VOGEL-MIKUŠ, K. Biochemical characterization of cell types within leaves of metal-hyperaccumulating Noccaea praecox (Brassicaceae). **Plant and Soil**, The Hague, v. 373, n. 1, p. 157–171, 2013.

RODRIGUES, E. S.; GOMES, M. H. F.; DURAN, N. M.; CASSANJI, J. G. B.; CRUZ, T. N. M.; SANT'ANNA NETO, A.; SAVASSA, S. M.; ALMEIDA, E. de; CARVALHO, H. W. P. Laboratory microprobe X-ray fluorescence in plant science: emerging applications and case studies. **Frontiers in Plant Science**, Lausanne, v. 9, p. 1588, 2018. doi: 10.3389/fpls.2018.01588.

SALAMA, H. M. H. Effects of silver nanoparticles in some crop plants, common bean (*Phaseolus vulgaris* L.) and corn (*Zea mays* L.). **International Research Journal of Biotechnology**, Sapele, Nigeria, v. 3, n. 10, p. 190–197, 2012.

SALOMÉ, M.; COTTE, M.; BAKER, R.; BARRETT, R.; BENSENY-CASES, N.; BERRUYER, G.; BUGNAZET, D.; CASTILLO-MICHEL, H.; CORNU, C.; FAYARD, B.; GAGLIARDINI, E.; HINO, R.; MORSE, J.; PAPILLON, E.; POUYET, E.; RIVARD, C.; SOLÉ, V. A.; SUSINI, J.; VERONESI, G. The ID21 Scanning X-ray Microscope at ESRF. **Journal of Physics: Conference Series**, Bristol, v. 425, n. 18, p. 182004, 2013.

SAVASSA, S. M.; DURAN, N. M.; RODRIGUES, E. S.; ALMEIDA, E. de; VAN GESTEL, C. A. M.; BOMPADRE, T. F. V.; CARVALHO, H. W. P. de. Effects of ZnO nanoparticles on Phaseolus vulgaris germination and seedling development determined by X-ray spectroscopy. **ACS Applied Nano Materials**, Washington, DC, v. 1, n. 11, p. 6414–6426, 2018.

SHARMA, P.; BHATT, D.; ZAIDI, M. G. H.; SARADHI, P. P.; KHANNA, P. K.; ARORA, S. Silver nanoparticle mediated enhancement in growth and antioxidant status of Brassica juncea. **Applied Biochemistry and Biotechnology**, Clifton, v. 167, n. 8, p. 2225–2233, 2012.

SHTEIN, I.; BAR-ON, B.; POPPER, Z. A. Plant and algal structure: from cell walls to biomechanical function. **Physiologia Plantarum**, Copenhagen, v. 164, n. 1, p. 56–66, 2018.

SMÝKAL, P.; VERNOUD, V.; BLAIR, M. W.; SOUKUP, A.; THOMPSON, R. D. The role of the testa during development and in establishment of dormancy of the legume seed. **Frontiers in Plant Science**, Lausanne, v. 5, p. 351, 2014.

SONG, U.; JUN, H.; WALDMAN, B.; ROH, J.; KIM, Y.; YI, J.; LEE, E. J. Functional analyses of nanoparticle toxicity: A comparative study of the effects of TiO2 and Ag on tomatoes (*Lycopersicon esculentum*). **Ecotoxicology and Environmental Safety**, Amsterdam, v. 93, p. 60–67, 2013.

SPIELMAN-SUN, E.; ZAIKOVA, T.; DANKOVICH, T.; YUN, J.; RYAN, M.; HUTCHISON, J. E.; LOWRY, G. V. Effect of silver concentration and chemical transformations on release and antibacterial efficacy in silver-containing textiles. **NanoImpact**, Amsterdam, v. 11, p. 51–57, 2018.

SPURNÝ, M. Spiral feedback oscillations of growing hypocotyl with radicle in *Pisum sativum* L. **Biologia Plantarum**, Praha, v. 8, n. 5, p. 381, 1966.

SUSINI, J.; COTTE, M.; SCHEIDT, K.; CHUBAR, O.; POLACK, F.; DUMAS, P. Technical report: the FTIR Spectro microscopy end station at the ESRF-ID21 Beamline. **Synchrotron Radiation News**, New York, v. 20, n. 5, p. 13–16, 2007.

TALARI, A. C. S.; MARTINEZ, M. A. G.; MOVASAGHI, Z.; REHMAN, S.; REHMAN, I. U. Advances in Fourier transform infrared (FTIR) spectroscopy of biological tissues. **Applied Spectroscopy Reviews**, Abingdon, v. 52, n. 5, p. 456–506, 2017.

TIAN, J.; WONG, K. K.; HO, C.-M.; LOK, C. N.; YU, W. Y.; CHE, C. M.; CHIU, J. F.; TAM, P. K. Topical delivery of silver nanoparticles promotes wound healing. **ChemMedChem**, Weinheim, v. 2, n. 1, p. 129–136, 2007.

TIBSHIRANI, R. Regression shrinkage and selection via the lasso. **Journal of the Royal Statistical Society. Series B (Methodological)**, London, v. 58, n. 1, p. 267–288, 1996.

TOPLAK, M.; BIRARDA, G.; READ, S.; SANDT, C.; ROSENDAHL, S. M.; VACCARI, L.; DEMŠAR, J.; BORONDICS, F. Infrared orange: connecting hyperspectral data with machine learning. **Synchrotron Radiation News**, New York, v. 30, n. 4, p. 40–45, 2017.

TÜRKER-KAIA. S.; HUCK, W. C. A Review of mid-infrared and near-infrared imaging: principles, concepts and applications in plant tissue analysis. **Molecules**, Basel, v. 22, n. 1, 2017.

VANNINI, C.; DOMINGO, G.; ONELLI, E.; PRINSI, B.; MARSONI, M.; ESPEN, L.; BRACALE, M. Morphological and proteomic responses of Eruca sativa exposed to silver nanoparticles or silver nitrate. **Plos One**, San Francisco , v. 8, n. 7, p. e68752, 2013.

VARIER, A.; VARI, A. K.; DADLANI, M. The subcellular basis of seed priming. **Current Science**, Bangalore, v. 99, n. 4, p. 450–456, 2010.

WANG, P.; LOMBI, E.; SUN, S.; SCHECKEL, K. G.; MALYSHEVA, A.; McKENNA, B. A.; MENZIES, N. W.; ZHAO, F.-J.; KOPITTKE, P. M. Characterizing the uptake, accumulation and toxicity of silver sulfide nanoparticles in plants. **Environmental Science: Nano**, London, v. 4, n. 2, p. 448–460, 2017.

WANG, P.; MENZIES, N. W.; LOMBI, E.; McKENNA, B. A.; JOHANNESSEN, B.; GLOVER, C. J.; KAPPEN, P.; KOPITTKE, P. M. Fate of ZnO nanoparticles in soils and Cowpea (*Vigna unguiculata*). **Environmental Science & Technology**, Washington, DC, v. 47, n. 23, p. 13822–13830, 2013.

WIERCIGROCH, E.; SZAFRANIEC, E.; CZAMARA, K.; PACIA, M. Z.; MAJZNER, K.; KOCHAN, K.; KACZOR, A.; BARANSKA, M.; MALEK, K. Raman and infrared spectroscopy of carbohydrates: a review. **Spectrochimica Acta Part A: Molecular and Biomolecular Spectroscopy**, Amsterdam, v. 185, p. 317–335, 2017.

YAN, A.; CHEN, Z. Impacts of silver nanoparticles on plants: a focus on the phytotoxicity and underlying mechanism. **International Journal of Molecular Sciences**, Basel, v. 20, n. 5, 2019. doi: 10.3390/ijms20051003.

ZANOTTI, R. F.; MOTTA, L. B.; BRAGATTO, J.; LABATE, C. A.; SALOMÃO, A. N.; VENDRAME, W. A.; CUZZUOL, G. R. F. Germination, carbohydrate composition and vigor of cryopreserved Caesalpinia echinata seeds. **Brazilian Archives of Biology and Technology**, Curitiba, v. 55, n. 5, p. 661-669, 2012.

ZEIER, J.; SCHREIBER, L. Fourier transform infrared-spectroscopic characterisation of isolated endodermal cell walls from plant roots: chemical nature in relation to anatomical development. **Planta**, New York, v. 209, n. 4, p. 537–542, 1999.

ZHU, Y.; TAN, T. L. Penalized discriminant analysis for the detection of wild-grown and cultivated Ganoderma lucidum using Fourier transform infrared spectroscopy. **Spectrochimica Acta Part A: Molecular and Biomolecular Spectroscopy**, Amsterdam, v. 159, p. 68–77, 2016.

ZUVERZA-MENA, N.; ARMENDARIZ, R.; PERALTA-VIDEA, J. R.; GARDEA-TORRESDEY, J. L. Effects of silver nanoparticles on radish sprouts: root growth reduction and modifications in the nutritional value. **Frontiers in Plant Science**, Lausanne, v. 7, p. 90, 2016. doi: 10.3389/fpls.2016.00090.

4 APPLICATION OF MICROPROBE SYNCHROTRON TECHNIQUES TO UNDERSTAND THE INTERACTION OF ZnO NANOPARTICLES IN *Phaseolus vulgaris* SEED COAT

Abstract

In the last decade, the use of nanomaterials in commercial products sharply increased. In agriculture, it is mainly applied as fertilizers and pesticides. Seed treatment is a common practice that provides micronutrients and protection,enhancing germination and plant development. This study investigated the interaction of zinc sources ($ZnSO_4$ and ZnO 40 nm) in common bean seed coat after germination. Scanning electron microscopy (SEM) images showed ZnO nanoparticles clusters in the edge of the hilum and around the micropyle. X-ray fluorescence microanalysis (µ-XRF) for seed coat samples treated with both sources revealed a concentration gradient of Zn from the middle layers towards the cuticle (most external layer) and parenchyma (most internal). X-ray absorption spectroscopy (XAS) showed that the Zn incorporated by the seed coat was biotransformed, into a mixture of Zn-citrate and Zn-malate, regardless of the Zn source used in priming. Attenuated total reflectance Fourier transform infrared (ATR-FTIR) and FTIR microscopy (µ-FTIR) analysis allowed to identify differences mainly in carbohydrate and protein groups in the layers of common bean seed coat samples exposed to ZnO 40 nm and $ZnSO_4$ at 100 and 1000 mg L^{-1}. Altogether, these results presented an overview of the interaction of the tested Zn sources with the seed coat after five days of germination.

Keywords: Microprobe X-ray fluorescence spectroscopy, Micro-X-ray absorption near-edge structure, common bean, seed coat

4.1 Introduction

The proper supply of macro and micronutrients throughout plant development is the mainkey for a well succeeded crop. Zinc (Zn) plays an important role in several physiological and metabolism processes like gene expression, enzyme activation, synthesis of proteins, metabolism of carbohydrates, lipids, nucleic acids and auxins (BROADLEY et al., 2012). However, about 50% of crops grows in Zn-deficient soils worldwide (ALLOWAY, 2009). Soils low in available Zn usually generates plants with low yield capability and nutritionally poor (WELCH; GRAHAM, 1999).

To increase the Zn concentration in plants and promote its development, many approaches to Zn fertilization are in use. Besides the conventional broadcasting and foliar application, which can cause nutrient losses and require high-cost machinery, an alternative method to complement plant fertilization consist of seed priming, in which nutrient is effectively provided in an inexpensive way, since it demands few inputs and affordable technologies (HARRIS et al., 2007).

Currently, seed priming with nanoparticles has gained importance due to unique physicochemical characteristics of nanomaterials that are capable to boost crop development and yield (JOSHI et al., 2018). Nanomaterials interact with cells and interfere in key vital processes of the early plant growth stages such as germination rate (GOKAK; TARANATH, 2015), seedling and root development (LI et al., 2015) and cellular metabolism (BABAJANI et al., 2019; KASOTE et al., 2019). Seed priming with nanomaterials is also a promising approach to grains biofortification to combat malnutrition (SUNDARIA et al., 2019).

Seeds primed with zinc oxide (ZnO) nanoparticles improved seedling growth and Zn concentration in roots, shoots and grains of wheat (MUNIR et al., 2018; ELHAJ BADDAR; UNRINE, 2018). Also raised the number of germinated seeds and accelerated the growth of roots and leaves of soybean (HOE et al., 2018). In pearl millet, ZnO nanoparticles enhanced seed germination, vigor, seedling growth and the activity of defense enzymes (NANDHINI et al., 2019).

Common bean seeds are covered by seed coat that give the embryo protection against mechanical stress and pathogens, and also control gas exchange and water uptake (QUTOB et al., 2008). The outermost layer of the seed coat is the waxy cuticle followed by the macrosclereids, that are elongated palisade cells with the long axis oriented perpendicularly to the surface. The next layer is the osteosclereids, which is characterized by extensive network of intercellular spaces. The fourth and the deepest layer consists of elongated parenchyma cells that also have prominent intercellular spaces (YEUNG, 1983; SOUZA; MARCOS-FILHO, 2001). Thus, it is possible that these layers respond differently to the application of seed priming compounds.

A previous work demonstrated that P. vulgaris seeds soaked in ZnO 40 nm dispersion prior to germination resulted in seedlings with the highest weight gain when compared to those treated with ZnSO4 and other ZnO nanoparticles sizes. Moreover, most of the applied Zn remained trapped in the seed coat (SAVASSA et al., 2018). Therefore, this study aimed to investigate the interactions between Zn sources ($ZnSO_4$ and ZnO 40 nm) and common beans seed coat. Scanning electron microscopy (SEM) exhibited the distribution of these sources on the seed coat surface. X-ray fluorescence spectroscopy (XRF) uncovered the Zn storage location whilst X-ray absorption near edge spectroscopy (XANES) revealed the Zn chemical environment within the treated seed coats. Fourier transform infrared (FTIR) determined differences in the organic profile of the seed coat layers.

4.2 Materials and Methods

4.2.1 Nanoparticles dispersion and common bean seeds

The nanoparticle ZnO 40 nm (MK Impex Corp.) tested in this study was previously characterized (SAVASSA et al., 2018). $ZnSO_4 \cdot 7H_2O$ (MERCK KGaA, Germany) was used as the ionic treatment (Zn^{2+}). The nanoparticles were suspended in deionized water and dispersed using a Sonics and Materials Vibra-Cell™ CV18 (Sonics and Materials Inc., USA) (130 watts) at 100, 1000 and 5000 mg L^{-1}.

Phaseolus vulgaris seeds (variety IAC Sintonia) used in this work were supplied by the Agronomic Institute of Campinas (IAC; Brazil) (CHIORATO et al., 2018). Seeds were washed with 10% NaClO solution and rinsed in deionized water, and then soaked for one hour in ZnO 40 nm dispersions and $ZnSO_4$ solutions, both at 100, 1000 and 5000 mg L^{-1}. Deionized water was used as control. After soaking, the seeds were transferred to Petri dishes covered with filter paper moistened with water and finally incubated for germination during five days at 27 ◦C.

4.2.2 Scanning electron microscopy (SEM)

Five seeds treated with ZnO 40 nm and $ZnSO_4$ at 5000 mg L^{-1}, and a control seed (treated only with deionized water) were used for SEM analysis. The hilum region was sampled with the aid of a scalpel blade, glued to carbon tape on aluminum stubs, gold coated (Bal-tec model SCD 050), and analyzed with a scanning electron microscope (Jeol - JSM IT 300) at 15 kV and digitally recorded at a working distance of 15 mm.

4.2.3 Microprobe X-ray fluorescence spectroscopy (µ-XRF) and micro-X-ray absorption near-edge structure (µ-XANES)

µ-XRF was employed to obtain chemical maps of Zn in the treated seed coat samples. For this purpose, treated seed coat fractions (around 0.2 x 0.2 cm^2) were collected and embedded in OCT resin, cryofixed in liquid nitrogen (LN2) and cryo-sectioned in 50 µm thick slices using a cryostat (Leica CM1850). The cross-sections were placed between ultralene films accoupled in a plastic sample holder (Figure S1) and freeze-dried.

The 2D spatial distribution of Zn in the samples were mapped using a benchtop µ-XRF equipment (Orbis PC, EDAX, USA) operated with a Rh anode X-ray tube working at 40 kV and 300 µA and equipped with a poly-capillary optical element to focus it down to 30 µm in diameter and a 30 mm^2 silicon drift detector with a resolution of 140 eV for Mn-Kα. The maps were obtained using a matrix of 32 × 25 points and dwell time of 2000 msec per point.

The µ-XANES analysis were carried out at the Zn K edge at XRF beamline of Brazilian Synchrotron Light Laboratory (LNLS). The beamline is composed of a bending-magnet, Si (111) double crystal monochromator, KB mirror system given a 20 µm diameter spot size beam, and silicon drift detector (SDD; KETEK GmbH, Germany).

4.2.4 Fourier transform infrared analysis

The Fourier transform infrared (FTIR) analysis from this work were performed at ID21 beamline of the European Synchrotron Radiation Facility (ESRF) (SUSINI et al., 2007). The FTIR microscopy (µ-FTIR) end-station uses a Thermo Nicolet Nexus infrared spectrometer (Thermo Scientific, Madison, WT, USA) and Thermo Nicolet Continuum infrared microscope (Thermo Scientific, Madison, WT, USA).

Treated seed coat cross sections of 4 µm thick, were prepared analogously to µ-XRF and µ-XANES analysis. The sections were placed between two BaF_2 windows (0.4 mm thick) accoupled in a sample holder, freezed using LN2, and freeze-dried for 4 h under vacuum ($2x10^{-4}$ mbar) and low temperature (-50 ˚C) followed by 4 h under vacuum and brought up to room temperature.

Synchrotron µ-FTIR was carried out in transmission mode using a 10 × 10 µm² beam. Spectra (average of 128 scans) were recorded over a range of 3000 to 850 cm^{-1} and spectral resolution of 4 cm^{-1}. The external and internal surfaces of treated samples were cut in a circular shape (around 10 mm diameter), frozen in LN2 and freeze-dried to be analyzed by attenuated total reflectance Fourier transform infrared (ATR-FTIR) using a bench top equipment (Thermo Nicolet Nexus 4700 FT-IR Spectrometer).

All the acquired data were processed using Orange Data Mining software (TOPLAK et al., 2017). Linear Discriminant Analysis (LDA) and Principal Component Analysis (PCA) were used to clustering differently treated samples. The feature extraction was done using

Logistic Regression and Least Absolute Shrinkage and Selection Operator (LASSO). Using a K-fold cross validation method the model's robustness parameters AUC (Area Under Curve), receiver operating characteristics (ROC) curve, precision, and sensitivity (or recall) were monitored to ensure good quality of the model.

4.3 Results and Discussion

4.3.1 Scanning electron microscopy

A previous work demonstrated that germinated seeds of *P. vulgaris* whose seeds were soaked in ZnO dispersions and $ZnSO_4$ solutions prior to germination had Zn more concentrated in the seed coat, mainly in the hilum region (SAVASSA et al., 2018). However, microscopy images regarding the interaction between these two sources and the hilum were not provided. The hilum is the "scar" created in the seed surface when the seed is detached from the funicle (the stalk by which the seed is attached to the pod). The hilum along with the micropyle plays dominant role in water uptake during the soaking process (DESHPANDE; CHERYAN, 1986; MIKAC et al., 2015).

Figure 1 presents scanning electron-micrographs of the hilum region (including micropyle, rafe and lens) of control, ZnO 40 nm and $ZnSO_4$ treated bean seeds. One can note that, contrary to what was observed for $ZnSO_4$ and control samples, the ZnO nanoparticles formed clusters in the edge of the hilum and specially around the micropyle (Figures 1f-g). The hilum is composed by a spongy-like tissue and thus a favorable area for agglomeration.

Besides Zn, it was also demonstrated that common bean seeds soaked in Cu and Fe oxides nanoparticles dispersions accumulated these elements in the hilum region (DURAN et al., 2017; 2018). Additionally, X-ray spectroscopy and tomography combined to SEM showed that magnetite nanoparticles penetrated within the hilum (DURAN et al., 2018).

Figure 1. Scanning electron-micrographs of *Phaseolus vulgaris* seed surface after different treatments with 5000 mg L^{-1} Zn sources. (a)-(d) control samples; (e)-(h) ZnO 40 nm; (i)-(l) $ZnSO_4$. Arrows show ZnO 40 nm deposit around the hilum (f) and micropyle (g). HI – Hilum; MI- Micropyle; RA – Rafe; LE – Lens

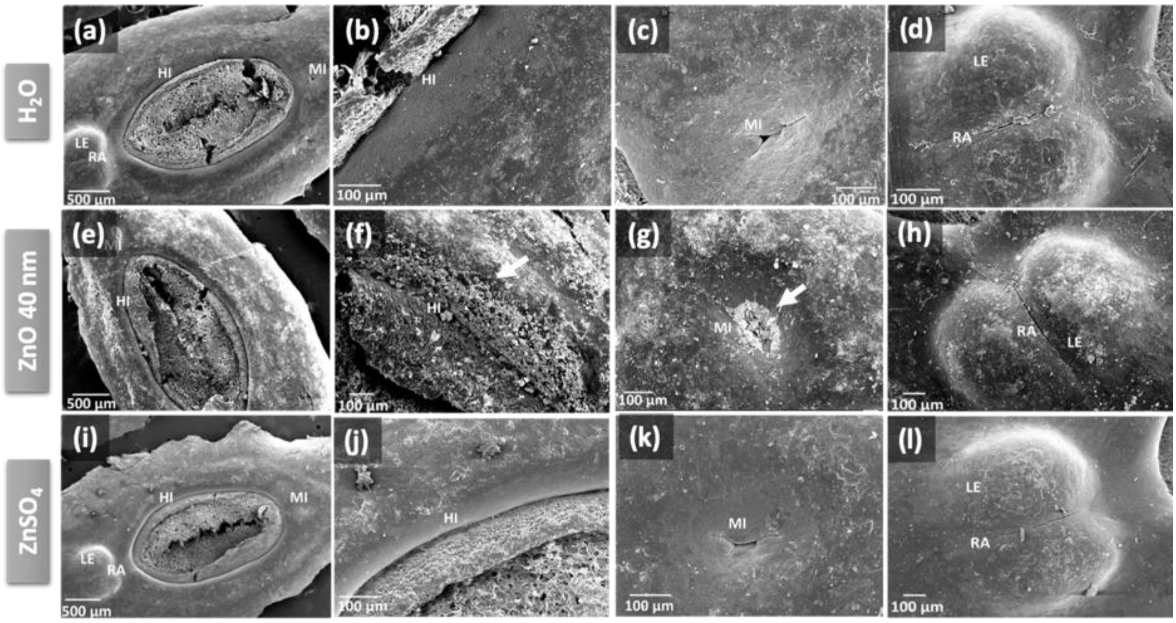

4.3.2 Zn localization and speciation within the seed coat

Figures 2a-b shows 50 µm-thick cross sections of *P. vulgaris* seed coats whose seeds were exposed to $ZnSO_4$ and ZnO 40 nm at 5000 mg L^{-1}, respectively. Albeit this concentration is too high for seed treatment and can lead to detrimental effects on seed germination and seedling development (SAVASSA et al., 2018), it was chosen in order to avoid lower detection limits of the technique employed. Moreover, the higher the analyte concentration, the lower the acquisition time for the measurements and consequently the sample is exposed to a lower radiation dose.

The 2D Zn chemical maps recorded for these sections were acquired by µ-XRF and are presented in Figures 2c (ZnO 40 nm) and 2d ($ZnSO_4$). For both sources, a concentration gradient of Zn from the middle layers towards the cuticle (most external layer) and parenchyma (most internal) is observable. However, Zn was more concentrated in the ionic treatment, which was expected since soluble Zn sources such as $ZnSO_4$ make Zn ions readily available for absorption than ZnO that present very low solubility.

With the Zn accumulation regions located, two points of the samples were selected to be probed by XANES since the Zn chemical environment can vary according to the position where the data is recorded. Figures 1a-b illustrates these points (referred to as P1 and P2). Figures 2e-f presents the normalized Zn-K edge XANES spectra recorded for $ZnSO_4$ and ZnO 40 nm treated samples, respectively, and for the reference compounds Zn-citrate and

Zn-malate. The spectral shape allows identify whether the incorporated Zn was biotransformed into the seed coats. For both treatments, P1 and P2 display Zn in a chemical environment similar to the reference compounds.

The linear combination fit (LCF) for each of these points are in Figure 3, this analysis allows identifying the proportion of each component in a mixture. The LCF fittings were done using Zn organic acid reference compounds (citrate and malate) that are good proxies for the Zn chemical environment in plant tissues (SARRET et al., 2002; 2004).

For $ZnSO_4$ treated sample, the LCF of the XANES spectra determined that P1 is a mixture of 57.9 ± 2.3% of Zn-citrate and 42.1 ± 5.4% of Zn-malate (Figure 3a), whereas P2 is a mixture of 24.1 ± 2.7% of Zn-citrate and 75.9 ± 5.9% of Zn-malate (Figure 3b). In the case of the samples exposed to ZnO 40 nm, the ratio found in P1 was 56.2 ± 3.5% of Zn-citrate and 43.8 ± 6.3% of Zn-malate (Figure 3c), while P2 was 47.3 ± 3.5% of Zn-citrate and 52.7 ± 6.3% of Zn-malate (Figure 3d).

In a previous work, chemical speciation analysis carried out in common bean seeds treated with ZnO 40 nm at 100 mg L^{-1} found Zn in the external seed coat surface as mixture of 14 ± 3% of pristine ZnO and 86 ± 3% of Zn-malate, and in the interface between seed coat and cotyledon as mixture of 37 ± 2% of pristine ZnO and 63 ± 2% of Zn-malate. Zn bound to citrate was only found for untreated sample (SAVASSA et al., 2018). It is possible to conclude that Zn interact differently with the seed coat layers. In the internal layers, Zn was found bonded only with organic acids and in different proportions than those found for the external tissues.

Some organic ligands, like malate and citrate, can be easily bonded with different metals including Zn and are present in different regions of the plants, such as vacuoles and xylem (TOLRA; POSCHENRIEDER; BARCELO, 1996). Malate and citrate participate in detoxification mechanisms (KOPITTKE et al., 2017).

Figure 2. Zn chemical maps and speciation. (a) and (b) 50 µm-thick cross sections of *Phaseolus vulgaris* seed coat. (c) and (d) Zn mapping of seed coat sections exposed to $ZnSO_4$ and ZnO 40 nm at 5000 mg L^{-1}, respectively. (e) and (f) normalized Zn-K edge XANES spectra recorded in P1 and P2 of the cross sections treated with $ZnSO_4$ and ZnO 40 nm, respectively, and reference compounds (Zn-citrate, Zn-malate)

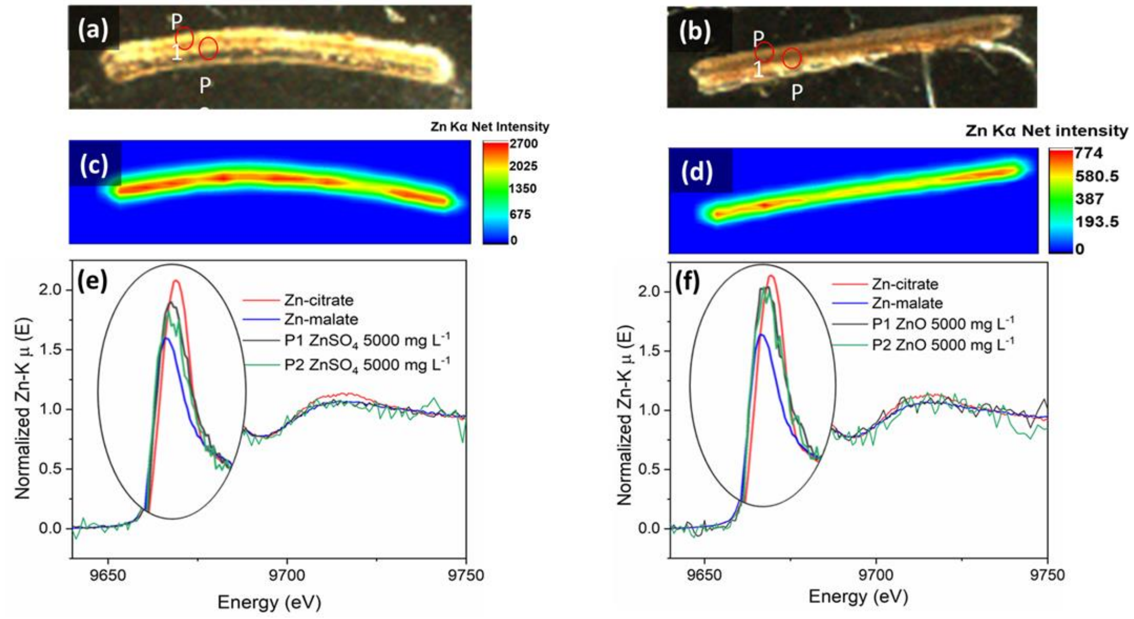

Figure 3. Linear combination fit for Zn-K edge XANES spectra recorded for (a) P1 (R-factor: 0.0058808) and (b) P2 (R-factor: 0.0088177) at the seed coat cross sections of *Phaseolus vulgaris* seeds treated with $ZnSO_4$ at 5000 mg L^{-1}; and for (c) P1 (R-factor: 0.0096479) and (d) P2 (R-factor: 0.0129750) at the seed coat cross sections of bean seeds treated with ZnO 40 nm at 5000 mg L^{-1}

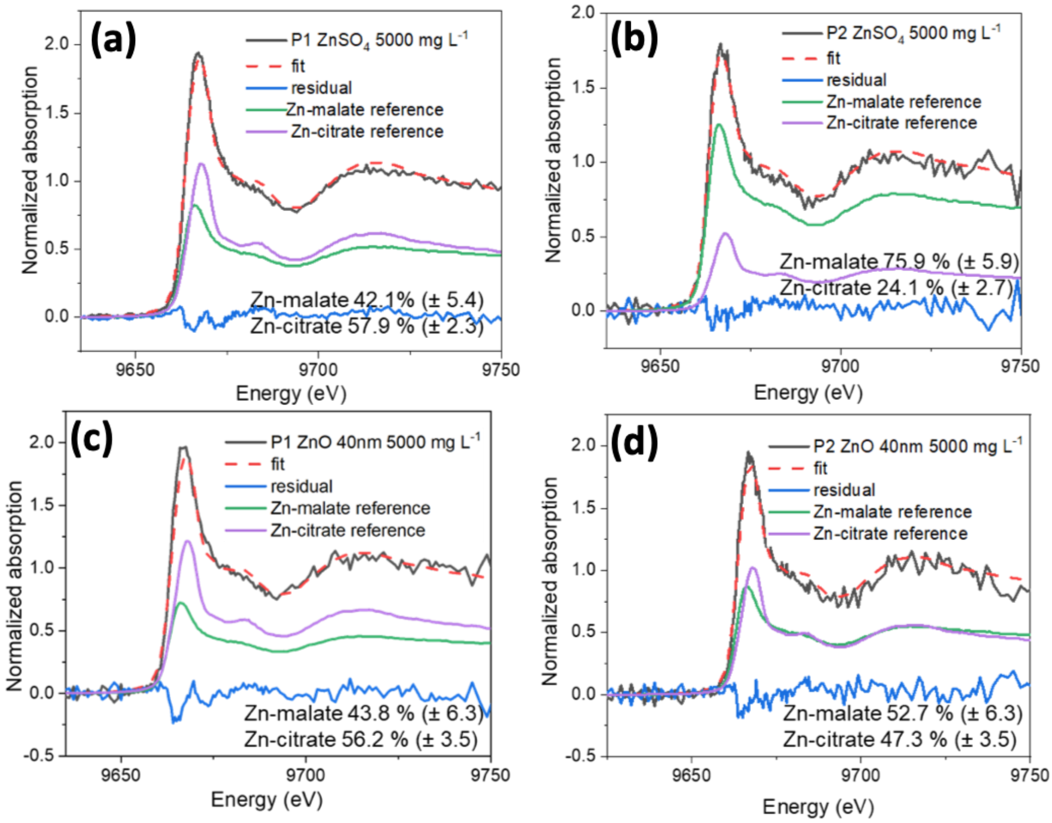

4.3.3 Fourier transform infrared analysis

Exposing plants to nanoparticles implies potential changes in their organic profile and nutritional properties (MORALES et al., 2013; SURESH et al., 2016). ATR-FTIR analysis was employed to identify changes in functional groups in the outer (cuticle) and inner surface (in contact with the embryo) of common bean seed coat samples exposed to ZnO 40 nm and $ZnSO_4$ at 100 and 1000 mg L^{-1}, including a sample treated only with water (control). It allowed to uncover possible changes in the main regions of the mid-IR spectrum, i.e. carbohydrates (800 - 1300 cm^{-1}), proteins (1400 – 1700 cm^{-1}) and lipids (2800 – 3000 cm^{-1}).

Firstly, all the acquired data were submitted to PC-LDA in order to reduce it and underline the most important and significant differences. The PC-LDA plots for the data obtained in the outer and inner surface of the seed coat are presented in Figures 4a and 4b, respectively.

For the outer surface (Figure 4a), it is possible to differentiate the control (H_2O) from the $ZnSO_4$ 100 mg L^{-1} and $ZnSO_4$ 1000 mg L^{-1} along component 1 (horizontal axis), suggesting a dose-dependent response. Regarding ZnO 40 nm, it can be observed that the clusters are not separated as good as $ZnSO_4$, the response was different for the lowest concentration ZnO 100 mg L^{-1}, which was the cluster most away from control. Also, it is important to consider the input from component 2 (vertical axis) in order to distinguish the nanoparticle from ionic treatments.

For the inner surface (Figure 4b), one can note good separation among groups. Along component 2 (vertical axis) there is the separation of Zn sources, and along component 1 (horizontal axis) there is the separation of the concentrations of treatments.

Figure 4. PC-LDA plots from ATR-FTIR analysis for common bean seed coat in the (a) external surface (cuticle) and in the (b) inner surface (parenchyma). Samples were treated with water, ZnO 40 nm and $ZnSO_4$ at 100 and 1000 mg L^{-1}. Different colors correspond to different groups

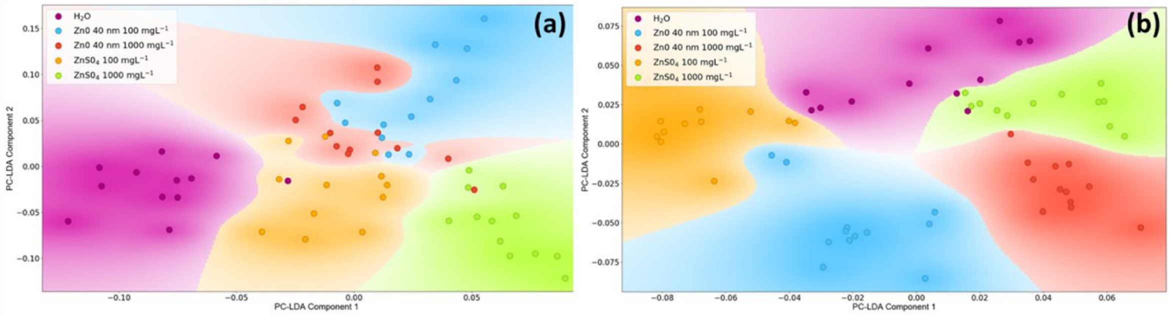

The organic profile of the seed coat samples was then determined by applying a consistent statistical regression model in the acquired FTIR data set. The chosen model is based principally in Logistic Regression and LASSO (TIBSHIRANI, 1996; MUTHUKRISHNAN; ROHINI, 2016). Figure 5a shows the mean spectra from the outer surface and Figure 5b from the inner surface with weighted LASSO regression coefficients. Two-fold cross validation parameters for this model are for external AUC = 0.977, Precision = 0.868, and Recall=0.867; and for the inner AUC = 0.999, Precision = 0.954, and Recall = 0.950, optimal values according to (GAUTAM et al., 2015).

The chemical assignment was conducted by examining each of the peaks obtained by LASSO and, based on the literature, they were assigned to chemical compounds that can be absorbed in the selected region of the FTIR spectra. Table 1 presents the main assignments.

Table 1. Chemical assignment of FTIR spectral bands selected by LASSO method for inner and outer seed coat surface samples

Wavenumber range (cm^{-1})	**Seed coat region**	**Attributions**	**Main Compounds**	**Ref.**
836	Outer	C–O–C	Carbohydrate molecule	(BUTA et al., 2015)
837	Inner	C–O–C (α-glycosidic bond)	Carbohydrate molecule	(BUTA et al., 2015)
876	Outer	ν(C–O)	B–d-fructose	(TÜRKER-KAYA; HUCK, 2017)
891	Outer	C–H deformation	Carbohydrate molecule	(TÜRKER-KAYA; HUCK, 2017)
935	Inner	ν(CO)	C-O-C linkages	(KAČURÁKOVÁ; MATHLOUTHI, 1996)
945	Outer	combination of ν(CO)ring, ν(CC) and β(CCH)	D-(-)-ribose	(WIERCIGROCH et al., 2017)
990	Outer	δ(CO)	Cellulose	(MARÉCHAL; CHANZY, 2000)
992 - 994	Outer	C–O stretch	Cutin	(TÜRKER-KAYA; HUCK, 2017)

Table 1 (continued)

1032	Inner	ν(C–O), ν(C–C)	Cellulose	(MONNIER et al., 2017)
1035 – 1037	Inner / outer	ν(OH), ν(C–OH)	Cell wall polysaccharides (arabinan)	(ZHU; TAN, 2016)
1038 – 1039	Inner / outer	O–H and C–OH stretch: cell wall polysaccharides	Arabinan, cellulose	(TÜRKER-KAYA; HUCK, 2017)
1045	Outer	ν(C-O), ν(C-C), ν(C=C), ν(COC)	Pectin, various polysaccharides, also suberin or cutin	(REGVAR et al., 2013)
1051 – 1054	Inner	C–O–C stretch; C–OH stretch; C–OH deformation; C–O–C deformation	Carbohydrate molecule	(BUTA et al., 2015)
1060	Outer	C–O stretch	Cell wall polysaccharides	(TÜRKER-KAYA; HUCK, 2017)
1074	Inner	pyranose, and furanose ring	Amylopectin and amylose	(KAČURÁKOVÁ; MATHLOUTHI, 1996)
1076 – 1077	Inner / outer	β(COH)	Amylopectin and amylose	(KAČURÁKOVÁ; MATHLOUTHI, 1996)
1083	Outer	C–O deformation	Secondary alcohol, aliphatic ester	(TÜRKER-KAYA; HUCK, 2017)
1108	Inner	C–O–C sym stretch	Cutin	(TÜRKER-KAYA; HUCK, 2017)
1131 – 1133	Inner / outer	ν(C-O)	L-(+)-arabinose	(KAČURÁKOVÁ; MATHLOUTHI, 1996)
1142	Inner / outer	C–O–C asym stretch	Cellulose	(TÜRKER-KAYA; HUCK, 2017)
1149	Outer	ν(COC), ν(CC)	Amylopectin and amylose	(KAČURÁKOVÁ; MATHLOUTHI, 1996)

Table 1 (continued)

1246	Outer	C=O stretch	Pectic substances, lignin, hemicellulose, suberin/cutin esters	(TÜRKER-KAYA; HUCK, 2017)
1427	Inner	δ(O–H)	Cell wall polysaccharide, alcohol, and carboxylic acid	(TÜRKER-KAYA; HUCK, 2017)
1446	Inner	δas(C–H) of CH_2 and CH_3	Cell wall polysaccharide, alcohol, and carboxylic acid	(TÜRKER-KAYA; HUCK, 2017)
1507 - 1508	Inner / outer	ν(C=C) aromatic	Lignin	(TÜRKER-KAYA; HUCK, 2017)
1515	Inner / outer	C=C aromatic strech	Lignin	(TÜRKER-KAYA; HUCK, 2017)
1539 - 1549	Inner / outer	ν(C=N); ν(N–H)	Amide II	(TÜRKER-KAYA; HUCK, 2017)
1622 - 1629	Inner / outer	C=C stretch	Phenolic compound	(TÜRKER-KAYA; HUCK, 2017)
1633 - 1651	Inner / outer	amide I (C=O strech)	Protein, pectin, water associated cellulose or lignin, alkaloids	(TÜRKER-KAYA; HUCK, 2017)
1733 - 1742	Inner / outer	saturated ester C=O strech	Phospholipid, cholesterol ester, hemicellulose, pectin, lignin, suberin/cutin esters	(TÜRKER-KAYA; HUCK, 2017)
2846 - 2848	Inner / outer	νs(CH_2)	Mainly lipids with a little contribution from protein, carbohydrate and nucleic acid	(TÜRKER-KAYA; HUCK, 2017)
2922 - 2925	Inner / outer	νas(CH_2)	Mainly lipid with a little contribution from protein, carbohydrate and nucleic acid	(TÜRKER-KAYA; HUCK, 2017)

Key: ν - stretching, as – asymmetric, s - symmetric, β – in-plane bending, δ - scissoring, ω - wagging, τ - twisting, def – deformation.

In the outer seed coat surface (Figure 5a), most notorious differences were found in the carbohydrate region, most of them associated with general polysaccharides such as cellulose, amylopectin and amylose. The variation observed in the range 1400 cm^{-1} to 1700 cm^{-1} regards to peaks mainly correlated to lignin, pectin, cell wall polysaccharide and hemicellulose. The lipid region presented few and low intensity peaks, indicating that no expressive lipidic differences occurred among the treatments.

In the inner surface (Figure 5a) case, the main divergences occurred in the range 1400 cm^{-1} to 1700 cm^{-1}, it is possible to see a peak (shoulder) at around 1645 cm^{-1} assigned to amide I from protein. Comparing with the outer surface (Figure 5b) it is noticed that this shoulder is prominent in the inner layer indicating that has more protein than the outer layer. But also that there are differences for the treatments, where the $ZnSO_4$ treated samples seems to have less protein. Protein is essential to a seed as source nitrogen to embryo development and synthesis of new enzymes (BEWLEY; BLACK, 1994). It is also possible to observe prominent differences for both surfaces in the FTIR spectra from 850 cm^{-1} to 1200 cm^{-1}. In the outer surface (Figure 5a) the absorbance pattern is smoother, while in the inner surface (Figure 5b) clear features at 1100 cm^{-1}, 1030 cm^{-1} and 1000 cm^{-1} can be noticed, including an intense one at 830 cm-1 that is not present in the FTIR spectra for the outer surface.

Figure 5. Mean spectra from ATR-FTIR analysis for the (a) outer surface (cuticle) and the (b) inner surface (parenchyma) of common bean seed coat treated samples with weighted LASSO regression coefficients

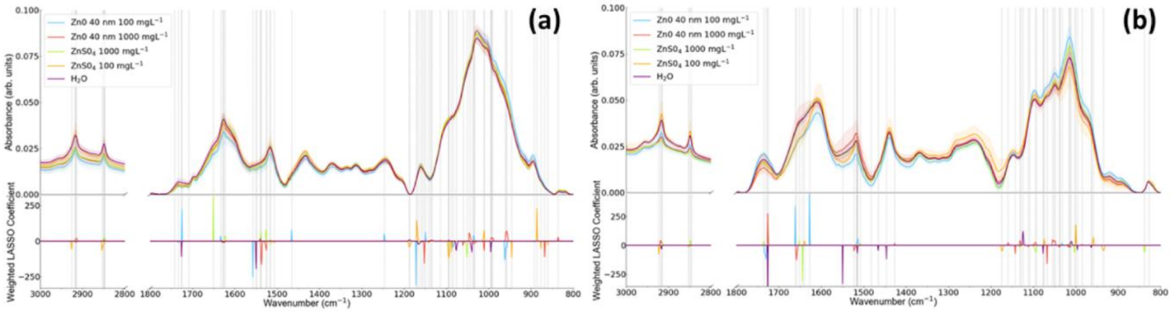

Although ATR-FTIR provided valuable information regarding the seed coat surfaces, it cannot specify if the treatments affected the organic profile of the seed coat internally. For this purpose, µ-FTIR was employed to identify the internal organic composition of the external (macrosclereids), middle (osteosclereids) and inner (parenchyma) layers of common bean seed coat. The samples consisted of 4-µm-thick seed coat slices exposed to ZnO 40 nm at 100 mg L^{-1} and $ZnSO_4$ at 100 and 1000 mg L^{-1}, and a sample treated only with water (control). The reason why a sample treated with ZnO 40 nm at 1000 mg L^{-1} was not included in this batch is due to the poor signal quality obtained for this sample during µ-FTIR analysis, this effect is likely due to scattering by the large nanoparticles agglomerates that are formed at this high concentration treatment.

Figure 6 shows the PC-LDA plots obtained from the µ-FTIR dataset. For the three tissues it is possible observe a group separation for treatments and the control (H_2O). At the macrosclereids layer (Figure 6a) and parenchyma tissue layer (Figure 6c), along component 1 (horizontal axis) it is possible to observe $ZnSO_4$ 1000 mg L^{-1} treatment are grouped in the most opposite side of the control (H_2O). For osteosclereids layer (Figure 6b) it is not so clear which group is in the opposite direction to the control but also have good separation of groups between the treatments.

Figure 7 shows the µ-FTIR mean spectra from the macrosclereids, osteosclereids and parenchyma layers with weighted LASSO regression coefficients. Two-fold cross validation parameters are to external layer, Figure 7a AUC = 0.974, Precision = 0.883, and Recall = 0.878, to middle layer, Figure 7b, AUC = 0.981, Precision = 0.915 , and Recall = 0.910 and to internal layer, Figure 7c, AUC = 0.957, Precision = 0.852 , and Recall = 0.840, again, optimal values according to (GAUTAM et al., 2015). Since the LASSO models did not point out relevant features in the highest wavenumbers regions, i.e. the lipid region of the mid-IR spectrum, it was only presented the spectral wavenumber range from 900 cm^{-1} to 1800 cm^{-1}.

Figure 6. PC-LDA plots from µ-FTIR analysis for common bean seed coat in the (a) external layer (macrosclereids), (b) middle layer (osteosclereids) and (c) inner layer (parenchyma tissue). Samples were treated with water, ZnO 40 nm and $ZnSO_4$ at 100 and 1000 mg L^{-1}. Different colors correspond to different groups

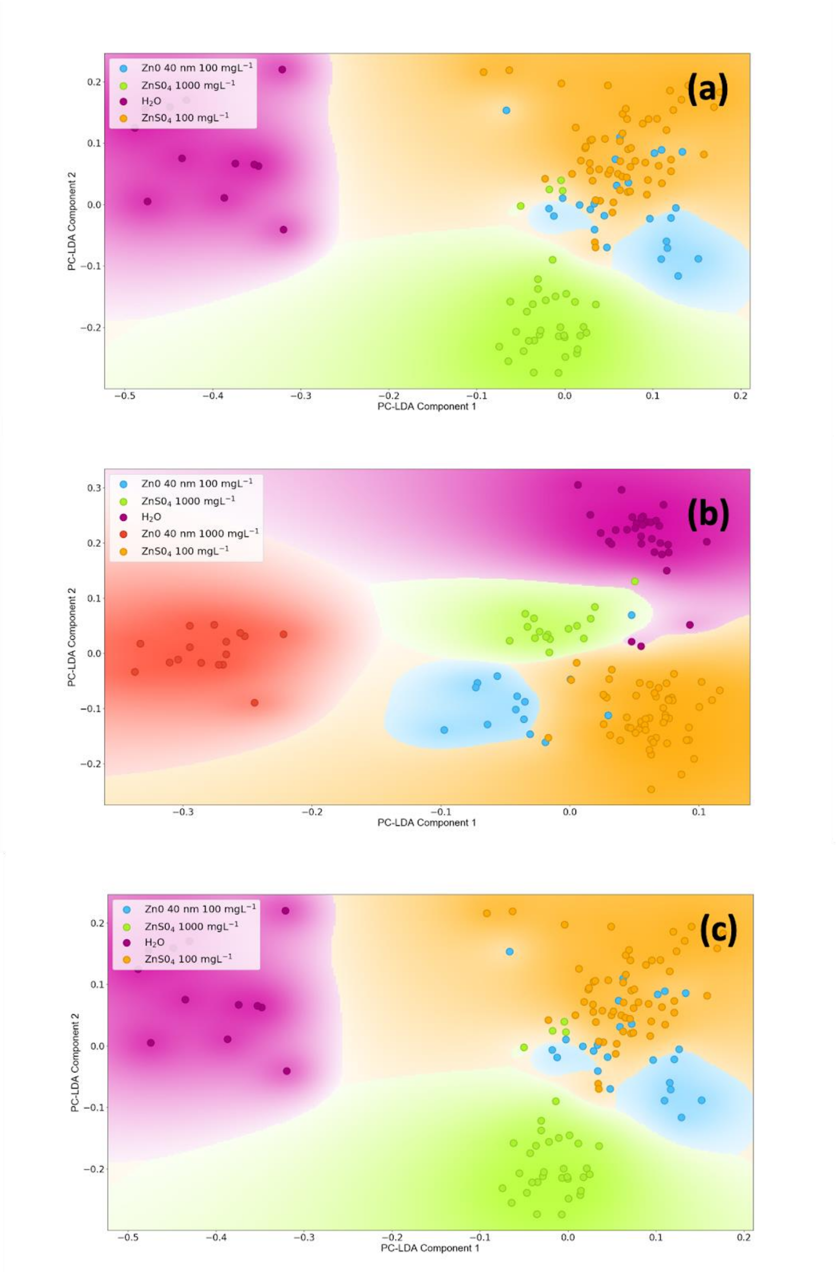

Figure 7. Mean spectra from µ-FTIR analysis for the (a) external layer (macrosclereids), (b) middle layer (osteosclereids) and (c) inner layer (parenchyma tissue) of common bean seed coat treated samples with weighted Lasso regression coefficients

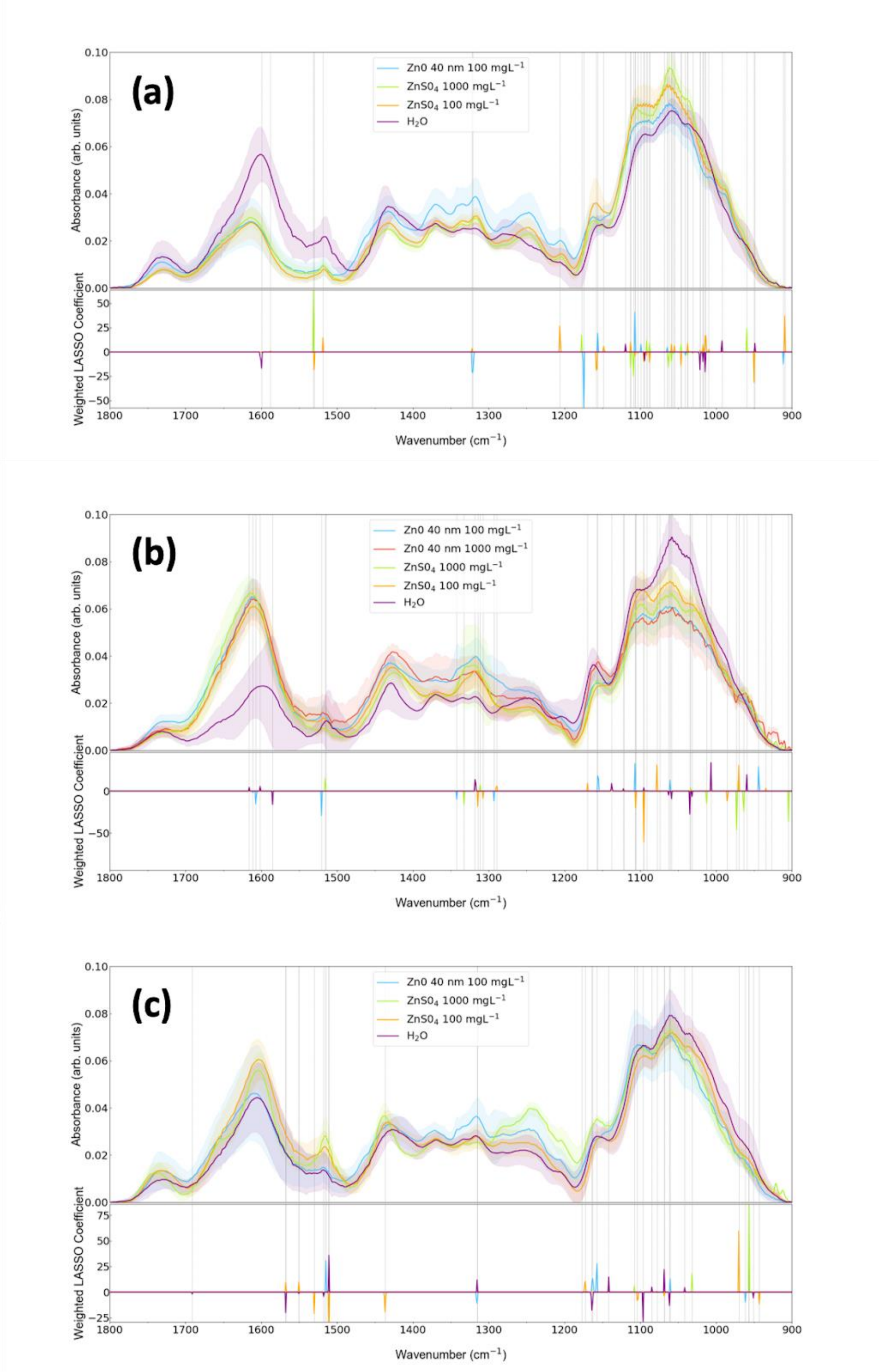

The detailed chemical assignments of the peaks are shown in Table 2. Few differences were observed among the three spectra. Differences were observed among the three spectra. Figures 7a and 7b presents big changes in the absorbances. In Figure 7a, control showed intense band at 1600 cm^{-1} while the bands for the Zn treatments were low and shifted. Figure 7b shows the opposite, treatments presented more intense bands at 1600 cm^{-1} compared with control and it is possible to see a shift to high wavenumbers. Figure 7b also presents changes in the absorbance at 1050 cm^{-1} for control.

Cucumber fruits from plants cultivated in substrate with the addition of ZnO 10 nm at 400 and 800 mg kg^{-1} presented FTIR data with altered carbohydrate pattern when compared to control (ZHAO et al., 2014). Changes in the peptide-protein, lipids, lignin, polysaccharides, hemicellulose, cellulose, and carbohydrate bands were also found for roots and shoots of maize seedlings whose seeds were coated with ZnO nanoparticles (76–334 nm) at 1600 ppm (ESTRADA-URBINA et al., 2018).

Table 2. Chemical assignment of FTIR spectral bands selected by LASSO method for outer (macrosclereids), middle (osteosclereids) and outer (parenchyma) tissues of common bean seed coat samples

Wavenumber range (cm^{-1})	**Seed coat region**	**Attributions**	**Main Compounds**	**Ref.**
970	Mid, inner	ν (C-O)	Cutin, polysaccharides	(HEREDIA-GUERRERO et al., 2014)
992	Outter	C–O stretch	Cutin	(TÜRKER-KAYA; HUCK, 2017)
1012 - 1014	Mid, outter	υ(CO), υ(CC), δ(C-OH),	Pectin	(BUTLER et al., 2017)
1021	Outter	C–C, C–O Stretching	Carbohydrates	(THUMANU et al., 2015)
1030-1033	Mid, inner, outter	ν(C–O), ν(C–C)	Cellulose	(MONNIER et al., 2017)
1034 - 1037	Mid, outter	ν(OH), ν(C–OH)	Cell wall polysaccharides (arabinan)	(ZHU; TAN, 2016)
1040-1041	Inner, outter	O–H and C–OH stretch: cell wall polysaccarides	Arabinan, cellulose	(TÜRKER-KAYA; HUCK, 2017)

Table 2 (continued)

1046	Outter	ν(C-O), ν(C-C), ν(C=C), ν(COC)	Pectin, various polysaccharides, also suberin or cutin	(REGVAR et al., 2013)
1054 - 1058	Outter	C–O–C stretch; C–OH stretch; C–OH deformation; C–O–C deformation	Carbohydrate molecule	(BUTA et al., 2015)
1060 - 1061	Mid, inner	C–O stretch	Cell wall polysaccharides	(TÜRKER-KAYA; HUCK, 2017)
1074	Mid	pyranose, and furanose ring	Amylopectin and amylose	(KAČURÁKOVÁ; MATHLOUTHI, 1996)
1078	Mid, inner	β(COH)	Amylopectin and amylose	(KAČURÁKOVÁ; MATHLOUTHI, 1996)
1084	Inner	C–O deformation	Secondary alcohol, aliphatic ester	(TÜRKER-KAYA; HUCK, 2017)
1103 - 1106	Mid, inner, outter	νs(C-O-C), ester	Cutin	(TÜRKER-KAYA; HUCK, 2017)
1107 - 1108	Inner, outter	C–O–C sym stretch	Cutin	(TÜRKER-KAYA; HUCK, 2017)
1141	Inner	C–O–C asym stretch	Cellulose	(TÜRKER-KAYA; HUCK, 2017)
1148	Outter	ν(COC), ν(CC)	Amylopectin and amylose	(KAČURÁKOVÁ; MATHLOUTHI, 1996)
1156 - 1158	Mid, inner, outter	C–C ring	Cellulose	(THUMANU et al., 2015)
1162 - 1163	Inner	υ(C-OH), υ(C-O-C)	Polysaccharide, cellulose	(BUTLER et al., 2017)
1510	Inner	ν(C=C) aromatic	Lignin	(KAČURÁKOVÁ; MATHLOUTHI, 1996)
1514-1518	Mid, inner, outter	C=C aromatic strech	Lignin	(TÜRKER-KAYA; HUCK, 2017)

Table 2 (continued)

1520	Mid	ν(C–C) aromatic	Phenolic compounds	(SKOLIK et al., 2019)
1550	Inner	ν(C=N); ν(N–H)	Amide II	(KAČURÁKOVÁ; MATHLOUTHI, 1996)
1599 - 1601	Mid, outter	υ(COO-)	Pectin, carboxylic acids	(BUTLER et al., 2017)
1607	Mid	ν (C-C) aromatic	Phenolic compounds	(HEREDIA-GUERRERO et al., 2014)

Key: ν - stretching, as – asymmetric, s - symmetric, β – in-plane bending, δ - scissoring, ω - wagging, τ - twisting, def – deformation.

4.4 Conclusion

As shown in the SEM images and µ-XRF maps most part of Zn, regardless of the source, was associated to the seed coat of the treated seeds. µ-XANES chemical speciation and LCF analysis unraveled that Zn from both treatments (ionic and nanoparticle) was complexed with organic molecules in an environment comparable to that of Zn-malate and Zn-citrate in similar proportions.

ATR-FTIR and µ-FTIR analysis allowed to identify differences in the regions of the spectra from 800 cm^{-1} to 1300 cm^{-1} (region of the carbohydrates assigned in the FTIR spectra) and from 1400 cm^{-1} to 1700 cm^{-1} (region of the protein, phenolic compounds, lignin, pectin, etc, assigned in the FTIR spectra) in the different layers of common bean seed coat samples soaked in ZnO 40 nm and $ZnSO_4$ at 100 and 1000 mg L^{-1}. More protein content was found in the inner surface than in the outer surface. Observing the differences among the inner surface treatments, samples treated with ZnO 40 nm and ZnSO4 at 100 mg L-1 showed reduced protein content. Carbohydrates and proteins are closely linked to enzymatic processes that occurs in the germination of the beans (BEWLEY; BLACK, 1994) and are also involved in protection mechanisms of the seeds(MELLO et al., 2010).

References

ALLOWAY, B. J. Soil factors associated with zinc deficiency in crops and humans. **Environmental Geochemistry and Health**, Dordrecht, v. 31, n. 5, p. 537–548, 2009.

BABAJANI, A.; IRANBAKHSH, A.; ORAGHI ARDEBILI, Z.; ESLAMI, B. Seed priming with non-thermal plasma modified plant reactions to selenium or zinc oxide nanoparticles: cold plasma as a novel emerging tool for plant science. **Plasma Chemistry and Plasma Processing**, New York, v. 39, n. 1, p. 21–34, 2019.

BEWLEY, J. D.; BLACK, M. Seeds BT. In: ________ (Ed.). **Seeds**: physiology of development and germination. 2. ed. New York: Springer-Verlag, 1994. p.1–33.

BROADLEY, M.; BROWN, P.; CAKMAK, I.; RENGEL, Z.; ZHAO, F. Function of nutrients: Micronutrients. In: MARSCHNER, H. **Marschner's mineral nutrition of higher plants**. 3. ed. New York: Academic Press, 2012.

BUTA, E.; CANTOR, M.; ȘTEFAN, R.; POP, R.; MITRE JUNIOR, I.; BUTA, M.; SESTRAȘ, R. E. FT-IR Characterization of pollen biochemistry, viability and germination capacity in Saintpaulia H . Wendl. Genotypes. **Journal of Spectroscopy**, New York, v. 2015, art. ID 706370, 2015. doi: 10.1155/2015/7063702015.

BUTLER, H. J.; ADAMS, S.; MCAINSH, M. R.; MARTIN, F. L. Detecting nutrient deficiency in plant systems using synchrotron Fourier-transform infrared microspectroscopy. **Vibrational Spectroscopy**, Amsterdam, v. 90, p. 46–55, 2017.

CHIORATO, A. F.; CARBONELL, S. A. M.; GONÇALVES, J. G. R.; SILVA, D. A. da; Benchimol-Reis, L. L.; CARVALHO, C. R. L.; BARROS, V. L. N. P. de; FREITAS, R. S. de; TICELLI, M.; GALLO, P. B.; SANTOS, N. C. B. dos. IAC Sintonia: new carioca common bean cultivar. **Crop Breeding and Applied Biotechnology**, Stockholm, v. 18, p. 338-342, 2018.

DESHPANDE, S. S.; CHERYAN, M. Microstructure and water uptake of phaseolus and winged beans. **Journal of Food Science**, Malden, v. 51, n. 5, p. 1218–1223, 1986.

DURAN, N. M.; MEDINA-LLAMAS, M.; CASSANJI, J. G. B.; LIMA, R. G. de; ALMEIDA, E. de; MACEDO, W. R.; MATTIA, D.; CARVALHO, H. W. P. de. Bean seedling growth enhancement using magnetite nanoparticles. **Journal of Agricultural and Food Chemistry**,Washington, DC, v. 66, n. 23, p. 5746–5755, 2018.

DURAN, N. M.; SAVASSA, S. M.; LIMA, R. G. D.; ALMEIDA, E. de; LINHARES, F. S.; VAN GESTEL, C. A. M.; CARVALHO, H. W. P. de. X-ray spectroscopy uncovering the effects of Cu based nanoparticle concentration and structure on *Phaseolus vulgaris* germination and seedling development. **Journal of Agricultural and Food Chemistry**, Washington, DC, v. 65, n. 36, p. 7874-7884, 2017.

ELHAJ BADDAR, Z.; UNRINE, J. M. Functionalized ZnO nanoparticle seed treatments to enhance growth and Zn content of wheat (*Triticum aestivum*) seedlings. **Journal of Agricultural and Food Chemistry**,Washington, DC, v. 66, n. 46, p. 12166–12178, 2018.

ESTRADA-URBINA, J.; CRUZ-ALONSO, A.; SANTANDER-GONZÁLEZ, M.; MÉNDEZ-ALBORES, A.; VÁZQUEZ-DURÁN, A. Nanoscale zinc oxide particles for improving the physiological and sanitary quality of a mexican landrace of red maize. **Nanomaterials**, Basel, v. 8, n. 4, p. 247, 2018.

GAUTAM, R.; VANGA, S.; ARIESE, F.; UMAPATHY, S. Review of multidimensional data processing approaches for Raman and infrared spectroscopy. **EPJ Techniques and Instrumentation**, Heidelberg, v. 2, n. 1, p. 8, 2015.

GOKAK, I. B.; TARANATH, T. C. Morphological and biochemical responses of *Abelmoschus esculantus* (L.) Moench to zinc nanoparticles. **Advances in Natural Sciences: Nanoscience and Nanotechnology**, Bristol, v. 6, n. 2, p. 025017, 2015.

HARRIS, D.; RASHID, A.; MIRAJ, G.; ARIF, M.; SHAH, H. 'On-farm' seed priming with zinc sulphate solution: a cost effective way to increase the maize yields of resource-poor farmers. **Field Crops Research**, Amsterdam, v. 102, n. 2, p. 119–127, 2007.

HEREDIA-GUERRERO, J. A.; BENÍTEZ, J. J.; DOMÍNGUEZ, E.; BAYER, I. S.; CINGOLANI, R.; ATHANASSIOU, A.; HEREDIA, A. Infrared and Raman spectroscopic features of plant cuticles: a review. **Frontiers in Plant Science**, Lausanne, v. 5, 305, 2014. doi: 10.3389/fpls.2014.00305.

HOE, P. T.; MAI, N. D. C.; LIÊN, L. Q.; BẢN, N. K.; MINH, C. V.; CHAU, N. T. H.; NGÔ; BUU, Q.; HIEN, D. T.; TUONG VAN, N. V.; HIEN, L. T.; LINH, T. T. M. Germination responses of soybean seeds under Fe, ZnO, Cu and Co nanoparticle treatments. **International Journal Of Agriculture & Biology**, Faisalabad, v. 20, p. 1562–1568, 2018.

JOSHI, A.; KAUR, S.; DHARAMVIR, K.; NAYYAR, H.; VERMA, G. Multi-walled carbon nanotubes applied through seed-priming influence early germination, root hair, growth and yield of bread wheat (*Triticum aestivum* L.). **Journal of the Science of Food and Agriculture**, London, v. 98, n. 8, p. 3148–3160, 2018.

KAČURÁKOVÁ, M.; MATHLOUTHI, M. FTIR and laser-Raman spectra of oligosaccharides in water: characterization of the glycosidic bond. **Carbohydrate Research**, Amsterdam, v. 284, n. 2, p. 145–157, 1996.

KASOTE, D. M.; LEE, J. H. J.; JAYAPRAKASHA, G. K.; PATIL, B. S. Seed priming with iron oxide nanoparticles modulate antioxidant potential and defense linked hormones in watermelon seedlings. **ACS Sustainable Chemistry & Engineering**, Washington, DC, v. 7, n. 5, p. 5142–5151, 2019.

KOPITTKE, P. M.; MCKENNA, B. A.; KARUNAKARAN, C.; DYNES, J. J.; ARTHUR, Z.; GIANONCELLI, A.; KOUROUSIAS, G.; MENZIES, N. W.; RYAN, P. R.; WANG, P.; GREEN, K.; BLAMEY, F. P. C. Aluminum complexation with malate within the root apoplast differs between aluminum resistant and sensitive wheat lines. **Frontiers in Plant Science**, Lausanne, v. 8, p. 1377, 2017.

LI, X.; YANG, Y.; GAO, B.; ZHANG, M. Stimulation of peanut seedling development and growth by zero valent iron nanoparticles at low concentrations. **Plos One**, San Francisco, v. 10, n. 4, p. e0122884, 2015.

MARÉCHAL, Y.; CHANZY, H. The hydrogen bond network in Iβ cellulose as observed by infrared spectrometry. **Journal of Molecular Structure**, Amsterdam, v. 523, n. 1, p. 183–196, 2000.

MELLO, J. I. de O.; BARBEDO, C. J.; SALATINO, A.; FIGUEIREDO-RIBEIRO, R. de C. L. Reserve carbohydrates and lipids from the seeds of four tropical tree species with different sensitivity to desiccation. **Brazilian Archives of Biology and Technology**, Curitiba, v. 53, n. 4, p. 889-899, 2010.

MIKAC, U.; SEPE, A.; SERŠA, I. MR microscopy for noninvasive detection of water distribution during soaking and cooking in the common bean. **Magnetic Resonance Imaging**, New York, v. 33, n. 3, p. 336–345, 2015.

MONNIER, G.; FRAHM, E.; LUO, B.; MISSAL, K. Developing FTIR microspectroscopy for analysis of plant residues on stone tools. **Journal of Archaeological Science**, New York, v. 78, p. 158–178, 2017.

MORALES, M. I.; RICO, C. M.; HERNANDEZ-VIEZCAS, J. A.; NUNEZ, J. E.; BARRIOS, A. C.; TAFOYA, A.; FLORES-MARGES, J. P.; PERALTA-VIDEA, J. R.; GARDEA-TORRESDEY, J. L. Toxicity assessment of cerium oxide nanoparticles in cilantro (Coriandrum sativum L.) plants grown in organic soil. **Journal of Agricultural and Food Chemistry**, Washington, DC, v. 61, n. 26, p. 6224–6230, 2013.

MUNIR, T.; RIZWAN, M.; KASHIF, M.; SHAHZAD, A.; ALI, S.; AMIN, N.; ZAHID, R.; ALAM, M. F. E.; IMRAN, M. Effect of zinc oxide nanoparticles on the growth and Zn uptake in wheat (Triticum aestivum L.) by seed priming method. **Digest Journal of Nanomaterials and Biostructures**, Bucharest, v. 13, n. 1, p. 315-323, 2018.

MUTHUKRISHNAN, R.; ROHINI, R. LASSO: A feature selection technique in predictive modeling for machine learning. In: 2016 IEEE INTERNATIONAL CONFERENCE ON ADVANCES IN COMPUTER APPLICATIONS (ICACA), 2016, Coimbatore, India. p.18–20. doi: 10.1109/ICACA.2016.7887916.

NANDHINI, M.; RAJINI, S. B.; UDAYASHANKAR, A. C.; NIRANJANA, S. R.; LUND, O. S.; SHETTY, H. S.; PRAKASH, H. S. Biofabricated zinc oxide nanoparticles as an ecofriendly alternative for growth promotion and management of downy mildew of pearl millet. **Crop Protection**, Guildford, v. 121, p. 103–112, 2019.

QUTOB, D.; MA, F.; PETERSON, C. A.; BERNARDS, M. A.; GIJZEN, M. Structural and permeability properties of the soybean seed coat. **Botany**, Ottawa, v. 86, n. 3, p. 219–227, 2008.

REGVAR, M.; EICHERT, D.; KAULICH, B.; GIANONCELLI, A.; PONGRAC, P.; VOGEL-MIKUŠ, K. Biochemical characterization of cell types within leaves of metal-hyperaccumulating Noccaea praecox (Brassicaceae). **Plant and Soil**, The Hague, v. 373, n. 1, p. 157–171, 2013.

SARRET, G.; SAUMITOU-LAPRADE, P.; BERT, V.; PROUX, O.; HAZEMANN, J. L.; TRAVERSE, A.; MARCUS, M. A.; MANCEAU, A. Forms of zinc accumulated in the hyperaccumulator Arabidopsis halleri. **Plant Physiology**, Rockville, v. 130, n. 4, p. 1815–1826, 2002.

SARRET, G.; BALESDENT, J.; BOUZIRI, L.; GARNIER J. M.; MARCUS, M. A.; GEOFFROY, N.; PANFILI, F.; MANCEAU, A. Zn speciation in the organic horizon of a contaminated soil by micro X-ray fluorescence, micro and powder EXAFS spectroscopy and isotopic dilution. **Environmental Science & Technology**, Washington, DC, v. 38, n. 10, p. 2792-2801, 2004.

SAVASSA, S. M.; DURAN, N. M.; RODRIGUES, E. S.; ALMEIDA, E. de; VAN GESTEL, C. A. M.; BOMPADRE, T. F. V.; CARVALHO, H. W. P. de. Effects of ZnO nanoparticles on Phaseolus vulgaris germination and seedling development determined by X-ray spectroscopy. **ACS Applied Nano Materials**, Washington, DC, v. 1, n. 11, p. 6414–6426, 2018.

SKOLIK, P.; MCAINSH, M. R.; MARTIN, F. L. ATR-FTIR spectroscopy nondestructively detects damage-induced sour rot infection in whole tomato fruit. **Planta**, Berlin, v. 249, n. 3, p. 925–939, 2019.

SOUZA, F. H. D. DE; MARCOS-FILHO, J. The seed coat as a modulator of seed-environment relationships in Fabaceae. **Revista Brasileira de Botânica**, São Paulo, v. 24, n. 4, p. 365–375, 2001.

SUNDARIA, N.; SINGH, M.; UPRETI, P.; CHAUHAN, R.P.; JAISWAL, J. P.; KUMAR, A. Seed priming with iron oxide nanoparticles triggers iron acquisition and biofortification in wheat (Triticum aestivum L.) grains. **Journal of Plant Growth Regulation**, New York, v. 38, n. 1, p. 122–131, 2019.

SURESH, S.; KARTHIKEYAN, S.; JAYAMOORTHY, K. FTIR and multivariate analysis to study the effect of bulk and nano copper oxide on peanut plant leaves. **Journal of Science: Advanced Materials and Devices**, Hanoi, v. 1, n. 3, p. 343–350, 2016.

SUSINI, J.; COTTE, M.; SCHEIDT, K.; CHUBAR, O.; POLACK, F.; DUMAS, P. Technical report: the FTIR Spectro microscopy end station at the ESRF-ID21 Beamline. **Synchrotron Radiation News**, New York, v. 20, n. 5, p. 13–16, 2007.

THUMANU, K.; SOMPONG, M.; PHANSAK, P.; NONTAPOT, K.; BUENSANTEAI, N. Use of infrared microspectroscopy to determine leaf biochemical composition of cassava in response to Bacillus subtilis CaSUT007. **Journal of Plant Interactions**, Abingdon, v. 10, n. 1, p. 270–279, 2015.

TIBSHIRANI, R. Regression Shrinkage and Selection via the Lasso. **Journal of the Royal Statistical Society. Series B (Methodological)**, London, v. 58, n. 1, p. 267–288, 1996.

TOLRA, R. P.; POSCHENRIEDER, C.; BARCELO, J. Zinc hyperaccumulation in Thlaspi caerulescens. II. Influence on organic acids. **Journal of Plant Nutrition**, v. 19, n. 12, p. 1541-1550, 1996.

TOPLAK, M.; BIRARDA, G.; READ, S.; SANDT, C.; ROSENDAHL, S. M.; VACCARI, L.; DEMŠAR, J.; BORONDICS, F. Infrared orange: connecting hyperspectral data with machine learning. **Synchrotron Radiation News**, New York, v. 30, n. 4, p. 40–45, 2017.

TÜRKER-KAYA, S.; HUCK, W. C. A review of mid-infrared and near-infrared imaging: principles, concepts and applications in plant tissue analysis. **Molecules**, Basel, v. 22, 2017. doi: 10.3390/molecules22010168.

WELCH, R. M.; GRAHAM, R. D. A new paradigm for world agriculture: meeting human needs: Productive, sustainable, nutritious. **Field Crops Research**, Amsterdam, v. 60, n. 1, p. 1–10, 1999.

WIERCIGROCH, E.; SZAFRANIEC, E.; CZAMARA, K.; PACIA, M. Z.; MAJZNER, K.; KOCHAN, K.; KACZOR, A.; BARANSKA, M.; MALEK, K. Raman and infrared spectroscopy of carbohydrates: a review. **Spectrochimica Acta Part A: Molecular and Biomolecular Spectroscopy**, Amsterdam, v. 185, p. 317–335, 2017.

YEUNG, E. C. Developmental changes in the branched parenchyma cells of bean seed coat. **Protoplasma**, Leipzig, v. 118, n. 3, p. 225–229, 1983.

ZHAO, L.; PERALTA-VIDEA, J. R.; RICO, C. M.; HERNANDEZ-VIEZCAS, J. A.; SUN, Y.; NIU, G.; SERVIN, A.; NUNEZ, J. E.; DUARTE-GARDEA, M.; GARDEA-TORRESDEY, J. L. CeO_2 and ZnO nanoparticles change the nutritional qualities of cucumber (*Cucumis sativus*). **Journal of Agricultural and Food Chemistry**, Washington, DC, v. 62, n. 13, p. 2752–2759, 2014.

ZHU, Y.; TAN, T. L. Penalized discriminant analysis for the detection of wild-grown and cultivated Ganoderma lucidum using Fourier transform infrared spectroscopy. **Spectrochimica Acta Part A: Molecular and Biomolecular Spectroscopy**, Amsterdam, v. 159, p. 68–77, 2016.

5 GENERAL CONCLUSIONS

The investigation of how nanoparticles (NP) interact with plants, in special seeds, proved to be a challenging and motivating subject. The study covering a wide range of concentrations and sizes, in addition to two compositions, granted an in-depth view of how nanoparticles are trapped in the seed coat and how they are biotransformed.

Regarding the stablished hypothesis, this thesis showed that nanoparticles remain mainly trapped at the seed coat. At proper concentration and size, NP may be a suitable form for *Phaseolus vulgaris* seed priming and therefore improves germination rate and/or seedling development. The evaluated nanoparticles can be biotransformed along the seed coat, and at least ions leached from the nanoparticles might translocate from the seed coat to the root tip.

Spectroscopic methods such as µ-XRF and µ-XANES are crucial tools to investigate the interaction of nanomaterials in biological tissues. The increasingly analytical power of synchrotron machines will allow, taking due precautions to avoid tissue damages, to obtain maps with enhanced lateral resolutions. Ultimately, tracing the biotransformation throughout the sample under real time. This statement is also true for FTIR, including its variants, such as µ-FTIR and nano-FTIR. These techniques, dedicated to probe the organic compounds, are complementary to X-ray based ones.

Scanning electron microscopy (SEM) images showed that ZnO 40 nm and Ag_2S NP agglomerated around the hilum structure and in spots in the seed coat. µ-XRF revealed that part of the Zn, regardless of the source, was associated with the seed coat and embryo. For Ag treatments, µ-XRF shows stronger interaction betw een treatments and seed coat for $AgNO_3$ and Ag^0 NP (15 nm) than Ag_2S NP (42 nm). These results suggest that not all the nanoparticles have a strong interaction with the bean seeds, i.e. that both their composition and size can interfere.

The biotransoformation of nanoparticles within the seed coat depended on the particle composition. µ-XANES revealed that Zn, issued from $ZnSO_4$ and nano ZnO, was associated to similar organic-like molecules such as malate and citrate. Linear combination analysis indicated similar proportions of these molecules in samples. For Ag treatments, the results depended on the source. In the $AgNO_3$ treatment, Ag was found as AgCl on the surface layer and Ag_2CO_3 in the parenchyma layer. For Ag^0 NP treatment, it was found as Ag-thiol-containing organic ligand (Ag-cysteine). Ag_2S NP was not biotransformed. These results are lined up with the literature. Although the causal relationship between composition and biotransformation is not established, the Ksp value for bulk Ag_2S, 1.1×10^{-51} suggests that solubility might be an important driver. However, one has to keep in mind that Ksp values for bulk may differ for nanomaterials.

Regarding morphological aspects, ZnO 40 nm at 10-100 mg L^{-1} improved the germination rate and seedling development, while $ZnSO_4$ used as ionic control, in most cases, presented toxic results. For Ag, none of the treatments presented meaningful differences in germination rate compared to control. On the other hand, Ag_2S NP at 1 mg L^{-1} improved seedling development.

This positive result might be related to the entrance of nanoparticles, or dissolved ions, through the hilum of the seed. This statement is supported by images that revealed this structure as the most important accumulation hot spot (as shown in this study). Another hypothesis that is also supported by literature regards the generation micro/nano scarifications in the seed coat by the nanoparticles. Ultimately, it would increase the flow of water and nutrients, therefore accelerating the germination.

Finally, additional studies are necessary to complement the results here presented. Considering that certain types of nanoparticles at specific concentrations can improve the germination and early stages of the development, it is necessary to tune the nanoparticle to obtain greater yields. Since the presumed use of nanotechnology in seed coat will require large amounts of nanomaterials, its feasibility is dependent on making them affordable. In other words, the cost-benefit of nanomaterials must be competitive in relation to current inputs. It is also necessary to reflect about methods of application of these compounds to not put the health of rural workers at risk. As previously mentioned, this is an urgent, challenging and motivating subject that requires substantial research.

ANNEX

Annex A – Permission to reuse in Thesis

12/06/2019 Rightslink® by Copyright Clearance Center

Title: Effects of ZnO Nanoparticles on Phaseolus vulgaris Germination and Seedling Development Determined by X-ray Spectroscopy

Author: Susilaine M. Savassa, Nádia M. Duran, Eduardo S. Rodrigues, et al

Publication: ACS Applied Nano Materials

Publisher: American Chemical Society

Date: Nov 1, 2018

Copyright © 2018, American Chemical Society

LOGIN

If you're a copyright.com user, you can login to RightsLink using your copyright.com credentials.

Already **a RightsLink user** or want to learn more?

PERMISSION/LICENSE IS GRANTED FOR YOUR ORDER AT NO CHARGE

This type of permission/license, instead of the standard Terms & Conditions, is sent to you because no fee is being charged for your order. Please note the following:

- Permission is granted for your request in both print and electronic formats, and translations.
- If figures and/or tables were requested, they may be adapted or used in part.
- Please print this page for your records and send a copy of it to your publisher/graduate school.
- Appropriate credit for the requested material should be given as follows: "Reprinted (adapted) with permission from (COMPLETE REFERENCE CITATION). Copyright (YEAR) American Chemical Society." Insert appropriate information in place of the capitalized words.
- One-time permission is granted only for the use specified in your request. No additional uses are granted (such as derivative works or other editions). For any other uses, please submit a new request.

Copyright © 2019 Copyright Clearance Center, Inc. All Rights Reserved. Privacy statement. Terms and Conditions.
Comments? We would like to hear from you. E-mail us at customercare@copyright.com

Title: Effects of ZnO Nanoparticles on Phaseolus vulgaris Germination and Seedling Development Determined by X-ray Spectroscopy

Author: Susilaine M. Savassa, Nádia M. Duran, Eduardo S. Rodrigues, et al

Publication: ACS Applied Nano Materials

Publisher: American Chemical Society

Date: Nov 1, 2018

LOGIN

If you're a copyright.com user, you can login to RightsLink using your copyright.com credentials.

Already **a RightsLink user** or want to learn more?

Quick Price Estimate

Permission for this particular request is granted for print and electronic formats, and translations, at no charge. Figures and tables may be modified. Appropriate credit should be given. Please print this page for your records and provide a copy to your publisher. Requests for up to 4 figures require only this record. Five or more figures will generate a printout of additional terms and conditions. Appropriate credit should read: "Reprinted with permission from {COMPLETE REFERENCE CITATION}. Copyright {YEAR} American Chemical Society." Insert appropriate information in place of the capitalized words.

I would like to...	reuse in a Thesis/Dissertation
Requestor Type	Author (original work)
Portion	Full article
Format	Print
Will you be translating?	No
Select your currency	USD - $

This service provides permission for reuse only. If you do not have a copy of the article you are using, you may copy and paste the content and reuse according to the terms of your agreement. Please be advised that obtaining the content you license is a separate transaction not involving Rightslink.